Synthesis and Characterisation of Tuneable, High Attachment Density Raspberry Particles

By

Kaili Nicole Stacey

Thesis
Submitted to Flinders University
For the Degree of

Doctor of Philosophy

College of Science and Engineering
15 November 2022

Declaration

I certify that this thesis:

1. does not incorporate without acknowledgment any material previously submitted for a degree or diploma in any university
2. and the research within will not be submitted for any other future degree or diploma without the permission of Flinders University; and
3. to the best of my knowledge and belief, does not contain any material previously published or written by another person except where due reference is made in the text.

Signed - Kaili Stacey 15 November 2022

Acknowledgements

Firstly, I would like to thank Flinders University and the Australian government for their awarding me the Australian Government Research Training Program Scholarship (Excellence). In addition, to the Playford Trust for their support through the Playford Trust PhD Scholarship.

I would also like to thank the staff at Microscopy Australia and the Australian National Fabrication Facility at the South Australian Nodes for their training on the instruments that became fundamental to this project.

Another huge thank you to David Lewis, my supervisor, for helping me work through my frustration when nothing I tried was working and for teaching me a lot about scientific communication and resilience.

To my group members, Daniel Mangos, Oskar Majewski, Rowan McDonough, Schannon Hamence, Kay Chen, Stefan Martino, Chris Hassam, and Elliot Jew for brainstorming ideas with me and for their friendship over the years. A special thanks to Alex Ashendon for being willing to talk nonsense with me over Vietnamese food.

To Noarlunga Netball club and all the amazing people there, thank you for providing a physical outlet for all my frustration; and for the years of pub trips. I owe you all a big batch of pistachio macarons.

To my friends for providing me with love, support, and distraction when I needed them. I've been so happy to know you all and here's to many more years of friendship.

Last, but not least, to thank my family. Janet, Ian, and Tash, for their unwavering support in me and for all the amazing home cooked meals. I would also like to thank my pets, past and present, for their ability to always put a smile on my face when I thought smiling was beyond me.

Summary

The attachment of nanoparticles to each other has a wide variety of applications in areas including superhydrophobic coatings, drug delivery, synthetic opals, antifouling, and catalysis.

As the properties of nanoparticles are dictated by both their chemical composition and their size, the development of new methods to attach particles of different sizes and materials to each other is an important field of study. In particular, the use of raspberry particles in the development of superhydrophobic, catalytic, and photonic materials was of particular interest in this thesis.

This thesis focuses on the characterisation of silica nanoparticles and the development of attachment reactions to produce silica-on-silica and gold-on-silica raspberry particles.

The effect of synthesis method, cleaning method, ammonia concentration, ethanol concentration, and atmospheric oxygen on the oxidation of thiols to disulphides during MPTMS particle synthesis was studied via Raman Microscopy and Ellman's reagent assays. These results were used to propose a mechanism for the formation of disulphides during particle synthesis. A method was also developed for the post-synthesis reduction of disulphides to thiols at the particle surface, which also confirmed the presence of disulphides on the surface of the particle.

Larger particles were synthesised from GPTMS via an emulsion method and were then used in the development of an attachment reaction of MPTMS particles to GPTMS particles to form raspberry particles. This reaction utilised the base-catalysed thiol-epoxy click reaction to form covalent bonds between the two types of particles. During the development of this reaction, the effect of particle concentration and the use of thiol-functionalised MPTMS particles vs disulphide-functionalised MPTMS particles on the final attachment density was determined. SEM and zeta potential measurements were used in the development and characterisation of the attachment reaction and the final raspberry particles.

These raspberry particles enabled a combinatorial approach to the production of multiscale superhydrophobic coatings with PDMS. The effect of particle:polymer mass ratio and small:large particle size ratio on the wettability of the final coatings was investigated through contact and sliding angle experiments, and SEM. A superhydrophobic coating with a water contact angle of 157.5^{o} and a sliding angle of 6.8^{o} was produced using this method.

Citrate-stabilised gold particles were synthesised via the Turkevich method. The affinity of citrate-stabilised gold for thiols, disulphides, and amines was investigated through small molecule ligand exchange reactions, attachments to functionalised flat surfaces, and attachments to thiol- and disulphide-functionalised MPTMS particles. These reactions were analysed through a combination of

FTIR, UV-Vis, DLS, and SEM techniques. It was found that amines were the most suitable for attachment to citrate-gold particles.

This information was then used to develop an attachment reaction for citrate-gold particles onto a larger GPTMS silica particle core via the use of ethylene diamine as a linker. The effect of gold particle excess on the attachment density was explored via SEM analysis. This attachment reaction resulted in gold-silica raspberry particles with high attachment density

Table of Contents

List of Figures

List of Tables

List of Equations

Details of Supplementary Information

Supplementary information is relevant to section 4.4.7 Effect of Raspberry Particle Size Ratio on Coating Wettability.

Videos of raspberry particle/PDMS coating water drop sliding probability at 0^{o} inclination are provided as supplementary information. Three videos are provided for coatings with raspberry particle small:large size ratios of 0.045:1, 0.101:1, and 0.108 are provided.

Abbreviations

APTMS	**(3-aminopropyl)trimethoxysilane**
ATR-FTIR	Attenuated Total Reflection Fourier Transform Infrared
DLS	Dynamic Light Scattering
DMSO	Dimethyl Sulfoxide
DTNB	5,5'-Dithiobis(2-nitrobenzoic acid)
EDAX	Energy-Dispersive X-ray Spectroscopy
FCC	Face-Centred Cubic
GPTMS	(3-Glycidyloxypropyl)trimethoxysilane
MPTMS	(3-Mercaptopropyl)trimethoxysilane
$NaBH_4$	Sodium Borohydride
PDMS	Polydimethylsiloxane
PMMA	Poly(Methyl Methacrylate)
SA	Sliding Angle
SAM	Self-Assembled Monolayer
SEM	Scanning Electron Microscope
TEOS	tetraethylorthosilicate
THPC	tetrakishydroxymethylphosphonium chloride
TNB	2-nitro-5-thiobenzoic acid
UV-Vis	Ultraviolet-visible
VTES	Vinyltriethoxysilane
WCA	Water Contact Angle
XPS	Xray Photoelectron Spectroscopy

Chapter 1: Introduction

Complex micro and nano structures have a wide variety of applications such as superhydrophobic coatings,[3-27] drug delivery,[28] photonic crystals,[29-55] antifouling,[56,57] and catalysis,[58-61] among others. As such, the development of new materials that contain features of different scales or chemical composition is an important field of research.

These complex structures can be fabricated via a wide variety of techniques, including templating,[62] lithography,[63-66] soft lithography,[62,67,68] and chemical vapour deposition.[69,70] However, many of these methods have strict operating conditions, expensive instruments and/or chemicals, and are not easily scalable to large-scale use.

The use and manipulation of colloidal particle solutions has become a growing area of research owing to their versatility in the materials that can be used, their cost effectiveness, and the potential for the production of materials at a relatively large scale. Two of the ways in which nanoparticles can be manipulated to form more complex structures include self-assembly and attachment of particles to each other. For instance, colloidal suspensions of monodispersed nanoparticles can be used in the production of synthetic opal structures,[29,32,33,35-37,39,41-44,46,48-55,71-73] while particle-on-particle attachments have been used in the production of superhydrophobic, self-cleaning coatings[7,9,13,14,18-20,22,24,26,27,74-78] and catalytic enhancement.[59,60,79-81] In addition, the combination of nanoparticles of different materials can give rise to a number of interesting photonic properties.[41,82-86]

The driving force behind both self-assembly and attachment of these nanoparticles is the interaction of the surface chemistry of the particles. As such, understanding of particle surface chemistry and the subsequent development of new attachment methods is essential in the formation of new materials.

The goals of this thesis are to form complex particle structures in which gold and silica particles are combined to create novel optical and topological properties. As background, in this chapter the synthesis of colloidal particles is explored, with an emphasis on silica and gold, and the reaction conditions that can be used to manipulate their physical and chemical properties. Particle packing structures and attachments that have been reported in literature are then presented and their possible photonic and superhydrophobic properties are explained. Finally, the chemical strategies that will be used in this thesis to synthesise and attach particles together into raspberry macrostructures, as well as analysing their resultant properties are investigated.

1.1 Self Assembly

One of the most common examples of self-assembly is the formation of self-assembled monolayers (SAMs) of bifunctional molecules on a surface as shown in Figure 1 below.[87-93] Surfactant molecules are able to form a very ordered structure, with the key aspects being the "head" has significantly different interaction with the surface than the "tail", a uniform size, and even distribution across the surface.[87-93] This attachment can completely change the properties of the surface[87-93] depending on the attached compound, making it a very useful technique in wide variety of research areas including hydrophobic or hydrophilic coatings,[90,94,95] anti-biofouling,[96,97] or biosensing.[93,98]

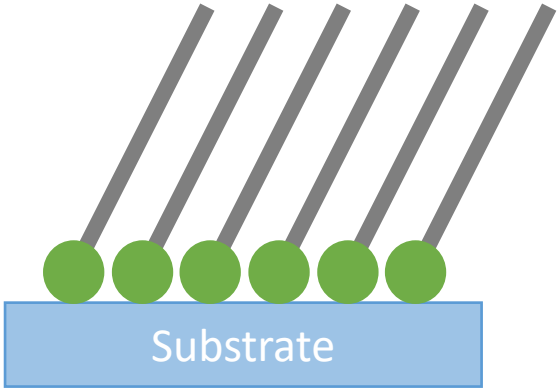

Figure 1: Schematic of a basic SAM, showing the head group in green and the tail in grey.

In order for a SAM to be produced, the attached molecule must form relatively strong bonds with the surface; otherwise, the molecules would be too easily removed during subsequent processes and analysis. Consequently, a more in-depth investigation into the properties of surfaces compared to the bulk material is required. The atoms at the surface of a material tend to be more reactive due to them having fewer neighbouring atoms and thus having 'dangling bonds'.[99-101] In addition, the purity and cleanliness of the surface is a major determining factor of the quality of the final SAM.

The understanding of SAMs has led to the attachment of small molecules to surfaces that are not flat,[102,103] for example the inside of tubes[104] or onto the surface of nanoparticles.[105,106] Nanoparticles have increased surface area to volume ratios compared to bulk materials. Thus, their properties are dominated by the surface, often resulting in very interesting optical, electronic, catalytic, etc. properties that are directly controlled by their size.[107-109] This increased surface area also allows for increased rates of reaction with less material required, as more surface is available for reactions to occur on nanoparticles compared to an equivalent amount of bulk material.

1.2 Self-Assembly of Particles

As an extension of attachment of macromolecules to surfaces, nanoparticles have also been attached to flat surfaces for a variety of applications. For example, catalytic nanoparticles have been attached to a flat substrate in order to increase the stability of the system.[110,111] The particle attachment prevents the particles from aggregating in solution and either reducing their reactivity or completely changing the properties.[110,111] These sort of attachments often have a secondary benefit in that they allow for continuous flow processes without the need for nanoparticle removal post-reaction.[112,113]

Ordered arrays of nanoparticles on flat surfaces can be used in the preparation of synthetic opals,[30,32,33,35-37,39,41-44,46,48,50,54,55,71-73,114,115] dust-repellent coatings,[116,117] and investigation of surface wettability,[118] among others. In particular, surface enhanced Raman spectroscopy (SERS) requires the use of a roughened substrate in order to magnify the Raman signal by up to 10^8. [119,120]

1.2.1 Synthetic Approaches to Self-Assembly of Particles

There have been many methods used to produce highly ordered, packed siliica particles to mimic the structures found in opals.[121] In an opal, monodispersed silica spheres are packed into a highly ordered lattice stucture as shown in Figure 2 below.[122,123]

Removed Due to Copyright Restriction

Figure 2: a) A colour photograph of opals found in nature[1]. b) A TEM shadowed replica image of the packing of silica spheres in an opal (modified from Darragh (1966)[2]

These range from more simple methods such as vertical deposition, gravity deposition, and moving meniscus methods to more complicated methods that incorporate the use of surfactants and shear force.[36,37,50,55,115] Despite their specific differences most of the reported procedures follow the same basic technique: A dispersion of monodispersed silica spheres (<10% polydispersity[50]) is made in an aqueous, alcoholic, etc. solvent. This solution is then left to evaporate allowing the particles to pack on the suspension vessel or on a substrate previously placed in the vessel.[36,124] The rate of sedimentation (V) of a simple gravitational deposition at atmospheric pressure can be described by Equation 1 below.[55] In this equation particle diameter, particle density, solvent density, gravitational acceleration, and solvent viscosity are represented by d, ρ_p, ρ_s, g, and η respectively.

Equation 1: Rate of Sedimentation

$$V = \frac{d^2(\rho_s - \rho_w)a}{18\eta}$$

Typical variations on this simple gravimetric method include introducing surfactants to prevent premature destabilisation of the particle suspension,[46,50,115,125] changes in the inclination angle of the substrate to be coated,[36] or the introduction of vacuum[55] or shear forces.[37] These changes can reduce defects in the final packed structure and improve mechanical properties.[46]

These methods tend to be very easy to accomplish and produce high quality packed structures.[29,30,32,36,37,41-44,46,48,50,54,55,72,115] However, the drying time can make them very time consuming (taking days or weeks to dry) and the final photonic crystals tend to be very fragile as the particles are only adsorbed onto the substrate.[36,37]

Inverse opal films have been developed in order to overcome these limitations.[31,35,37] There are again several different specific methods for the production of inverse opal films but the overall concept remains the same. Particles are used to make a photonic crystal as described above before a polymer is cast through the structure. The particles are then removed via a selective etching process, leaving behind a polymer film with periodic holes in it where the particles were.[31,123,126] The use of polymers makes a structure that is typically more mechanically durable and, depending on the polymer used, interesting properties can be achieved such as self-healing,[31] stimuli responsive colours,[126] and composite colours from stacking.[37] An alternative method for the production of inverse opal films is through the use of lithography. In this method e-beam lithography and reactive ion etching were used to bore an array of nano-holes into a silicon substrate.[67]

1.3 Optical Properties of Self-Assembled Particles

1.3.1 Photonic Crystals

Highly ordered structures with alternating refractive indices, such as the opal and inverse opal films discussed above, are referred to as photonic crystals.[37,123,127] Depending on whether the refractive index is periodic in 1, 2, or 3 dimensions, the photonic crystal can be referred to as 1D, 2D, or 3D.[123,127] Photonic crystals are able to induce coherent scattering[122] and as such they are responsible for structural colour seen in nature such as the Morpho butterfly wing,[128-135] opals,[2] and several plants.[136-138] This periodic variation in refractive index reflects certain wavelengths of light, called the photonic band gap, while allowing others to propagate through.[37,50] In general, structural colour tends to be more remarkable and is more resistant to fading then pigments and dyes.[67,122,131,137,138] It is also the cause of iridescence, i.e. where the observed colour changes with change in the angle of observation.[122,131,138]

1.3.2 Particle Packing and 3D Photonic Crystals

As previously mentioned, opals are formed when amorphous silica particles arrange into a highly ordered FCC lattice where water fills the voids between the particles.[122,123] This is likely the most famous example of a 3D photonic crystal in nature and has been the subject of many studies and replication attempts.

A 3D photonic crystal interacts with light via diffraction, resulting in constructive and destructive interference which gives colour[51,123,139] and the wavelength of maximum reflected intensity of the crystal can be calculated using a variation on the Bragg equation. The Bragg equation has angular dependence which gives rise to the observation of iridescence. However, it does not take into account the refractive index of the materials used as it was originally used for modelling light interactions with atomic crystal lattices.

In order to overcome this, modified Bragg equations like the ones shown in Equation 2,[50,51,126,139] Equation 3,[37,123,140] and Equation 4[124] are used, although there is inconsistencies in the literature as to which equation to use. Each of these equations describes some relationship between a combination of the wavelength of maximum reflection (λ), the angle of incidence of the light (θ), the interplanar spacing of the 111 plane (d), and the particle diameter (D). The effective refractive index (n_{eff}) can be calculated from the refractive indices (n_1 and n_2) and volume filling fractions (φ_1 and φ_2) of two different materials as shown in Equation 5. For a FCC lattice of spheres, the volume filling fraction of the particles is φ_1=0.74 while the surrounding matrix has a volume filling fraction of φ_1=0.26. [44]

Equation 2: Modified Bragg equation with angular dependence and interplanar distance terms [124]

$$m\lambda = 2d_{111}\left(n_{eff}^2 - \sin^2\theta\right)^{\frac{1}{2}}$$

Equation 3: Modified Bragg equation with no angular dependence [37,123,140]

$$\lambda = 2dn_{eff}$$

Equation 4: Modified Bragg equation with no angular dependence, spacing based on particle diameter rather than interplanar distance [37,50,126,139]

$$\lambda = \left(\frac{8}{3}\right)^{\frac{1}{2}} Dn_{eff}$$

Equation 5: Effective Refractive index of a FCC photonic crystal of packing spheres [37,44,50,125,126,139]

$$n_{eff} = n_1\phi_1 + n_2\phi_2$$

1.4 Photonic Single Particles

As previously discussed, the production of 3D photonic structures using particle packing has been extensively investigated but they have many limitations, driven by the need to maintain a high level of order over a large area.

A newer field of research is the production of single particles that can act as a photonic crystal by making multilayer particles where the refractive index varies within the particle structure. These types of particles will henceforth be referred to as photonic particles. The production of core-shell particles is not necessarily new and their use in close-packed FCC, 3D photonic crystals has been explored,[139,141-146] but it is very rare that any photonic properties are reported for the particles in solution. Insofar as I am aware, there are three existing papers that show the production of photonic particles.[124,125,147]

In 2006, Nakamura *et al* reported silica-titania core-shell nanoparticles with a very uniform titania coating.[124] Before this, most literature surrounding the production of 3D photonic crystals was focused on the use of plain silica or polystyrene nanoparticles and separately, the production of core-shell particles such as silica-gold, silica/polystyrene-zinc sulphide, or latex spheres with dyes or semiconductors in their shells. Nakamura et al[124] focused more on the use of the core-shell silica-titania particles in a packed FCC, 3D photonic crystal structure. However, there is a brief mention of the particles having a diffraction peak in solution, which then disappeared after the particles were sintered. It is believed that this diffraction peak is the result of the alternating titania-electrolyte layers acting as a 1D multilayer structure.[124]

In 2013, Huang *et al*[125] published a paper which focuses exclusively on silica-titania core-shell particles that were found to produce structural colour while still in solution. The method by which these particles were made was very similar to Nakamura's method, however, instead of titania nanosheets the titania was produced via a hydrolysis-condensation reaction of $(NH_4)_2TiF_6$ solution and H_3BO_3. The overall particle size was found to be 1360 nm while the titania layer was 170-200 nm thick. The plain silica spheres did not show any colour, however with the addition of a titania shell the dispersion was yellow in colour and a clear peak was seen in the UV/vis transmission spectra[125]. It was found that an increase in the titania layer thickness resulted in an increase in the wavelength of the transmission peak, corresponding to a red-shift of the colour in the solution[125]. This colour is believed to be the second order interference; the first-order interference was not observed, potentially because the titania layer was not perfectly smooth[125].

Tao *et al* (2016)[147] has a completely different approach in the production of photonic particles by using top-down methods. It also uses latitudinal material asymmetry to create structural colour, rather than a concentric, multilayered particle[147]. This was achieved by fabricating a macro-scale preform from pre-shaped segments. This preform was then coated in an amorphous cladding before being drawn in to a fibre with a diameter equal to the desired particle size. The surface energy at the interface between the cladding and the core is then exploited to initiate Plateau-Rayleigh capillary instability, which in turn creates a type of pearl necklace structure through thermally induced emulsification of

the core. The cladding is then selectively dissolved to produce the final photonic particles. The latitudinal refractive index variation results in polarization of the scattered light[147].

1.5 Particle-on-Particle Attachments

A progression of the attachments of particles to flat surfaces is the attachment of particles to other particles. This approach has been gaining interest and has a wide range of applications. In particular, this synthetic approach to materials can allow for the production of more complex structures than traditional materials processing or materials that can utilise the unique properties of different types of nanoparticles.

Of the complex geometries possible with particle-particle attachments, perhaps the most common is the so-called 'raspberry particle'. These are produced when a 'shell' of small nanoparticles are attached to a larger core particle to form a structure with hierarchal roughness as shown in Figure 3. The attached particles can be made from the same or different materials depending on the desired end use.

There have been several reported methods for the synthesis of these raspberry particles, with two major synthesis approaches. In the first approach, the core particles are produced and the shell particles are then grown directly on the core particle surface. Some example of this method are reported by Zhao *et al* (2016)[148] and Liu (2015)[10] where fluorinated shell particles were grown directly onto a silica core. Other reports have also used seeded emulsion polymerisation[25,149] or co-condensation[150] where phase separation is manipulated to produce the desired raspberry structure. In one example, Fu *et al* (2022)[5] synthesised crosslinked polyurethane/polyvinylpyrrolidone copolymer particles that were crosslinked with thiol and isocyanate monomers to improve their mechanical and chemical durability. Due to the swelling and subsequent shrinking of monomers during this synthesis reaction, raspberry-like protrusions are formed on the particles which were then fluorinated. However, most of these methods provide very little control over the size of the shell particles and as such the dependence of certain properties on the core-shell size ratio cannot be investigated.

The more common approach involves making the core and shell particles separately and then attaching them together[5,8,13,17,20,25,151-153] as shown in Figure 3. This attachment can be achieved in a myriad of different ways including electrostatic adsorption,[25,154] physical adsorption,[17,153,155] heteroflocculation,[152] usage of linker molecules,[20] thiol click chemistry,[5,8] etc. These methods often allow for greater flexibility in particle materials than a one-pot method with reported materials used including various polymers such as polystyrene,[17,20,25,149,151-153] poly(glycidyl acrylate),[8] poly(vinyl

propylene),[153] Silica,[10,13,17,25,150,151,153,154,156] gold,[59,80,81,85,156-160] calcium carbonate,[155] or a combination of materials.

In one example, Xu *et al* (2021)[25] made positively charged polystyrene/ methacryloxyethyltrimethyl ammonium chloride copolymer particles via dispersion polymerisation. These were then able to be attached to pre-purchased silica particles through electrostatic interactions between the positively charged polystyrene particle cores and the negatively charged silica particle shells. While this attachment method is experimentally simple, the resultant raspberry particles did not appear to have high attachment densities of the smaller shell particles onto the larger cores.

Many of the methods mentioned above fail to achieve high attachment densities, require post-synthesis particle functionalisation, have complicated synthesis methods, or provide very little control over the size ratios of the core to the shell particles which could have dramatic effects on their corresponding wetting or photonic properties and applications.

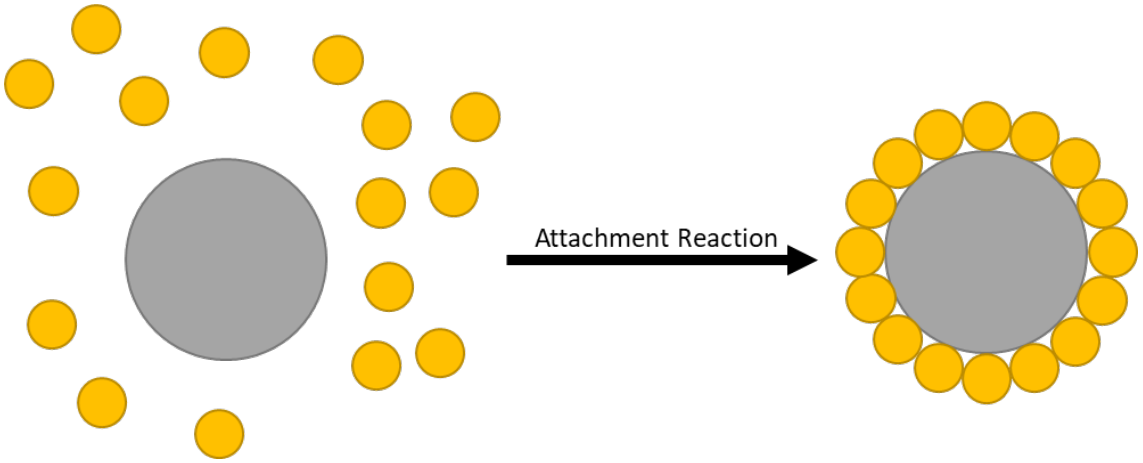

Figure 3: Simple diagram of raspberry particle synthsis via particle attachment reactions.

A use for raspberry particles was reported by Behme *et al* (2022)[161] who used them as a template for the production of microsieves. The raspberry particles were made by attaching silica shell particles to a larger glass core. These raspberries were then spread over water in a monolayer when a PMMA/toluene mixture was poured over the particle monolayer and left to dry. The raspberry particles were then etched away from the resulting PMMA/raspberry particle composite, leaving behind a PMMA matrix with hierarchal pore features that can be used as a microsieve.

Another interesting use for raspberry particles was reported by Zhang *et al* (2019).[162] In this paper, dithiothreitol-gold nanoclusters were able to interact with DNA in such a way that raspberry-like structures were formed. It was found that these raspberry structures were able to protect the incorporated DNA from hydrolysis via enzymatic attack from DNase I and showed high

biocompatibility, thus making them good contenders for gene delivery.Shirman *et al* (2018)[79] used evaporation-induced self-assembly to drive the assembly of raspberry particles from metal (gold, silver, platinum, etc.) shell particles and thiol-modified polystyrene core particles. These raspberry particles were then used as templates to create porous catalytic structures.

Raspberry particles can also be used in the production of core-shell particles. Core-shell particles consist of a thin shell of a material that fully coats a larger core particle; often this is metallic coatings on non-metallic substrates.[59,80,82-86,157-159,163-171] The production of these thin coatings can often be quite difficult, with many processes resulting in uneven coverage or coatings thicker than desired.[80,83-86,121] Raspberry particles have been used to help improve shell growth by providing very small seed particles on the larger core which act as nucleation points for deposition of further shell material, as shown in Figure 4.[59,80,82-86,121,157-159,163-171]

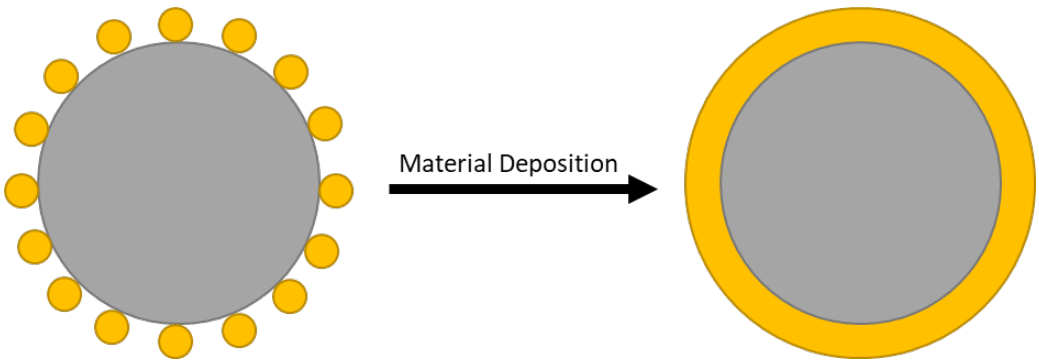

Figure 4: Schematic for the production of a core-shell particle using raspberry particles decorated with seeds.

Kim *et al* (2012)[167] produced Fe_3O_4-gold core-shell nanoparticles by first attaching gold seed nanoparticles to the iron oxide core via an APTMS layer. These composite particles retained the magnetic nature of the iron oxide core while gaining the photonic resonance of the gold shell. When a dispersion of these particles was placed in a magnetic field, the particles would arrange in 1D chains along the magnetic field lines due to the magnetic core while the gold shells prevented aggregation. This combination of a magnetic core with a gold coating in such defined arrays could have potential use in area of nanoscale electronics.

1.5.1 Superhydrophobic Coatings

One of the applications for raspberry particles is in the production of biomimetic lotus leaf coatings.[4-13,15,18,19,22,24-27] Although single-sized particle coatings have been shown to make hydrophobic coatings with high contact angles,[118,172] the true super hydrophobicity of the lotus leaf, with high contact angles (>150°) and low sliding angles (<10°)[173-177] can only be reliably achieved through coatings with two scales of roughness[8,178,179]. The hierarchal roughness of raspberry particles makes them a perfect

candidate for incorporation into these coatings.[25] This application is more thoroughly explored in Chapter 4: Thiol-Epoxy silica particle attachment.

1.5.1.1 Measuring Wettability

The hydrophobicity or hydrophilicity (also referred to as wettability) of a surface is normally determined by the water contact angle (WCA).[175,180] In these measurements, a water drop is placed on the surface of interest and the angle between the surface-liquid interface and the liquid-air interface is measured as shown in Figure 5 below.[175,180] Surfaces are said to be hydrophobic if θ>90° and vice versa.[175] Another important measurement when determining the wettability of the surface is the sliding angle (α). This is the angle at which a water drop will slide off the surface without sticking as shown in Figure 5.[174]

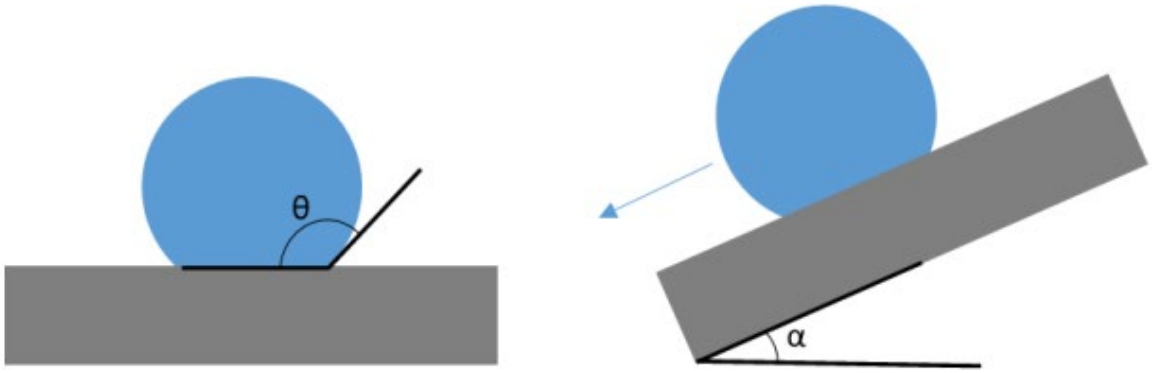

Figure 5: Diagrams of contact angle and sliding angle measurements

On a flat surface, the contact angle can be predicted by Young's equation (Equation 6)[174,175,180,181] where γ_{SA}, γ_{SL}, and γ_{LA} and are the surface energies of the solid-air, solid-liquid, and liquid-air interfaces respectively. Though this equation can be useful for simple modelling of water-surface-air interactions, it does not account for contact angle hysteresis, which is a result of inconsistencies in the surface chemistry or structure.[175,180]

Equation 6: Young's Equation

$$\cos\theta = \frac{\gamma_{SA} - \gamma_{SL}}{\gamma_{LA}}$$

1.5.1.2 Cassie and Wenzel Wetting

The wettability of surfaces with a single scale of roughness is greatly dependent on the morphology of the surface features. The Cassie and Wenzel states are the most commonly used models to predict how a drop will behave on a roughened surface.[174,178,180,181]

In the Wenzel state, the drop sinks down into the surface features as shown in Figure 6.[178,180] This increases the contact area between the drop and the surface substantially from an equivalent flat

surface which in turn results in high adhesion forces.[175] These high adhesion forces pin the water drop in place, resulting in high sliding angles.[178,180] The equation that relates the contact angle of a flat surface (θ) to a roughened surface (θ*) as given by the Wenzel method is shown in Equation 7 below,[178,180,181] where r_f is the surface roughness factor. When the original, flat surface is made of a hydrophobic material (i.e. θ>90°), the increased contact area between the drop and a rough surface of the same material results in an increase in the contact angle and vice versa. In other words, when θ>90° then θ*>θ, and when θ<90° then θ*<θ for all physically possible angles.[174,178,180]

Equation 7: Wenzel state contact angle of a rough surface

$$\cos(\theta^*) = r_f \cos(\theta)$$

In contrast, the Cassie state has the water drop sitting on top of the surface features rather than within them.[174,180] This results in the trapping of air bubbles between the grooves of the surface and the underside of the drop as seen in Figure 6. This results in a reduced contact area between the drop and the surface, which results in lowered adhesion forces. These lower adhesion forces allow the drop to slide off the rough surface at lower tilt angles than the equivalent flat surface.[172,174,180] The equation that relates θ* to θ for the Cassie Wetting state is given in Equation 8 below,[174,178,180] where f_s is the fraction of the surface in contact with the drop. From this equation it can be seen that θ*>θ for all possible θ.[174] Thus an increase in contact angle can be seen regardless of whether the original material is hydrophobic or hydrophilic.

Equation 8: Cassie state contact angle of a rough surface

$$\cos(\theta^*) = -1 + f_s(\cos(\theta) + 1)$$

The above models allow for the formation of very high contact angles from both the Wenzel and Cassie wetting states,[174] however only the Cassie state allows for the low sliding angles that are required for a truly superhydrophobic surface.[174,178,180]

Both the Cassie and Wenzel models are idealised extremes of the interaction between a drop and a rough surface and as such are not always able to explain experimental observations.[178,180] As such

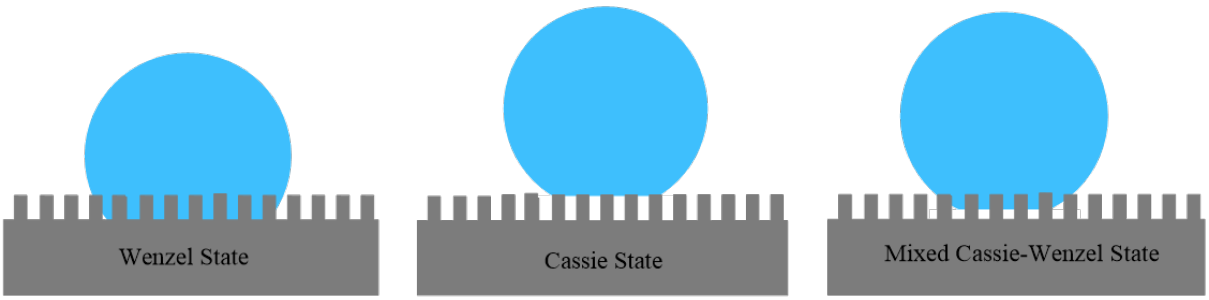

Figure 6: Behaviour of a drop on a rough surface as dictated by the Wenzel, Cassie, and Mixed Cassie-Wenzel states

Marmur (2003)[178] has proposed a mixed wetting state model where the drop partially sinks into the surface features while still trapping some air between the surface and the drop as shown in Figure 6.

When a surface has hierarchal roughness, there are two different scales of surface features that could interact with the drop almost independently. Either scale may be in the Cassie, Wenzel, or mixed Cassie-Wenzel states, which adds further complexity into the behaviour of water on these surfaces.

1.6 Nanoparticle Growth

Nanoparticles can be achieved through two broad approaches; top-down and bottom up.[108,121,182] In top down methods, a bulk material is broken down through a mechanical process such as milling, etching, blasting, etc. until nanomaterials are obtained.[121,182] This approach is usually quite simple, however the resultant nanoparticles are typically non-uniform with very little control over size or morphology.[182]

Bottom-up approaches offer more control over final particle size and morphology and are often simple to undertake.[108,182] However, the mechanism of particle growth can change depending on the desired chemical composition. Two major avenues are nucleation and emulsion growth.[108,182,183]

1.6.1 Nucleation-Growth

Classical Nucleation and Growth theory is a mathematical model that was first developed in order to model the Gibbs free energy of forming liquid droplets from a vapour phase.[183,184] However, this model has been adapted for the production of solid nanoparticles from liquid phases.[108,185]

The LaMer mechanism[121,184-189] is based on Classical Nucleation and Growth Theory, and was one of the first mechanisms proposed for the formation of nanoparticles.[108,184] It, along with its modifications, is one of the only widely accepted nanoparticle growth mechanisms.[108] In this mechanism, nucleation and growth are separated into two different stages,[108,184,190] with a total of three reaction phases.[184,191] In phase 1, the monomer is added to a reaction medium, which results in a sharp increase in monomer concentration.[108,184,190,191] In phase 2, when this concentration reaches a critical number through either supersaturation or change in temperature, the monomers undergo 'burst nucleation' to form nuclei.[108,184,185,190,191] This nucleation occurs very rapidly and dramatically reduces the concentration of monomer in solution, preventing further nucleation after this point.[108,184,185,190,191] The third phase is the growth phase where monomers from solution are added to the nuclei through a reaction of some sort.[108,184,190] This growth process is usually limited/controlled by the rate of monomer diffusion through the reaction medium.[108,184] These three phases are illustrated via monomer concentration over time in Figure 7 below.

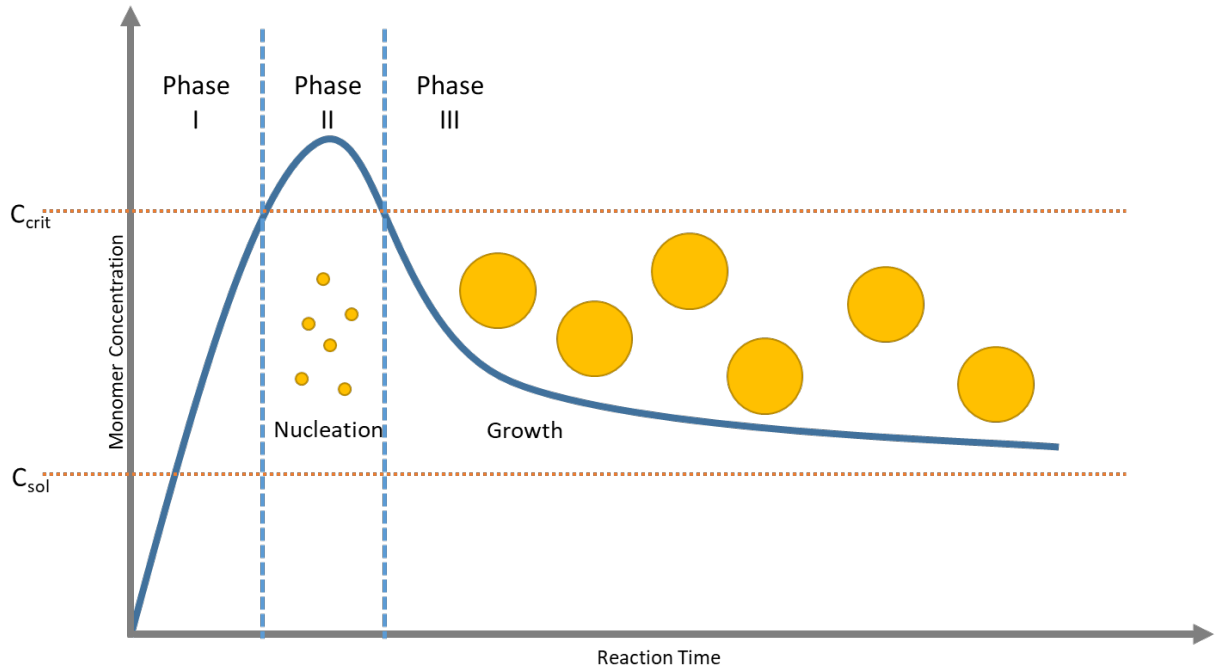

Figure 7: Particle nucleation and growth as described by the LaMer Mechanism. The curve represents the monomer concentration over time while the yellow represents the growing nanoparticles. C_{crit} is the critical concentration beyond which particle nucleation occurs. C_{sol} is the concentration below which the monomers are entirely soluble and no particle growth occurs.

There are several other proposed nucleation and growth mechanisms, including two-step mechanisms (where nucleation and growth occur concurrently),[183,184] Ostwald ripening,[184,191,192] digestive ripening,[184] intraparticle growth,[184] coalescence,[184] oriented attachment,[184] and pre-nucleation clusters.[183] More detailed explanations of these mechanisms, and others can be found in Thanh (2014)[184] and Wu (2022)[183].

1.6.2 Emulsion Particle Synthesis

In an emulsion nanoparticle synthesis reaction, the particle monomer is dispersed in an immiscible solvent, forming an emulsion of monomer droplets in the solvent.[108] The monomers, which are held in close proximity in the droplets, then rapidly coalesce into particles.[108]

Unfortunately, most emulsions are thermodynamically unstable[192] and as such, the Gibbs free energy of the system is decreased by coalescence of the monomer droplets.[192] If the emulsion is too unstable then this coalescence occurs before the monomers can polymerise to form a nanoparticle. In these cases, a surfactant or some other type of stabiliser is used to stabilise the emulsion to allow for the formation of nanoparticles.[192,193] Thus, the size and shape of the produced nanoparticles is mostly determined by the size of the emulsified droplets before they coalesce into particles, which is highly dependent on the presence, concentration, and composition of the stabilising agent.[192,193] This is unlike nucleation-growth mechanisms where the particle monomer is dissolved in an appropriate solvent, and the size and shape is more directly controlled by the monomer concentration.[194-198]

The most widely used application of emulsion particle synthesis is for the production of polymeric nanoparticles, more specifically called emulsion polymerisation.[192,193,199,200] In this method, hydrophobic monomers are dispersed in an aqueous medium (often with the assistance of surfactants) to form particles with average sizes in the range of 50-500 nm.[193,201] However, inverse emulsion polymerisation can also be used, where the monomers are polar and the solvent non-polar.[193,202]

Other methods of emulsion particle synthesis include microemulsion polymerisation, miniemulsion polymerisation, and emulsion-solvent evaporation. In microemulsion polymerisation, the monomer droplets are usually below 100 nm.[193,203-205] In miniemulsion polymerisation, the monomer droplets are formed through the application of high shear.[193,206-210] In emulsion-solvent evaporation, polymers (not monomers) in solvent are dispersed into a liquid medium before the droplet solvent is evaporated, leaving behind solid particles.[193,211-213]

A major downfall of emulsion methods is the presence of the surfactant at the surface of the final particles, which can be detrimental to further particle attachments or biocompatibility.[193,203,204,214]

1.6.3 Silica Nanoparticle Synthesis

Silica nanoparticles are of particular interest in a wide variety of fields due to their ease of synthesis, effective control over particle size, high monodispersity, and biocompatibility.[121] Silica particles can be produced from silane precursors by both nucleation-growth[121,195,198,215-217] and emulsion mechanisms,[115,121,215,218,219] though nucleation-growth is the most common.

1.6.3.1 Stöber Synthesis

The Stöber process is the one of the most predominant methods by which silica particles are synthesised. This method was first reported in 1968[217] and can produce monodispersed, spherical particles that range in size from nanoscale to microscale.[154,216,217,220-223]

In the Stöber process, the tetra-substituted silane precursor tetraethyl orthosilicate (TEOS) undergoes a series of hydrolysis and condensation reactions, eventually resulting in a large amorphous network.[121,216,217,224] Initially, the TEOS reacts with water in a hydrolysis reaction in which the ethoxy groups are replaced with hydroxyl groups.[121,216,224-226] These hydroxyl groups are then able to undergo condensation reactions with another hydrolysed molecule in order to form a Si-O-Si chain and water as a by-product.[121,216,224-226] These hydrolysis and condensation steps then continue until a large amorphous network is formed.[121,216,224-226]

The morphology of this network is controlled by a variety of factors including pH and temperature.[224,225] At high pH, the mechanism of the condensation reactions switches to a nucleophilic

attack mechanism wherein the hydroxyl group preferentially attacks the most electrophilic Si atoms.[121,224,225] It has been found that the electrophilicity of the Si atoms in these types of systems increases in the trend: Si-OH<Si-OEt<Si-O-Si, therefore the "internal" Si atoms are more likely to be attacked. [121,224] Consequently, the reaction mechanism under basic conditions favours the formation of a tetrahedral network, resulting in a spherical shape.[224] This reaction scheme is illustrated in Figure 8. However, this illustration is very simplified and does not show alternate pathways such as the occurrence multiple hydrolysis events before condensation.

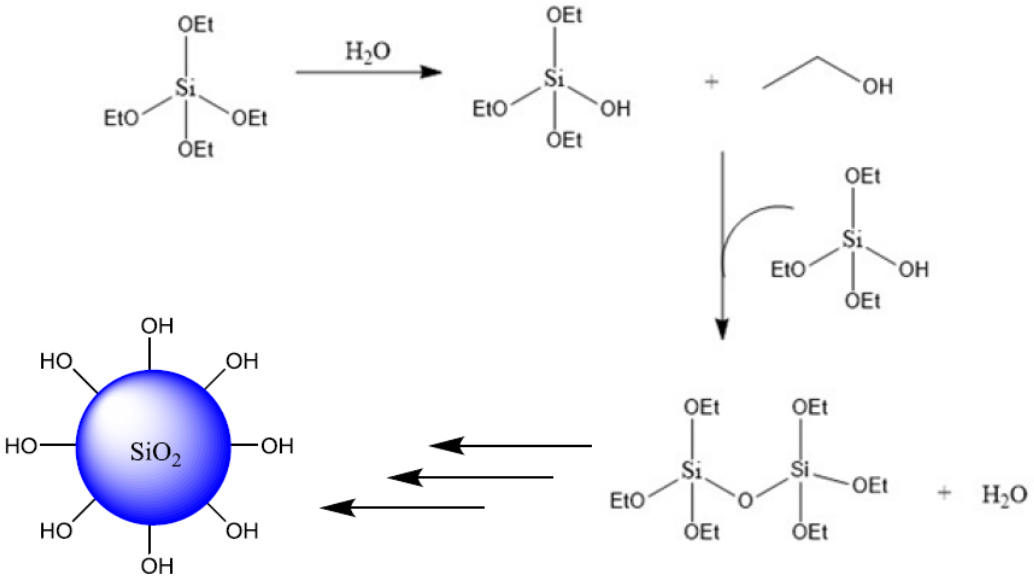

Figure 8: Simple Stöber process reaction schematic.

The Stöber process allows particle size to be easily controlled in the nano- and micro-size ranges through variations in TEOS concentration, ammonia concentration, and water content.[121,216,217,220,221,227,228] The effects of these variables on the final particle size can be modelled using Equation 9,[228] although this is a simplified model that doesn't take into account the interactions that may occur between reagents.[220]

Equation 9: Proposed model for Stöber process silica nanoparticle diameters (d) and the dependence on experimental conditions.

$$d = [H_2O]^2 e^{-B[H_2O]^{\frac{1}{2}}}$$

$$A = [TEOS]^{\frac{1}{2}}(82 + 151[NH_3] + 1200[NH_3]^2 - 366[NH_3]^3)$$

$$B = 1.05 + 0.523[NH_3] - 0.128[NH_3]^2$$

In order to increase the range of chemical reactions that can be done off the particle surfaces,[121] TEOS silica particles are often modified post-synthesis with a number of different silane molecules with different functional groups in the monomer structure, such as MPTMS, APTMS, and GPTMS.[80-82,84,85,121,150,158,164,171,229-231] These modifications are achieved by mixing the TEOS particles with the new silane in very similar (or the same) conditions as the original particle synthesis, resulting in addition of the new silane to the existing particle surfaces via a series of hydrolysis and condensation reactions.[80-82,84,85,121,158,164,171,230]

An alternative approach to post-synthesis modification is to use the functional silanes as the starting monomer in a modified Stöber process.[194-196,198,231,232] This produces silica particles with the desired functionality without the need for further reactions. Some examples of silica particles that have been achieved in this way have thiol,[194-196,198,231] epoxy,[197] and alkene[196] functional groups on their surfaces. These types of particles have also been shown to have good control over the final size through starting silane concentration.[195,198]

1.6.3.2 Surfactant Growth

Another method for the growth of silica particles is the incorporation of surfactants as templating agents.[115,117,121,214,215,218,219,233,234] In the presence of a surfactant, the hydrolysed silica precursor molecules form a micelle structure in which the condensation reactions occur to form the final particle.[218,234] The size of this micelle, and by extension the final particle size, can be altered by the type and concentration of the surfactant.[218,219,233,234] Ionic surfactants experience electrostatic interactions with the hydrolysed silica precursor molecules which in turn increases or decreases the size of the formed micelles for cationic and anionic surfactants respectively.[218] The use of surfactants results in the production of very monodispersed particles in much less time than the Stöber process, however there is less research into the effect of surfactants on the morphology of the final particles.[115,117,218,219] Additionally, the surfactant can be hard to remove from the particle surface,[115,214,219] resulting in interference with any particle surface attachment reactions.

1.6.4 Gold Nanoparticle synthesis

The most common method for the synthesis of gold nanoparticles is the Turkevich method.[81,157,164,165,171,235-244] This method was developed in 1951 by Turkervich[236] and modified in 1973 by Frens.[245] In this method chloroauric acid is reduced to metallic gold by the use of citric acid as both the reducing agent and stabilising ligand.[235,236] The ratio of the gold(III) ions to citric acid in the solution determines the final size of the gold particles, with an increasing gold:citrate ratio resulting in increased particle sizes and vice versa.[235] If the concentration of citrate becomes too low, there is not enough of the ligand to effectively stabilise the gold particles resulting in aggregation of the small

nanoparticles to larger particles overall. Gold particles ≤20 nm in diameter tend to be monodispersed, however particles >20 nm are usually not, as they form due to aggregation of smaller particles which is a less controlled growth method.[235] A modified Turkevich method can be used to produce monodispersed gold particles >20 nm via a two-step synthesis. In the first step, small gold particles are made. These particles are then used in the second step as seeds and are mixed with a solution containing more monomer and reducing agent, but in the correct ratio so that no new nucleation events occur and the gold is only deposited on the pre-existing seeds.[235,246]

The exact mechanism of gold particle growth in the Turkevich method is dependent on the pH of the solution. At low pH (approximately 3.7-6.5) the reduction reaction proceeds through a $[AuCl_3(OH)]^-$ intermediate and follows the LaMer burst nucleation mechanism, with nucleation only lasting approximately 10 seconds.[184] Once nucleation has occurred, there is a random rapid addition of monomers before the low concentration of monomer in solution switches the growth mechanism to intraparticle ripening and/or Ostwald growth.[184] At high pH (approximately 6.5-7.7) the intermediates are $[AuCl_2(OH)]_2^-$ and $[AuCl(OH)]_3^-$ and the nucleation occurs more slowly (approximately 60 seconds) before a slow addition of monomers from solution is observed. In both cases however, it is unclear whether the gold atoms are reducing first and then bonding together, or if the gold ions are bonding before reduction.[184]

Other reducing agents have been used in the production of gold particles from chloroauric acid, including sodium borohydride ($NaBH_4$)[247,248] and tetrakishydroxymethylphosphonium chloride (THPC),[82,85,158,163,166,167,169,170,238,249-251] however the mechanism of particle formation is less clear in the case of $NaBH_4$ as the reduction reaction occurs too rapidly to isolate any intermediate transition states.[235]

Of more interest in research is the use of different stabilising ligands, as the ligand can be used to control the final shape, size, solubility, assembly, and electronic transfer efficiency.[235] There are two general approaches to stability via ligands, charged and steric. Charged stability is achieved through use of charged ligands such as citric acid, where the ligand complexes to the gold particle in such a way that the outer surface is charged. This charged surface then results in electrostatic repulsion between particles to provide the desired stability.[235] However, charged stability is sensitive to changes in pH or addition of salts and may not be suitable to every application. Steric stability is achieved through the use of bulky molecules as stabilising ligands, preventing the gold particles from approaching each other and aggregating.[235] Alkanethiols are very commonly used as steric stabilisation ligands, where the thiol bonds to the surface of the gold while the long alkane chain extends out from the particle surface. Another commonly used ligand is THPC, which is also able to

act as a reducing agent for the gold chloride. THPC appears to be most commonly used when gold particles <5 nm are required.[82,85,158,163,166,167,169,170,238,249-251] Polymers, alcohols, ethers, amines, silanes, phosphines, disulphides, and surfactants can also be used as stabilising ligands.[168,235,252] These different ligands can either be incorporated into the gold particle production reaction, or they can be changed post-synthesis by ligand exchange reactions.[235,253,254]

1.7 Surface Modification

The surface properties of a material can be tailored through the modification of surface chemistry. This modification can be achieved on flat or particle surfaces through direct modification of the surface groups (i.e. by reduction or oxidation), or by attachment of another molecule with a different functionality. Examples of surface modification via attachment include the previously mentioned attachment of functional silanes to silica particles, [80-82,84,85,121,150,158,164,171,229-231] or the formation of self-assembled monolayers.[87-93]

In general, surface modification should be easy to achieve, be non-destructive to the original material, and be irreversible, in order to allow for their subsequent use.

1.7.1 Thiol Click chemistry

The term click chemistry is used to refer to reactions that are selective, insensitive to water and oxygen, have simplistic reaction conditions, and produce stereospecific products with high yields and purities.[255-257]

Thiol groups are of specific interest in click chemistry as they undergo reactions with a number of different functional groups such as alkenes, alkynes, isocyanates, epoxides, and halides[256-259] as illustrated in Figure 9. These reactions have been used frequently in materials and polymer science in the past.[255,256,260-262]

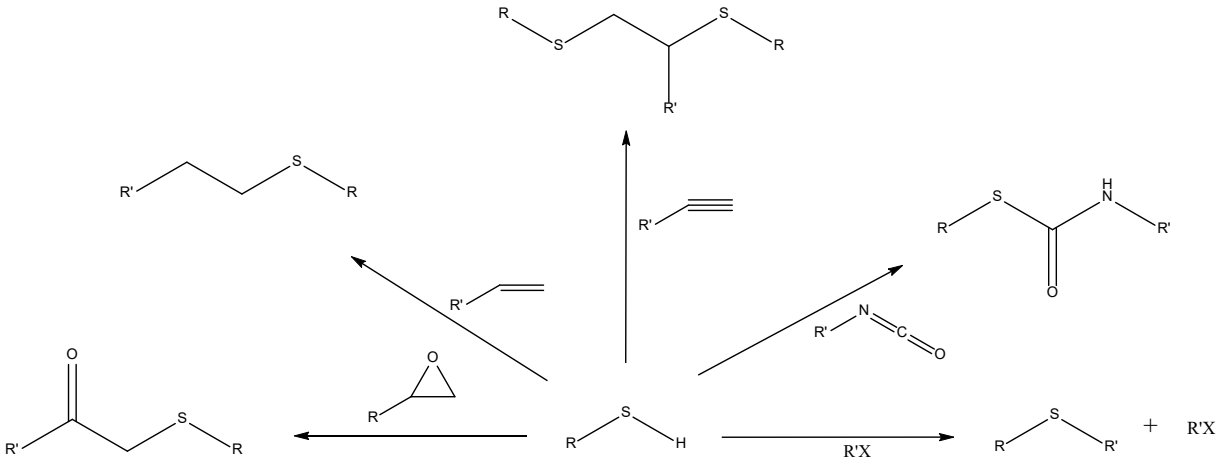

Figure 9: Variations of thiol click chemistry reactions

These thiol reactions generally use radical or nucleophilic attack mechanisms.[255-257,260-265] For instance thiol and epoxy functional groups react in a nucleophilic ring opening reaction to form a β-(hydroxyl)thioether[256,261,264,265] as illustrated in Figure 10. This reaction is self-propagating and effectively irreversible, making it ideal for the attachment or surface functionalisation of nanoparticles.

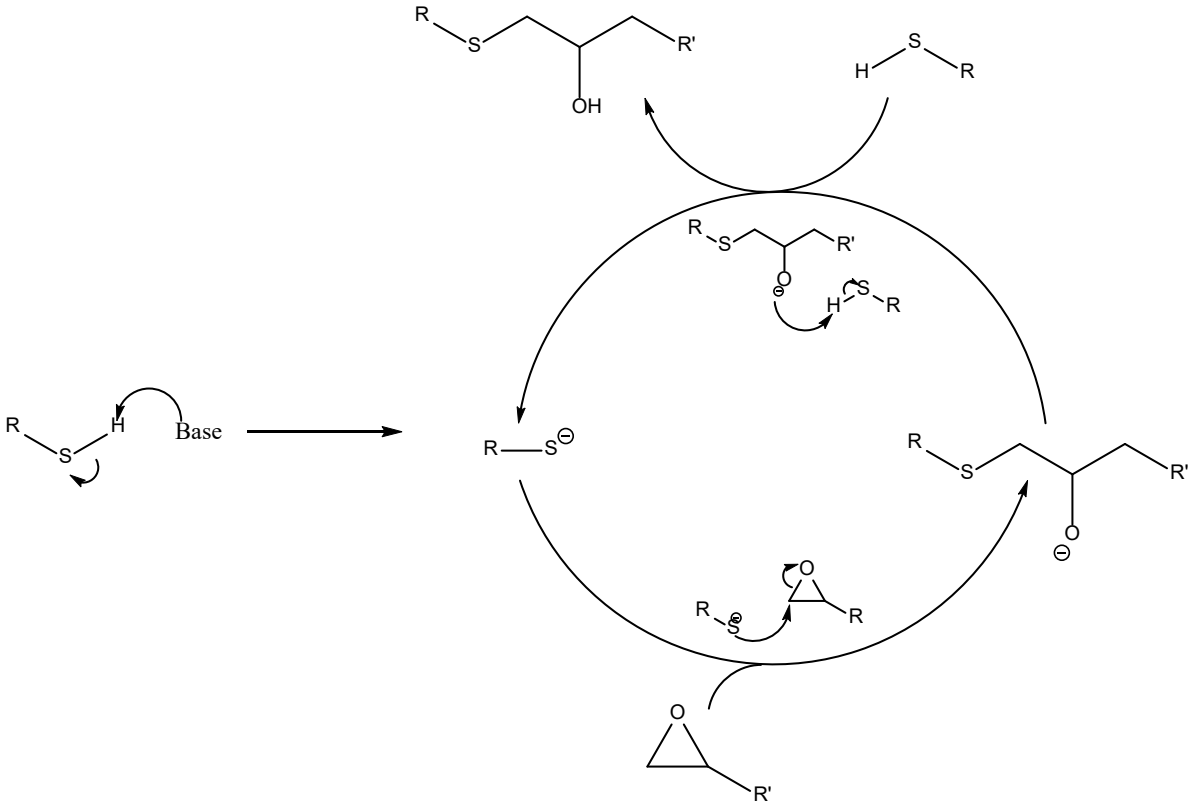

Figure 10: Thiol-epoxide base catalysed reaction schematic

1.8 Theory of Analytical Techniques

1.8.1 Scanning Electron Microscopy

Scanning Electron Microscopy (SEM) is a form of electron microscopy that is able to give high resolution imaging of nanoscale features.[266,267] In this technique, a beam of electrons with an energy of 2-40 keV is produced by an electron gun.[266,267] This beam is focused onto the sample surface through the use of electromagnetic lenses in a raster pattern, resulting in surface-electron interactions.[266,267] These interactions can give rise to secondary electrons, backscattered electrons, Auger electrons, and x-rays, all of which can be detected and used to give different types of information about the surface.[267] In particular secondary electrons can be used to give high resolution images in the x and y direction, as well as some information in the z direction due to the good depth of field.[267] This depth of field is able to be achieved as surface features that are closer to the detector (i.e. higher) will give

a stronger secondary electron signal.[267] However no actual analysis or quantitative information can be obtained for the z direction.[267]

1.8.2 Dynamic Light Scattering

In dynamic light scattering (DLS), a laser is shone through a suspension of nanoparticles and is scattered by the particles.[268-271] As particles in suspension will move due to Brownian motion, the scattered light will fluctuate and these fluctuations are detected to give the diffusion coefficient (D).[268-270] D can then be related to the hydrodynamic radius (R_h) of the particles via the Stokes-Einstein equation (Equation 10) where n is the dispersant viscosity, K is the Boltzmann constant, and T is the measurement temperature.[268-270] This relationship allows DLS to be used to measure nanoparticle size and distribution.

Equation 10: Stokes-Einstein Equation

$$D = \frac{KT}{6\pi n R_h}$$

1.8.3 Zeta Potential

When a charged particle is dispersed in a suspension, the counter ions in the surrounding solution will form an electric double layer.[269,272,273] The innermost of these layers (the Stern layer) has the counter ions tightly bound to the surface of the particle while the more mobile ions further from the particle surface exist within the diffuse region.[269,272,273] In the diffuse region there is a boundary that distinguishes the ions that will move with the particle as it moves, and the ions that will remain in the bulk solvent.[269,272,273] The term zeta potential refers to the electric potential at this boundary, which can be calculated from the electrophoretic mobility (measured by DLS) via the Henry or Smolochuski approximations.[269,272,273]

Zeta potential is used as a measure of colloidal stability[269,272,273] and can also be used as an approximation of the surface charge of the particle as they are approximately congruent.[273]

1.8.4 Ellman's Reagent

Ellman's reagent, also known by its chemical name as 5,5'-Dithiobis(2-nitrobenzoic acid) (DTNB), is an organic molecule with a disulphide group connecting two functionalised aromatic rings.[274-276] This disulphide is able to participate in thiol-exchange reactions with thiol groups as shown in Figure 11 below.[274-276] The resultant thiolate anion has a bright yellow colour, which enables it to be detected via UV-Vis spectroscopy.[274-276] This reaction is specific to thiol groups and allows for the quantitative detection of these thiol groups through the Beer-Lambert law via a calibration curve or the molar absorptivity.[274-276] This reaction is most commonly used in biological applications where it can be used

for determination of cysteine in proteins; as such it has standardised procedures and the molar absorptivity is well known.[274-276]

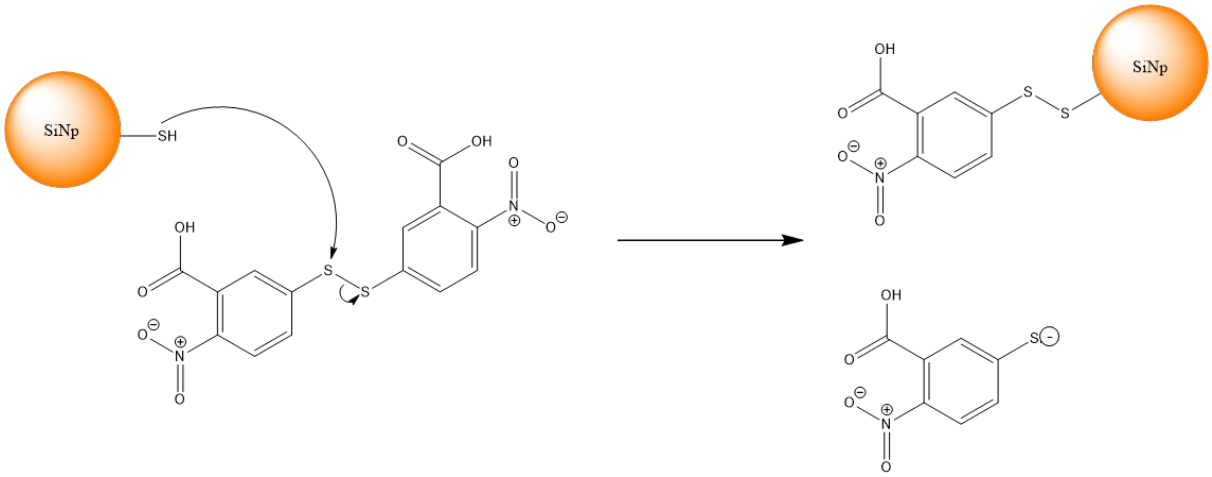

Figure 11: Mechanism for Ellman's reagent attachment to thiol-functionalised silica particles

1.8.5 UV-Vis Spectroscopy

In UV-Vis Spectroscopy, light of specific visible wavelengths is shone through a sample and the absorbance of this light is measured.[277] This measurement is able to then be repeated for a series of different wavelengths which enables the production of an absorption spectrum across the entire visible spectrum.[277] As colour is a result of absorption and reflectance of light of specific wavelengths, UV-Vis spectroscopy is very useful in the characterisation of coloured compounds.[277]

1.8.6 Attenuated Total Reflectance-Fourier Transform Infra-Red Spectroscopy

Infra-Red (IR) spectroscopy samples are able to absorb IR radiation at specific wavenumbers due to the vibration of bonds within the sample, provided that these vibrations result in a change in the dipole moment of the bond.[278,279] As the specific energy absorbed is dependent on the type of bond present this can be a powerful tool in chemical analysis.[278]

A specific form of IR spectroscopy is attenuated total reflectance-Fourier Transform Infra-Red (ATR-FTIR). In this set up, the sample is placed on a crystal with a high refractive index. An IR beam is then passed through the crystal at such an angle that total internal reflectance occurs at the sample-crystal interface.[278] This internal reflectance results in the formation of an evanescent wave that extends into the sample where it can be absorbed by the sample, depending on the bonds present.[278] The attenuated energy of the evanescent wave is then passed back to the IR beam where it can be detected and used to generate an IR spectrum.[278]

1.8.7 Raman Microscopy

Raman spectroscopy is an analytical technique that, like IR spectroscopy, is based on the interactions of light with the chemical bonds within a sample. Raman is considered a complimentary technique to IR, as most bonds or molecules that are Raman active are not IR active and vice versa.[279-283] In Raman spectroscopy, laser light is incident on a sample where it induces a change in polarizability in certain types of bonds.[279-283] This change in polarizability is monitored through measurement of the scattering of the incident light.[279-283]

The vast majority of scattering is elastic (i.e. there is no change in energy between the incident and scattered photons) and as such provides no information about the sample. This is known as Rayleigh scattering.[279,282] In some cases, the incident photon will promote the molecule to a virtual energy state before the molecule relaxes back to a vibrational state that is different to its original, unexcited state.[279-283] This relaxation results in the emission of a photon with a different energy than the incident photon. This shift in energy (and correlated shift in frequency) can be measured and relates to the vibrational or rotational state of the molecule, which in turn gives information about the bonds within the molecule, and the way it interacts with other molecules around it.[279-283]

In Raman microscopy, a microscope lens is used to focus the laser onto the sample.[280,282,283] This focus results in a high spatial resolution of a few micrometres or less.[282] This spatial resolution allows for the use of Raman mapping where Raman spectra can be measured at many different points across a sample or spot analysis where there is only a small area of interest.[280,282,283]

1.9 Research Aims

The main research aims of this thesis are to:

1. Gain a deeper understanding of the nature of the sulphur group contained within silica particles made from MPTMS, particularly the sulphur oxidation state. This includes a systematic analysis of how this oxidation state is affected by both the particle reaction method and the concentrations of reagents used.
2. Use silica particles synthesised from MPTMS and GPTMS to produce raspberry particles via thiol-epoxy click chemistry. This reaction method allows for an investigation into how the ratios of the nano- and micro-scale roughness affects surface wettability due to its combinatorial nature.
3. Use citrate-stabilised gold particles and both MPTMS and GPTMS silica particles to develop a new method of gold-silica particle-particle attachment with higher attachment densities than those previously achieved. Through development of this method a deeper understanding of the relative strengths of thiol-gold and disulphide-gold interactions was achieved, as well as

an understanding of the attachment efficiency of citrate-gold to amine-, to thiol-, and to disulphide-functionalised silica particles.

Chapter 2 Materials and Methods

2.1 Chemicals

All reagents are listed in Table 1 and were used as received.

Table 1: Chemicals used in this thesis

Chemical	Abbreviation	Purity/Grade	Supplier
(3-mercaptopropyl)trimethoxysilane	MPTMS	95%	Sigma Aldrich
(3-glycidoxypropyl)trimethoxysilane	GPTMS	≥98%	Sigma Aldrich
Acetonitrile	ACN	≥99.9%	Sigma Aldrich
Tetrahydrofuran (stabilised with BHT)	THF	99.6%	Chem Supply Australia
Ammonia Solution (25% in H_2O)	NH_4OH	25%	Chem Supply Australia
Chloroauric Acid	$HAuCl_4$	99.995%	Sigma Aldrich
Sodium citrate tribasic dihydrate		≥99.0%	Sigma Aldrich
Tributylphosphine	Bu_3P	97%	Sigma Aldrich
(3-aminopropyl)trimethoxysilane	APTMS	97%	Sigma Aldrich
Ethylene diamine		≥99%	Sigma Aldrich
3-methyl-1-butanethiol		≥97%	Sigma Aldrich
Diisoamyl disulphide		≥98%	Sigma Aldrich
Sodium Chloride	NaCl	99.7 %	Chem Supply Australia
Sodium dodecylbenzenesulfonate	SDBS	Technical grade	Sigma Aldrich
Sylgard 184 silicone elastomer base		8 g/L	Dow Corning
Sylgard 184 silicone elastomer curing agent		86 g/L	Dow Corning
Methanol	MeOH	99.9 %	Chem Supply Australia
Ethanol	EtOH	99.9%	Chem Supply Australia
Elemental Sulphur	S_8	Unknown	Industry Waste
Toluene		100%	Ace Chemical Company
Disuodium hydrogen phosphate	Na_2HPO_4	≥99.0%	Sigma Aldrich
Sodium phosphate monobasic	NaH_2PO_4	≥99.0%	Sigma Aldrich
5,5'-Dithiobis(2-nitrobenzoic acid)	DTNB	≥98%	Sigma Aldrich

2.2 MPTMS particle synthesis

2.2.1 MPTMS Modified Stöber Method

2.2.1.1 Method A

Silica particles were grown from MPTMS using a previously reported modified Stöber process.[194,195,198]

Water (800 mL, 44 mol, 80%v/v), ethanol (100 mL, 1.7 mol, 10%v/v) and ammonium hydroxide solution (25% NH_3, 100 mL, 1.03 mol NH_3, 10%v/v) were combined in a large container and left to stir gently so that not vortex was formed by stirring. MPTMS (2 mL, 10.7 mmol, 0.2 %v/v) was added to the stirring water/ethanol/ammonia mix and left to stir gently for approximately 45 minutes. After this time, the stirring speed was increased and the mixture was left to react for 3 days until it was cloudy.

The same method was also used to make smaller batches of MPTMS particles in a 50 mL centrifuge tube with the same proportions of reagents.

2.2.1.2 Method B

Silica particles were grown from MPTMS using a previously reported modified Stöber process.[196]

Water (800 mL, 44 mol, 80%v/v) and ammonium hydroxide solution (25% NH_3, 100 mL, 1.3 mol NH_3, 10%v/v) were combined in a large plastic container and left to stir at a moderate speed. A separate mixture of MPTMS (1 mL, 5.4 mmol, 0.1%v/v) and ethanol (100 mL, 1.7 mol, 10%v/v) was made and shaken to combine. The MPTMS/ethanol solution was then added to the stirring water/ammonia solution and left to stir rapidly for 3 days.

2.2.2 SDBS Surfactant Method

Silica particles were grown from MPTMS using a surfactant method.[117]

Ethanol (5 mL, 85.6 mmol, 35.5 %v/v) and Ammonium hydroxide solution (25% NH_3, 6.6 mL, 87.8 mmol NH_3, 46.8 %v/v) were mixed with SDBS (175 mg, 0.502 mmol) and left to stir at a high speed so that a large vortex is formed. MPTMS (2.5 mL, 13.5 mmol, 17.7%v/v) was added to this stirring solution and was left to react for 3 hours. After 10 minutes the solution was an opaque blue/white colour.

2.2.3 Synthesis of Particles with Different Diameters

The modified Stöber Process described in 2.2.1.1 Method A was repeated with varying concentrations of the MPTMS precursor to make particles with varied diameters. The specific reagent quantities used in the synthesis of each particle diameter are shown in Table 2 below.

Table 2: Reactant concentrations and resultant thiol-terminated silica particle diameters

Average particle diameter (nm)	MPTMS		H_2O	Ethanol	Ammonia solution (25%)
	mL	mM	L	L	L
38	0.4	2.15	0.800	0.1	0.1
98	1.0	5.38	0.800	0.1	0.1
143	2.0	10.75	0.800	0.1	0.1
220	4.0	21.45	0.800	0.1	0.1
235	6.0	32.1	0.800	0.1	0.1

2.2.4 Effect of Ammonia Concentration on MPTMS Particle Growth

The modified Stöber processes described in 2.2.1.1 Method A and 2.2.1.2 Method B were repeated with varying concentrations of the ammonium hydroxide solution. The final quantities used are shown in Table 3 below.

Table 3: Reaction solutions with varying Ammonia Quantities.

MPTMS (mL)	25% Ammonium Hydroxide (mL)	Ethanol (mL)	Water (mL)
0.02	0.5	1	8.5
0.02	1	1	8
0.02	1.5	1	7.5
0.02	2	1	7
2	100	100	800

2.2.5 Effect of Ethanol Concentration on MPTMS Particle Growth

The modified Stöber processes described in 2.2.1.1 Method A and 2.2.1.2 Method B were repeated with varying quantities of ethanol. The final quantities used are shown in Table 4 below.

Table 4: Reaction solutions with varying Ethanol Quantities.

MPTMS (mL)	25% Ammonium Hydroxide (mL)	Ethanol (mL)	Water (mL)
0.02	1	0.5	8.5
0.02	1	1	8
0.02	1	1.5	7.5
0.02	1	2	7

2.2.6 Particle Cleaning Methods

2.2.6.1 Centrifuge

MPTMS silica particle suspensions were cleaned by first centrifuging at 4500 rpm (3984 g) for 2 hours using a Sigma 3-16 PK centrifuge. The resultant supernatant was discarded and the pellets were redispersed in 2 mL of water. This dispersion was then centrifuged at 13400 rpm (12100 g) for 30 minutes using an Eppendorf Minispin before the resultant supernatant was discarded. These redispersion and centrifuge steps were then repeated a minimum of three times in either water, ethanol, or acetonitrile depending on the subsequent use of the particles, with the solvents matching.

2.2.6.2 Salt

The particles were isolated by adding NaCl salt to the reaction mix to cause agglomeration of the particles, no specific quantities of salt were used and it was just added until agglomeration occurred. The agglomerated particles were then collected via ultra-vacuum filtration using Millipore S-PAK 0.45 µm membrane filters. While the particles were sitting on the filter, they were rinsed with water to remove residual NaCl before the particles were redispersed in H_2O.

2.2.6.3 Bubbled with Air

The MPTMS particle reaction mixture was bubbled with compressed air for 1 day to remove the NH_3 from the mixture and cause the particles to destabilise. The particles were then collected via ultra-vacuum filtration using Millipore S-PAK 0.45 µm membrane filters. While the particles were sitting on the filter, they were rinsed with water before the particles were redispersed in H_2O.

2.2.7 Effect of Atmospheric Oxygen on MPTMS Particle Synthesis

The modified Stöber Process described in 2.2.1.1 Method A was repeated with the following changes.

Water (8 mL, 0.444 mol, 80%v/v) and ethanol (1 mL, 17.1 mmol, 10%v/v) were bubbled with N_2 for 3 hours to remove atmospheric oxygen. The ammonium hydroxide solution (25% NH_3, 1 mL, 13.3 mmol NH_3 10%v/v) was then added to the water/ethanol mixture and was left to stir slowly without the formation of a vortex. MPTMS (20 µL, 0.108 mmol, 0.2%v/v) was then added to the stirring water/ethanol/ammonia solution which was left to stir slowly for approximately 45 minutes. The stirring speed was then increased and the solution was left to stir for 3 days until cloudy.

2.3 Reduction of disulphides at MPTMS Particle Surface

Previously prepared MPTMS particles were reacted with tributylphospene to reduce the surface dithiol groups to thiols. This reaction method was adapted from small molecule chemistry[284,285] but has not, to the best of my knowledge, been applied to particle surfaces.

A suspension of MPTMS particles in water (0.5 mL, 141.6 mg/mL, 70.8 mg particles) was added to a 50 mL 2-necked round bottom flask. Water (10 mL) and ethanol (5 mL) were added to the flask and the mixture was bubbled with nitrogen for 70 minutes while stirring. Tributylphosphine (0.1 mL, 0.405 mmol) was added to the stirring solution under a N_2 atmosphere. This was then left to react at room temperature for approximately 1.5 hours. A solution of elemental sulphur (S_8) in toluene (10 mL) was added to the solution to quench the reaction which was left to stir for 30 minutes. The flask was then opened to the air and the solution was moved to a separating funnel. The cloudy white layer was isolated and centrifuged at 13400 rpm for 30 minutes using an Eppendorf minspin to collect the particles. The supernatant was disposed and the pellet was redispersed in ethanol. This cleaning step was repeated a total of three times before the particles were analysed via an Ellman's reagent assay and Raman microscopy.

2.4 Ellman's Reagent Assay

2.4.1 Phosphate Buffer Preparation

Na_2HPO_4 (1.41723 g, 10.0 mmol) and NaH_2PO_4 (0.19206 g, 1.60 mmol) were dissolved in water (0.100 L) to make a phosphate buffer with a pH of 8 and a concentration of 0.1 M.

2.4.2 DTNB solution Preparation

DTNB (39.88 mg, 0.1006 mmol) was dissolved in the previously prepared phosphate buffer (100 mL) to make a 1.01 mM solution. This was then diluted to 0.101 mM for further use.

2.4.3 MPTMS particle Solution Preparation

Dried MPTMS particles (0.5-3.0 mg) were redispersed the previously prepared phosphate buffer (0.5 mL, 0.1 M, pH 8) via sonication.

2.4.4 Ellman's Reagent Assay

The redispersed particle solutions (0.1 mL) were combined with the Ellman's Reagent solution (2 mL, 1.01 mM, 2.02 µmol) and left to react for 30 minutes in a dark room. The reaction solutions were centrifuged at 13400 rpm for 30 minutes using an Eppendorf Minispin and the resultant supernatant was analysed via UV-Vis analysis.

2.5 Effect of pH on MPTMS Particle Surface Charge

A pH 14 solution was made by mixing ammonium hydroxide (25% NH_3, 3.846 mL) in an aqueous NaCl solution (4 mM NaCl, 1.154 mL). This solution was then used for a series of 1:10 dilutions to create pH solutions of pH 13-8. A pH 1 solution of HCl (0.1 M) was also made in the aqueous salt solution (4 mM NaCl). This solution was then used for a series of 1:10 dilutions to create pH solutions of pH 2-6. Water was used as a pH 7 solution.

A drop of MPTMS particle suspension (150.0 mg/mL) in water was added to each pH solution and the zeta potential of each sample was measured.

2.6 GPTMS Particle Synthesis

2.6.1 GPTMS Modified Stöber Method

Silica particles were grown from GPTMS using a previously reported process.[197]

Epoxide-functionalised silica particles were synthesised by adding GPTMS (10.0 mL, 45.3 mmol, 2.0%v/v) to a mixture of 25% ammonia solution (10.0 mL, 0.133 mol NH_3, 2.0%v/v) and Milli-Q water (490.0 mL, 27.21 mol, 96%v/v). This mixture was shaken and then left to sit for 18 hours. These particles were found to have an average diameter of 2.174 ±0.265 µm

2.6.2 Cleaning Method

The resultant particles were collected via ultravacuum filtration using a Millipore S-PAK 0.45 µm membrane filter and dispersed in 10 mL of water.

The particles were cleaned by centrifuging at 4500 rpm (3984 g) for 30 minutes using a Sigma 3-16 PK centrifuge before redispersing in 10 mL of water. The cleaning step was repeated three times.

2.7 GPTMS Particle Amine Functionalisation

A previously prepared ethylene diamine solution (14 mL, 16.41 mM, 23.0 µmol) was added to a suspension of GPTMS particles in water (0.1 mL, 8.96 mg particles, 89.6 mg/mL) in a centrifuge tube. This mixture was left to stir at room temperature overnight. The resultant reaction mixture was centrifuged at 4500 (3984 g) rpm for 30 minutes using a Sigma 3-16 PK centrifuge before the

supernatant was discarded. The pellet was redispersed in water (2 mL) and centrifuged at 13400 rpm (12100 g) for 30 minutes using an Eppendorf Minispin; this was repeated two times.

2.8 MPTMS-GPTMS Raspberry Particle Attachment

2.8.1 Raspberry attachment Reaction

A pH 14 acetonitrile solution was made by combining ammonium hydroxide solution (25% NH_3, 7.692 mL) and acetonitrile (2.308 mL). The pH 14 solution was then diluted to pH 11 via serial dilution with acetonitrile as the solvent.

GPTMS particles (20 mg) and MPTMS particles (50 mg) were dispersed in the pH 11 acetonitrile solution (0.8 mL) via sonication. This reaction mixture was then left to stir for approximately 40 hours to allow the reaction to occur.

The reacted particles were centrifuged at 13000 rpm (12100 g) for 30 minutes using an Eppendorf Minispin and the supernatant discarded to remove the triethylamine. They were then centrifuged 3 times at 13000 rpm (12100 g) for 30 seconds and 3 times at 5000 rpm (1683 g) for 30 seconds in order to remove the unreacted thiol particles. After each centrifuge step the resultant pellet was redispersed in acetonitrile.

2.8.2 Effect of Particle Concentration on Attachment Density

The method described in 2.8.1 Raspberry attachment Reaction above was repeated with varied amounts of pH 11 acetonitrile solution added to produce different particle concentrations. These concentrations were 0.58%w, 2.87%w, 7.07%w, 10.09%w, and 13.3%w.

2.8.3 Attachment of Different Sized MPTMS Particles

The method described in 2.8.1 Raspberry attachment Reaction above was repeated with MPTMS particles of different diameters. A summary of the particle sizes and reaction mixtures used are shown in Table 5 below. All GPTMS particles used in this experiment were from the same batch.

Table 5: Particle dispersions used for attachment reactions of MPTMS particle with different diameters.

Average thiol-terminated particle diameter (nm)	Thiol-terminated particles (mg)	Epoxide-terminated particles (mg)	pH 11 Acetonitrile solution (mL)	Final solids concentration (%w/w)
38	50.5	42.1	0.823	11.3
98	115	23.5	1.618	9.06
143	184	40	1.701	13.3

220	340	53	1.776	20.7
235	468	61.6	1.808	25.6

2.9 Raspberry Particle Coatings

2.9.1 General Coating Method

Dried raspberry particles were dispersed in THF via sonication for a final particle concentration of 100 mg/mL (10.1%w).

A solution of PDMS in THF was made by combining the Dowsil Silicone elastomer base (1158.94 g) and curing agent (120.56 g) in THF (10.0 mL) and leaving it to stir for 3 hours, resulting in a final solids concentration of 127.95 mg/mL (12.6%w).

The particle solution (50.0 µL, 5 mg particles) was mixed with the PDMS solution (16.6 µL, 2.12 mg PDMS). An additional aliquot of THF (85 µL) was added to make a solution with a final total solids concentration of 47.0 mg/mL or 5.02%w (33.0 mg particles, 3.52%w particles, 14.0 mg PDMS, 1.50%w PDMS).

A glass microscope slide was cleaned by sonicating it in methanol for 30 minutes before it was dried with nitrogen. A coating area of *c.a.* 2.5 cm^2 was then created on the slide by placing two pieces of scotch tape crosswise across the slide, parallel to each other at approximately 1 cm apart.

A sample of the particle/PDMS/THF solution (0.1 mL) was dropped onto the top edge of the coating area and a razor blade was used to draw the solution down over the entire coating area. This draw casted solution was then left to dry at room temperature for 30 minutes before it was placed in a 65°C oven overnight to cure.

2.9.2 Effect of Particle:Polymer Mass Ratio

The method described in 2.9.1 General Coating Method was repeated with varied particle:polymer mass ratios; as shown in Table 6 below.

Table 6: Composition of coating solutions with varied particle:PDMS ratios.

Total Volume THF	Raspberry Particles			PDMS			Total Solids Concentration		Particle:PDMS mass ratio
µL	mg	mg/mL	%w	mg	mg/mL	%w	mg/mL	%w	
150	0	0	0	7.05	47.0	5.02	47.0	5.02	0:1
213	5	15.7	2.51	10	31.3	3.34	47.0	5.02	0.5:1
319	5	23.5	1.67	5	23.5	2.51	47.0	5.02	1:1
88.7	2.5	28.2	3.01	1.67	18.8	2.01	47.0	5.02	1.5:1
151.6	5	33.0	3.52	2.12	14.0	1.50	47.0	5.02	2.4:1
142	5	35.2	3.77	1.67	11.8	1.26	47.0	5.02	3:1

2.9.3 Effect of Particle Size Ratio

The method described in 2.9.1 General Coating Method was repeated with raspberry particles with differently sized MPTMS particles (as made in 2.8.3 Attachment of Different Sized MPTMS Particles).

2.10 Gold Particle Synthesis

Citrate stabilised gold nanoparticles were made using the Turkevich method[236] as follows.

Chloroauric acid (400.75 mg, 1.179 mmol) was dissolved in water (1.00 L) before being heated until boiling while stirring. Sodium citrate tribasic dihydrate (1.225 g, 4.166 mmol) was dissolved in water (100.0 mL) before it was added to the boiling chloroauric acid solution. This mixture was left to boil and stir for approximately 15 minutes, until the solution changed colour from yellow to a deep red.

2.11 Gold Particle Ligand Swap

2.11.1 Citric Acid to 3-Methyl Butanethiol

A sample of the gold reaction solution (200 mL) was concentrated to 50x the reaction mix by centrifuging the particles at 13400 rpm (12100 g) for 30 minutes using an Eppendorf Minispin and redispersing the pellet in water (2 mL).

The concentrated gold particle solution (0.200 mL) was added to a solution of 3-methyl butanethiol in ethanol (2.00 mL, 10.8 mM, 22 µmol). This mixture was left to react for 2 hours before the solution was centrifuged at 13400 rpm (12100 g) for 30 minutes using an Eppendorf Minispin. The supernatant was discarded and the pellet redispersed in ethanol. This centrifuge step was repeated another 2 times.

2.11.2 Citric Acid to Diisoamyl Disulphide

The method described in 2.11.1 Citric Acid to 3-Methyl Butanethiol was repeated using diisoamyl disulphide instead of 3-methyl butane thiol.

2.11.3 Citric Acid to Ethylene Diamine

The concentrated gold particle solution made in section 2.11.1 Citric Acid to 3-Methyl Butanethiol was added to a solution of ethylene diamine in water (2.00 mL, 1.641 mM, 3.282 µmol). This mixture was left to react for 2 hours before the solution was centrifuged at 13400 rpm (12100 g) for 30 minutes using an Eppendorf Minispin. The supernatant was discarded and the pellet redispersed in water. This centrifuge step was repeated another 2 times.

2.12 Glass Functionalisation

1%v solutions of APTMS and MPTMS were made in methanol. The glass slides were cleaned by sonicating in methanol for 15 minutes before they were placed in the MPTMS or APTMS solutions for 1 hour. The functionalised slides were then rinsed with methanol and water before being stored in water for future use.

2.13 Gold Particle Attachments

2.13.1 Gold-Glass Attachment

Functionalised glass slides were left to sit in the aqueous gold particle solutions for at least 30 minutes at room temperature before rinsing with water to remove unattached gold particles. The slides were then stored in water-filled cuvettes for UV-Vis analysis.

The above method was repeated with reaction times of 1, 2, 4, 24, and 48 hours. The 1 hour and 2 hour reactions were then also repeated at 60°C and 80°C by suspending the reaction vessels in water baths set to the appropriate temperatures.

A sample of the concentrated gold solution made in 2.11.1 Citric Acid to 3-Methyl Butanethiol was dropped onto glass slides which were heated to 60°C on a hotplate. The water was left to evaporate and a film of gold particles was left on the glass slide.

2.13.2 Gold-Epoxy Attachment

2.13.2.1 Scheme 1

The diethylene amine functionalised gold particles (1.00 mL) from 2.11.3 Citric Acid to Ethylene Diamine were added to a suspension of GPTMS particles (0.020 mL, 1.19 mg particles). This mixture was left to stir overnight at room temperature.

The reacted particles were centrifuged at 13000 rpm (12100 g) for 30 minutes using an Eppendorf Minispin and the supernatant discarded. They were then centrifuged 3 times at 2000 rpm (269 g) for 30 seconds in order to remove the unreacted gold particles. After each centrifuge step, the resultant pellet was redispersed in water.

2.13.2.2 Scheme 2

A suspension of GPTMS particles (8.96 mg) in water was added to the ethylene diamine solution (14 mL, 16 mM, 0.224 mmol) made in 2.11.3 Citric Acid to Ethylene Diamine. This mixture was left to stir overnight at room temperature overnight. The particles were cleaned by centrifuging at 4500 rpm (3984 g) for 30 minutes using a Sigma 3-16 PK centrifuge before redispersing in 2 mL of water. The cleaning step was repeated three times.

The concentrated gold particles (1.00 mL) from 2.11.1 Citric Acid to 3-Methyl Butanethiol were added to a suspension of the ethylene diamine functionalised GPTMS particles (0.025 mL, 4.50 mg particles) in water. This mixture was left to stir overnight at room temperature.

The reacted particles were centrifuged at 13000 rpm (12100 g) for 30 minutes using an Eppendorf Minispin and the supernatant discarded. They were then centrifuged 3 times at 2000 rpm (269 g) for 30 seconds in order to remove the unreacted gold particles. After each centrifuge step the resultant pellet was redispersed in water.

2.14 Characterisation and Instrumentation

2.14.1 Sputter Coating

A drop of MPTMS or GPTMS silica particle solution was left to dry on a small silicon wafer overnight before analysis. This sample was then coated with 5 nm Pt via an EmiTech K575X sputter coater. A sputter current of 25 mA and a tool factor of 8.5 were used.

Gold particles were also dropped onto a small silicon wafer and left to dry for analysis. However, they were not sputter coated as gold is already conductive. All particle-polymer coatings were coated with 25 nm of Pt using the same instrumentation as described above.

2.14.2 SEM Imaging

An Inspect FEI SEM accelerating voltage of 5 kV and a spot size of 3 was used to take SEM images of the samples at varying magnifications.

2.14.3 Characterisation of Particle-on-Particle Attachment Density

The attachment density was characterised as the number of small-attached particles per unit area of the larger core particle. The attachment density was also compared to a calculated “theoretical

maximum" attachment density based on the sizes of the thiol- and epoxide-functionalised silica particles.

2.14.4 Raman Microscopy

Particle samples were dried 0.5mL of solution was dried in the 60° overnight. A sample of the dried particle powder was then deposited onto a glass microscope slide for analysis with a Witec Raman microscope. Each spectrum was taken with a 532 nm laser, a 600t grating, 30 second acquisition time, 10 accumulations, a spectrum range of 100-3750 nm, a laser filter of 50%, a slit of 100, and a hole of 100.

2.14.5 FTIR Spectroscopy

FTIR spectra of dried samples of gold nanoparticles were taken using a Perkin Elmer Frontier Spectrometer. The range was set to 600-3600 cm^{-1} and the resolution was 1 cm^{-1}.

2.14.6 UV-Vis Spectroscopy

A Varian Cary 50 Scan UV Visible Spectrophotometer was used for UV-Vis spectra collection in with a wavelength range of 200-800 nm at a scan rate of 4800 nm/min and a scan interval of 1 nm.

For analysis of the Ellman's Reagent assays, a sample of the phosphate buffer was used as a blank and a sample of the 1.01 mM DTNB solution was used as a control.

For gold particle solution analysis, water or ethanol were used as a blank depending on the solvent of the dispersion.

For coating analysis, a clean glass slide was used as a blank.

2.14.7 Zeta Potential

The Zeta potential of particle solutions was measured using a Malvern Zetasizer. The Smoluchowski model was used with a F(ka) value of 1.5. The temperature was set to 25°C with an equilibration time of 120 seconds. The dispersant was set as water or ethanol depending on the solvent of the sample. The measurement duration was set to automatic with a range of 10-100 runs, with 3 measurements total.

2.14.8 Dynamic Light Scattering

The DLS of particle solutions was measured using a Malvern Zetasizer. The Mark-Houwink used were A=0.428 and K= 7.67 x 10^{-5} cm^2/s. The temperature was set to 25°C with an equilibration time of 120 seconds. The dispersant was set as water or ethanol depending on the solvent of the sample. The measurement duration was set to automatic with a range of 10-100 runs, with 3 measurements total.

2.14.9 Water Contact Angle Measurement

Water droplets of approximately 40 µL were placed at three different locations on each coating and the resultant contact angles were measured using a Basler CCD camera and Basler Microscopy Software.

2.14.10 Sliding Angle Measurement

A 40 µL drop of water was placed on the coated surface, at which point the stage was tilted until the droplet slid off. The change in height of the lifted side of the stage from flat to tilt was then used in conjunction with the width of the stage to calculate the sliding angle using right angles triangle trigonometry.

Chapter 3: MPTMS particle surface chemistry

3.1 Summary

In this chapter, the sulphur state of silica particles grown from MPTMS via a modified Stöber method was examined. The particles were analysed for thiols and disulphide groups both through the bulk of the particle and at the surface via Raman spectroscopy, Ellman's reagent assays, and UV-Vis spectroscopy.

The effect of different reaction methods and reagent concentrations on the relative concentrations of thiols and disulphides in the particles was systematically investigated and this information was used to assign a mechanism to the formation of the disulphide groups during the particle synthesis reaction.

A method was also developed for the reduction of disulphide groups at the particle surface to thiols, for use in further reactions.

3.2 Introduction

Over the last decade, the development of thiol-functionalised silica particles has become an important part of research in fields such as medical research[286] and wastewater remediation.[231,287-289] These particles offer the potential benefit of providing a wide range of chemical reactions from the relatively easy to react thiol groups on the surface, particularly in the use of thiol click chemistry.[255-265]

There are several different methods for the synthesis of these "thiol-functionalised silica" particles from MPTMS, which can broadly be categorised by the following general synthetic approaches:

(i) Making silica particles grown from the tetraethylorthosilicate (TEOS) precursor via traditional or modified Stöber processes. These particles are then coated with a layer of MPTMS to introduce the sulphur groups at and near the surface of the particles.[121,287,289-292] This method can often result in non-uniform surface coatings of the particles.[80]

(ii) The co-condensation of TEOS and MPTMS in a reaction mixture, where the two precursors are added simultaneously.[121,288,293-298]

(iii) The self-condensation of MPTMS without the presence of any other silanes.[195,198,217,227,232,286,299] This method is attractive as it incorporates functional groups at the surface, which are much more reactive than the OH groups of a regular Stöber method.[194]

While it is reasonable to assume that particles made using these approaches will deliver particles with free thiol groups, there are reports of the formation of disulphides either inside or on the surface of these particles.[286,288,298,300]

Often, the resultant particles are analysed by FTIR and/or EDAX, which can confirm the presence of thiol groups and sulphur respectively.[287,289-292,295,297] However, neither of these methods are capable of determining whether or not disulphides have been formed and it is often assumed that no such oxidation has taken place.

The distinction between thiol or disulphide groups, particularly at the surface of the particles, can be very important for a number of different applications such as heavy metal ion capture, which is more efficient in the presence of thiols that can utilise ion exchange mechanisms.[289,298]

Some authors have observed the presence of disulphides in MPTMS particles.[288,293,294,296,298,299,301] However, the ratio of thiols to disulphides on the surface of the particles varies from publication to publication as both the general method (post-, co-, or self-condensation) and the more specific reaction conditions change. As these papers are usually independent studies looking at one sample of these modified silica particles, there has been no systematic analysis of the relationship between synthesis conditions, post synthesis cleaning, and particle chemical composition.

Al Mahrooqi (2018) reported a semi-systematic investigation of thiol/disulphide presence with different specific reaction conditions using a self-condensation method via Ellman's reagent assays.[299] However, The primary focus of the study was on size control and not all of the samples appear to have been analysed in this way. They also made the assumption that all disulphide bridges would be internal and that all sulphur present at the surface would be thiol groups. In addition to these limitations, they utilised organic solvents (predominantly DMSO) instead of the vastly more popular aqueous/alcohol mixtures.

In this chapter, we present a systematic study of the changes in sulphur oxidation state with changing reaction conditions during an aqueous self-condensation synthesis method, and investigate the validity of a mechanism previously proposed for disulphide formation in small molecules.

3.3 Methods

The methods relevant to this chapter are described in the following sections:

2.2 MPTMS particle synthesis, 2.3 Reduction of disulphides at MPTMS Particle Surface, 2.4 Ellman's Reagent Assay, 2.14.1 Sputter Coating, 2.14.2 SEM Imaging, 2.14.4 Raman Microscopy, and 2.14.6 UV-Vis Spectroscopy

3.4 Results/Discussion

3.4.1 Established that disulphides are present

3.4.1.1 Raman spectroscopy

In order to test how the thiol group is present once the MPTMS has been made into a particle, Raman spectra were taken of MPTMS particles, the MPTMS monomer, TEOS particles that have a plain SiO_2 matrix after hydrolysis and condensation, and VTES particles that have a $SiO_{1.5}$ matrix with a propylene side chain. Figure 12 a) shows a low-resolution full Raman spectrum while Figure 12 b) shows a higher resolution spectrum from 450 cm^{-1} to 700 cm^{-1}. The thiol group at approx. 2500cm^{-1} [302] was present in the MPTMS sample, but was non-existent in the spectrum of the particles made from MPTMS. When taking a higher resolution spectrum at 450-750 cm^{-1}, a major peak can be seen at 508 and 519cm^{-1} that are not present in any other samples (and as such is not due to the silica matrix which can show peaks in this area[303]) and are consistent with literature values for disulphide bonds.[302,304] There are also some peaks at 634 cm^{-1} and 693 cm^{-1} that were assigned to C-S-C bonds and a peak at 650 cm^{-1} that appears to be due to the $SiO_{1.5}$ matrix. This is strong evidence that the MPTMS does not form disulphide groups when left exposed to air, but this is instead a result of the particle synthesis reaction. In addition, the lack of thiol peak in the MPTMS particle spectrum implies that the reduction of thiols to disulphides has occurred throughout the entire particle and is not restricted to the particle surface. This in turn implies that the thiol reduction and particle synthesis reactions are occurring simultaneously. It is also important to note that the disulphide bonds do not appear to form between particles, as no agglomeration of particles was observed during synthesis or cleaning procedures.

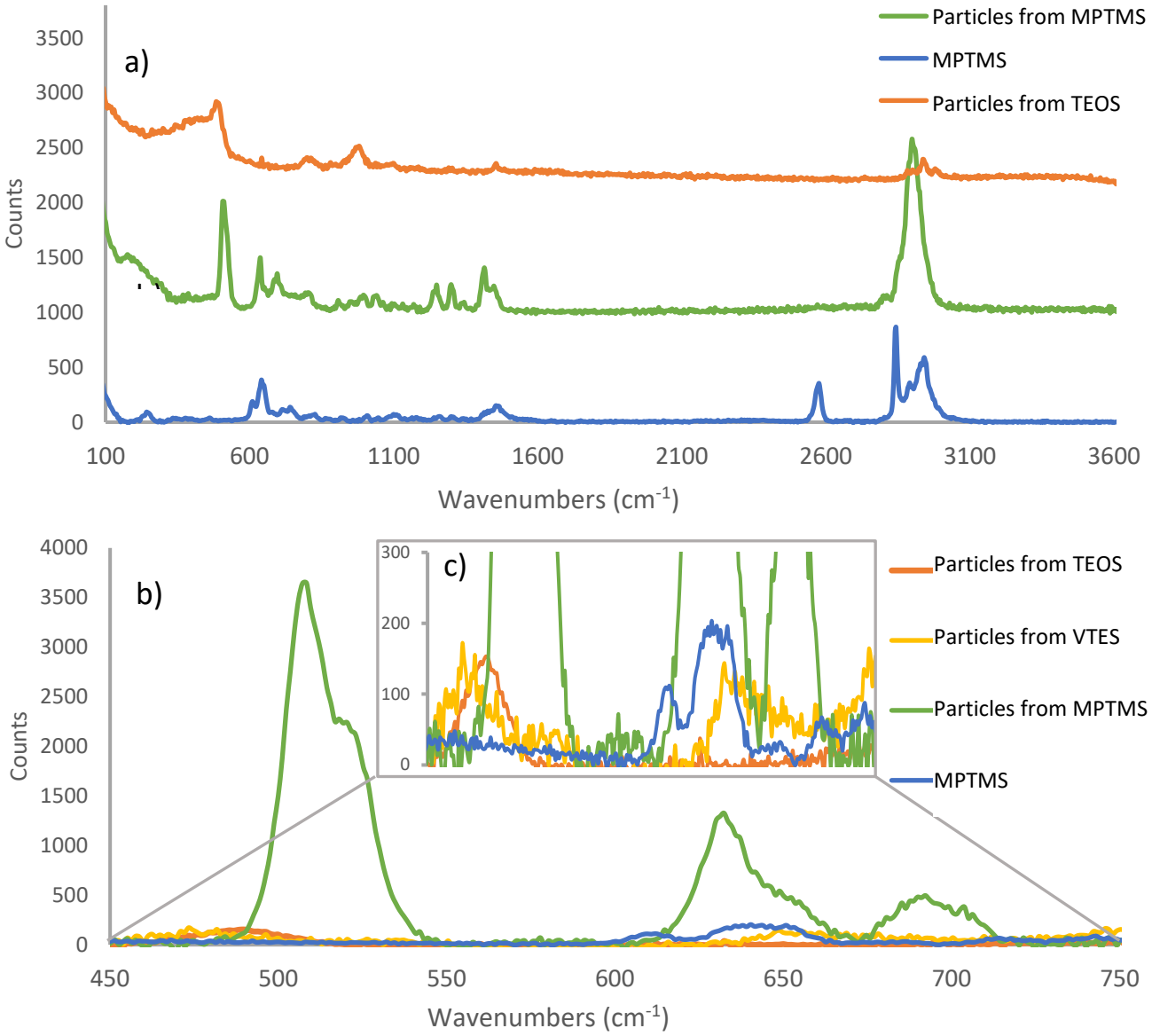

Figure 12: Raman Microscope Spectra of MPTMS particles, particles made form TEOS, particles made from VTES and dried MPTMS (monomer). a) Low resolution full spectrum b) High resolution spectrum from 450-750 cm^{-1}

Ellman's reagent (DTNB) is a disulphide molecule with UV-Vis absorption below 410 nm in solution. When it reacts with a thiol, it undergoes a thiol-disulphide exchange where the DTNB breaks in half, with one side remaining attached to the original thiol and the other half remaining as a TNB anion in solution.[274-276] This TNB anion has a bright yellow colour and a UV-Vis peak at approximately 420 nm, as shown in Figure 14.

When DTNB was reacted with MPTMS particles, the particles were centrifuged and the supernatant was collected and analysed via UV-Vis (Figure 14). This UV-Vis spectrum has the same absorbance profile as the unreacted DTNB, indicating either that no thiols are at the surface of the particles, or that the amounts are so low as to be below the limits of detection.

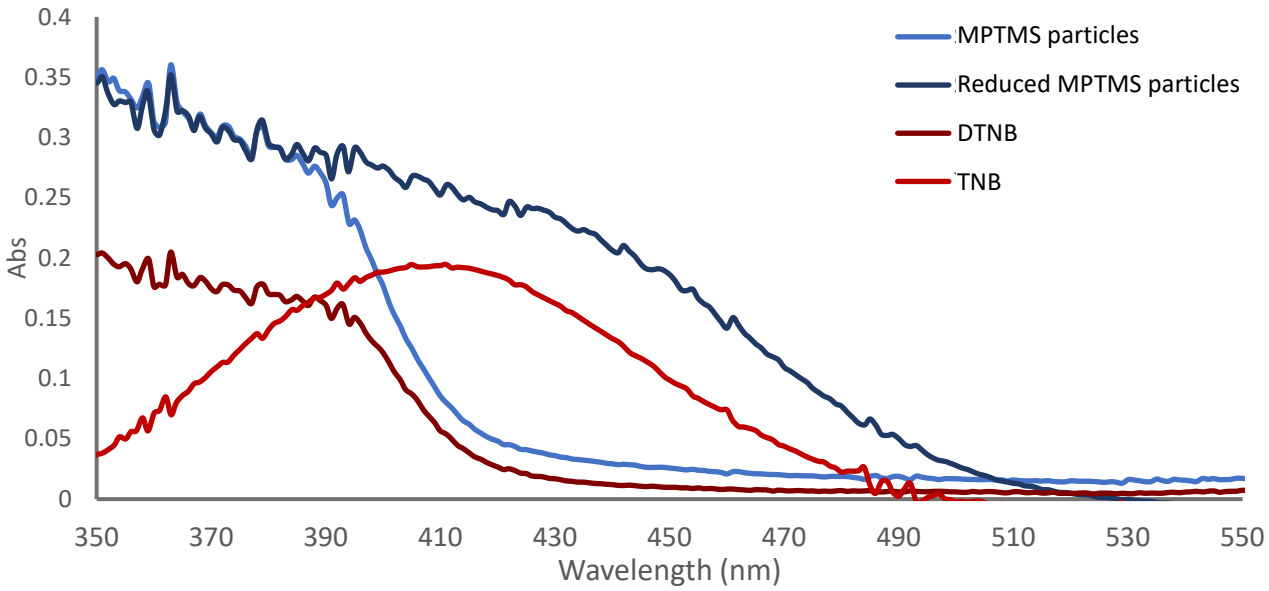

Figure 14: UV-Vis spectra of Ellman's reagents reactions with MPTMS particles (light blue) and reduced MPTMS particles (dark blue). Spectra of unreacted Ellman's reagent (dark red) and reacted Ellman's reagent (TNB, red) are provided for reference.

To test if the disulphide groups at the surface can be reduced back into thiols, the same batch of MPTMS particles were reacted with tributylphosphine and water in ethanol under a nitrogen atmosphere as shown in Figure 13 below. This reaction method has been used for the reduction of disulphides to thiols in small molecule chemistry[284,285] but has not, to the best of my knowledge, been applied to particle surfaces. These reduced particles were then cleaned and reacted with DTNB reagent, the subsequent UV-Vis analysis of the supernatant is shown in Figure 14. This sample had a bright yellow colour and the UV-Vis spectrum is a combination of the excess unreacted DTNB and reacted TNB, implying that thiols were present at the particle surface after reduction with tributylphosphine. The density of thiol groups at the surface was calculated to be 0.48 thiols/nm^2 using the molecular absorptivity of TNB, which is well below the theoretical maximum of 5.[194,195] This could be due to steric hindrance of the bulky tributylphosphine molecule as it approaches the surface for the reduction reaction, or the bulky TNB that remains attached to the surface, preventing reactions with further DTNB molecules.

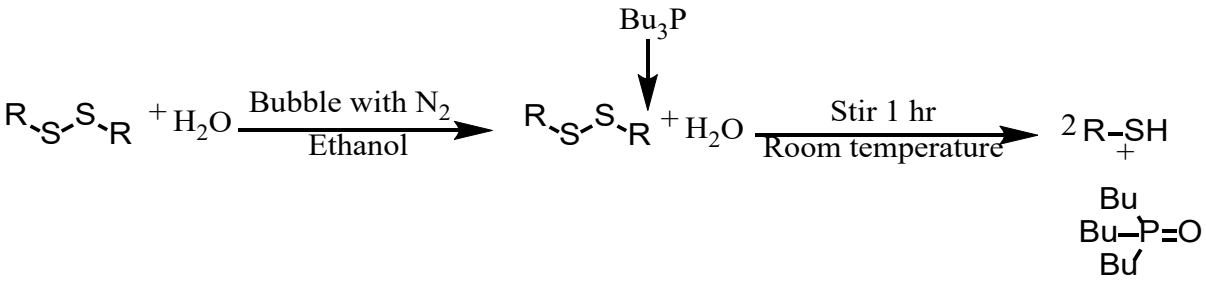

Figure 13: Reduction of disulphides to thiols using tributylphosphine as a reducing agent

The stability of the post-synthesis thiol-groups on the particle surface was monitored over two weeks by periodically drying a sample of the reduced particles and measuring the Raman spectrum of the

dried samples. The particles were also stored in three different solutions to test thiol stability in different conditions: distilled water, a pH 5 HCl solution, and a pH 9 ammonium hydroxide solution. The ratios of the resultant disulphide peaks to thiol peaks were calculated and are displayed in Figure 15 below. The water sample showed the most consistent disulphide to thiol Raman peak ratio over time, implying that this was the most stable suspension. However, the thiol groups appeared to remain relatively stable over the two-week period as there is no clear increasing or decreasing correlation between disulphide to thiol Raman peak ratio and time.

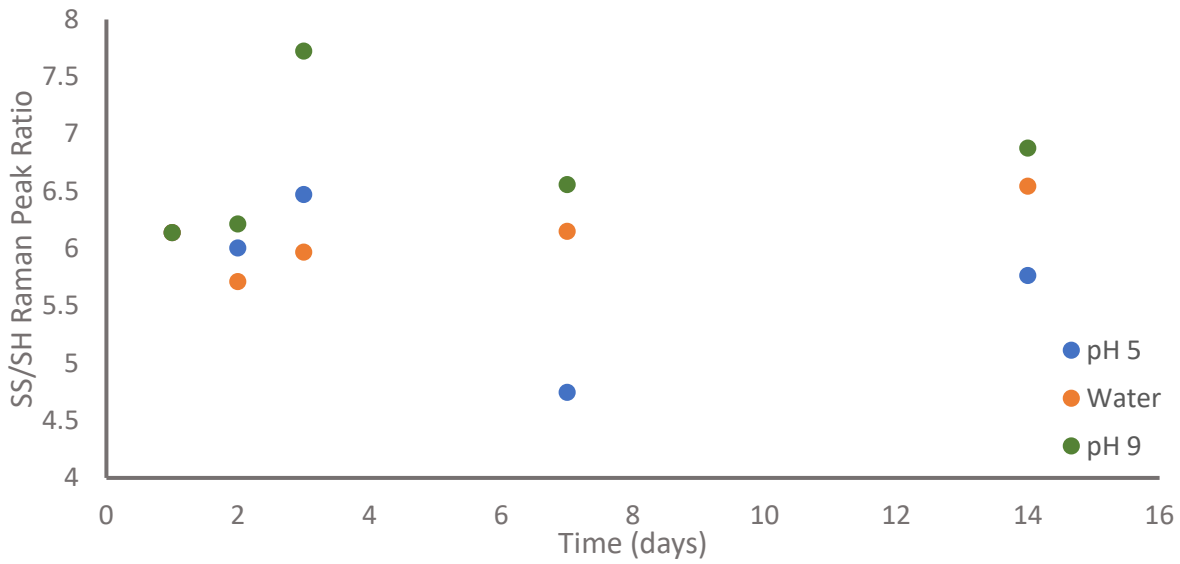

Figure 15: Post-reduction thiol stability over time in different pH conditions.

3.4.2 Effect of Cleaning Procedure

Four different cleaning methods were used on particles from the same batch in order to determine whether cleaning method can change the oxidation state of the sulphur of the final particles. These cleaning methods were:

(i) Using NaCl to destabilise the particle suspension before collection and rinsing via vacuum filtration (s).
(ii) Bubbling the particle suspension with air to evaporate the ammonia and cause destabilisation before collecting and rinsing via vacuum filtration (b).
(iii) Centrifuging from reaction mix (c).
(iv) Dried straight from the reaction mixture (d).

The Raman spectra for these samples is shown in Figure 16 below. All spectra were normalised to the SS peak at 504 cm^{-1}.

The ratio of the disulphide peak at 504 cm^{-1} and the thiol peak at 2560 cm^{-1} remains unchanged across all measured samples, indicating that the cleaning method has no effect on the sulphur oxidation. This

is especially significant as it implies that the sulphur state is decided during the synthesis reaction and cannot be easily changed post-synthesis, even for samples that are bubbled with air for over 24 hours. Another interesting observation; even though the same synthesis methods were used for samples measured in both Figure 12 and Figure 16, Figure 16 shows a thiol peak at 2560 cm^{-1} while Figure 12 does not. This indicates that very subtle variations in synthesis method could result in different levels of sulphur oxidation.

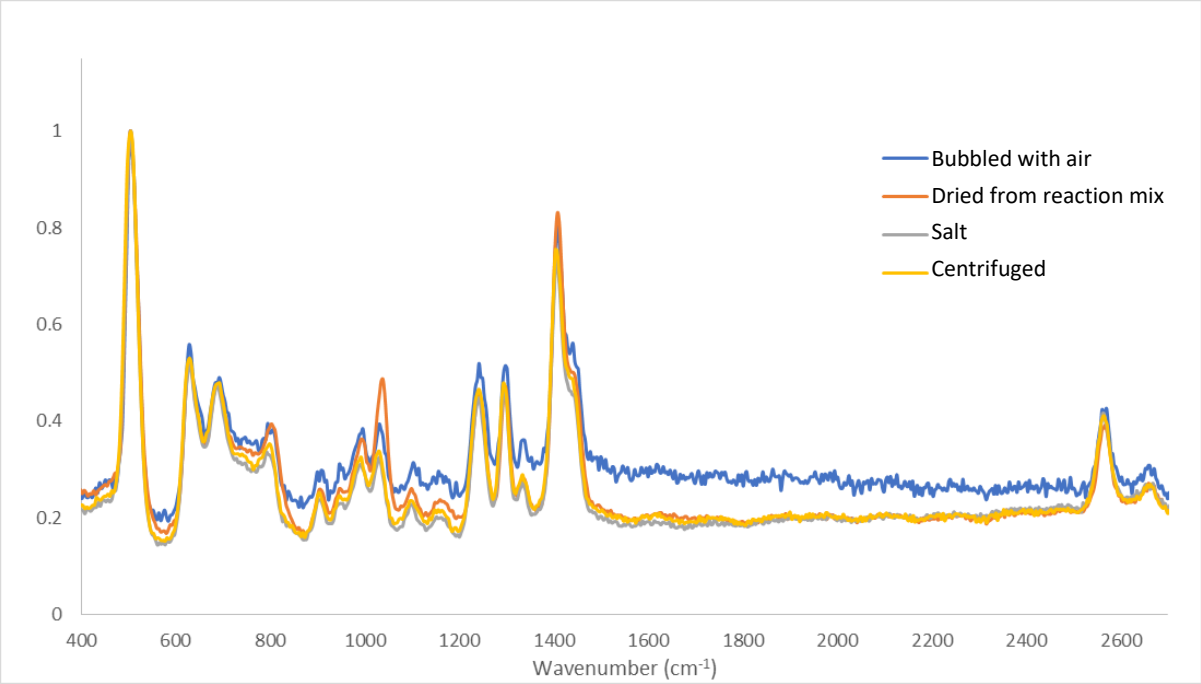

Figure 16: Raman spectra of MPTMS particles cleaned using different techniques. All spectra are normalised to the ss peak at 504 cm-1.

3.4.3 Reaction Method

As mentioned in the introduction, different synthesis methods appear to produce particles with differing sulphur chemistry. However, as these studies are conducted by independent research groups there is apparently no research into how to control the sulphur state in the final particles.

In order to systematically compare and determine how changing reaction conditions can affect the final particle chemistry, three different particle synthesis methods were utilised.

Methods A and B are very similar, with the only change being order of addition. Both methods are modified Stöber process and as such progress via nucleation-growth mechanism. In method A, the MPTMS was added neat to a stirring mixture of water, ethanol, and ammonia and left to stir slowly for 45 minutes before increasing the stirring speed for the rest of the reaction. Method B involved mixing the MPTMS with the ethanol prior to the addition to the stirring water/ammonia solution. Mixing the MPTMS with ethanol first negates the need for the initial period of slow stirring. The

differences in these two approaches was predominantly thought to effect MPTMS solubility and as such would have a small effect on the exact synthesis mechanism. Thus, it was previously assumed that the resultant particles would have the same chemical composition. Method C uses SDBS (an anionic surfactant) as a stabilising agent that remains complexed to the final particle surface. The use of a surfactant also switches the reaction mechanism from nucleation-growth to an emulsion.

Through comparison of the Raman spectra shown in Figure 17, it can be seen that the order of addition does appear to affect the final sulphur oxidation state of the particle.

Method C shows a large thiol peak with a relatively low disulphide peak, implying that the thiol groups present in MPTMS remain mostly untouched during the particle synthesis. In contrast both methods A and B show a much larger disulphide peak than thiol peak, with method A not having a thiol peak at all. This suggests that the nucleation-growth process is more likely to oxidise thiol groups to disulphides, and that a subtle change to reaction method (such as order of addition) can result in changes to the final sulphur composition of the particle. As this project is looking at attaching particles together and the SDBS can be very hard to remove properly from the particle surface, the remainder of this study will focus on methods A and B.

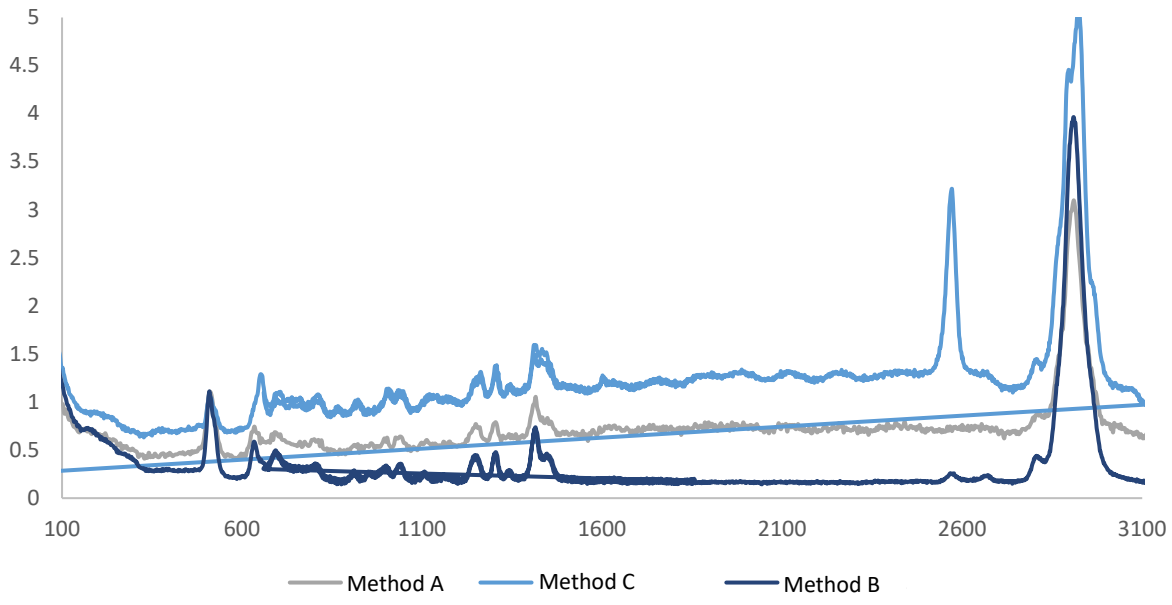

Figure 17: Raman spectra of particles made using methods A, B and C

3.4.4 Effect of Ammonia Concentration on Sulphur Oxidation State

In order to more thoroughly test the effect of reaction conditions on thiol oxidation, both methods A and B were repeated with varying ammonia concentration. The Raman spectra for these samples were

normalised to the disulphide peak at 505 cm^{-1} and are shown in Figure 18 below. By taking a ratio of the disulphide peak to the thiol peak at 2565 cm^{-1}, the relative extent of thiol oxidation could be monitored across these different reaction conditions.

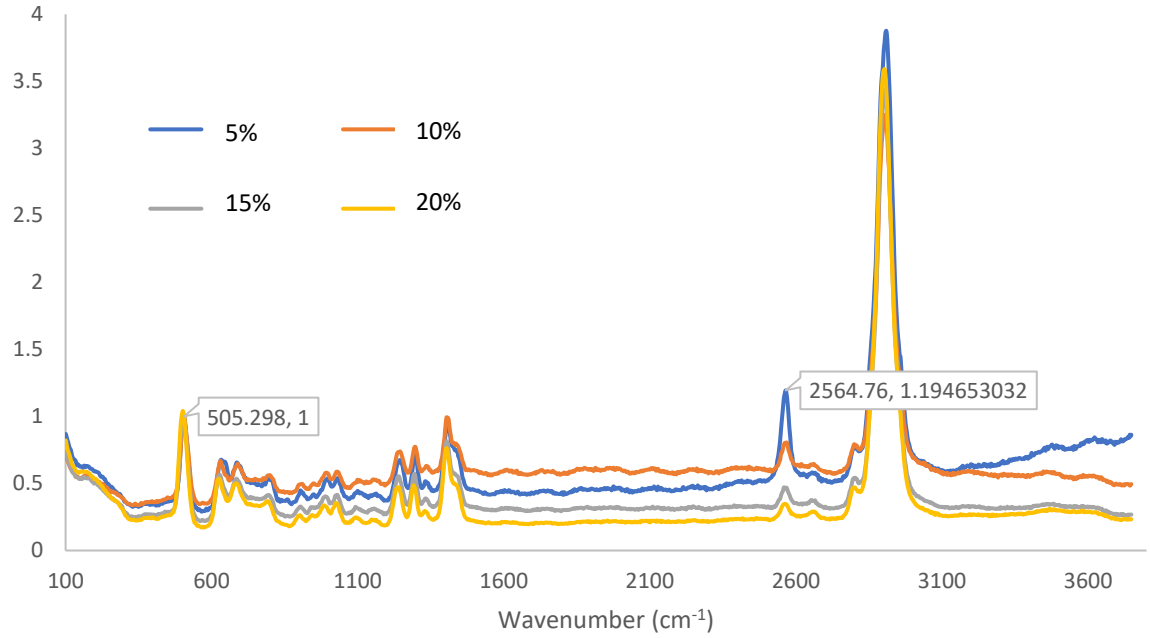

Figure 18: Raman spectra of MPTMS particles with varied ammonia concentration synthesised using method A

Figure 19 shows that as the concentration of ammonium hydroxide in the reaction mixture was increased, the ratio of disulphides to thiols in method A also increased in a linear fashion. These results indicate that ammonia has an active role in the oxidation of thiol groups to disulphides during particle synthesis. Method B initially follows the same trend as method A until the ammonia concentration was increased to 15 %v/v where the ratio of disulphides to thiols plateaus into a more logarithmic trend. Thus, mixing MPTMS with ethanol prior to addition to the reaction mix appears to somewhat inhibit the oxidation of thiols to disulphides. However, it is not clear why this phenomenon only effects reactions with higher ammonia concentration.

As Raman is not a surface specific technique, the presence of disulphide groups at the surface of the particles is not inherently known. However, this rate of disulphide increase is much larger than the change in the volume to surface area ratio (shown in the Appendix), which implies that the increase in disulphides is not due to an equivalent increase in the volume. This further implies that the disulphide and thiol groups are not restricted to the inside and surface of the particles respectively. If the surface was entirely thiols and the volume was entirely disulphides, the expectation is that the rate of change of these two trend lines would be equivalent. The samples were also tested with

Ellman's reagent assays, however all UV-Vis results were below the limits of detection. As such, this method could not be used to confirm this surface or volume hypothesis.

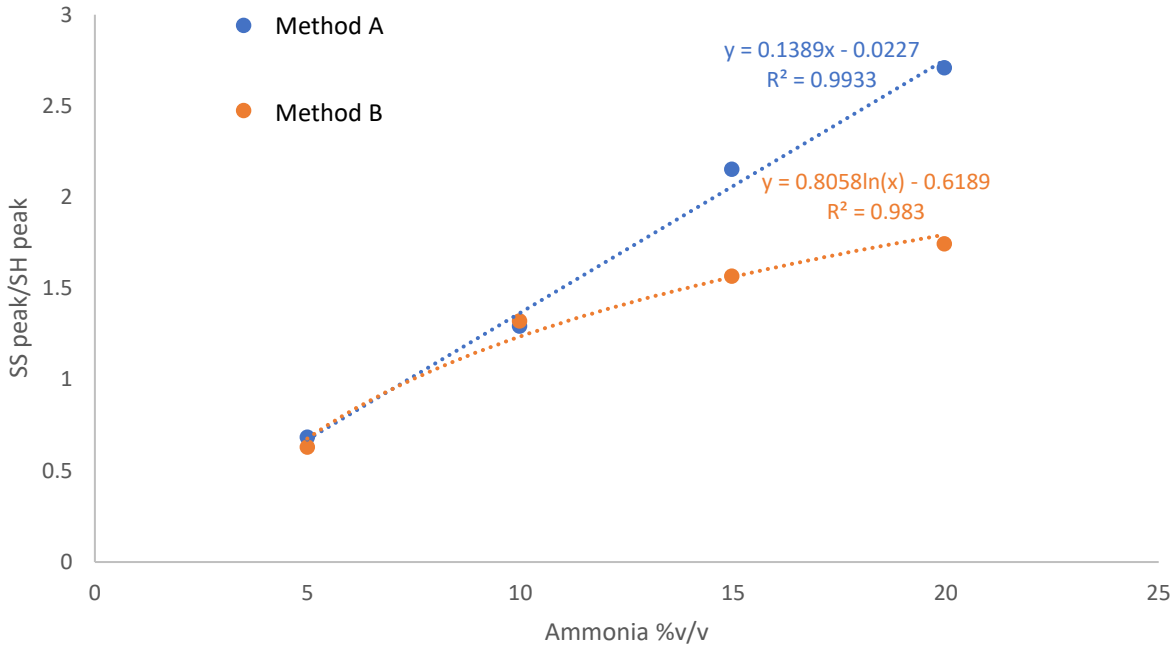

Figure 19: Dependence of disulphide to thiol Raman peak ratio on ammonia concentration

3.4.5 Effect of Ethanol Concentration on Sulphur Oxidation State

The same test was then done with ethanol rather than ammonia and the resultant disulphide/thiol peak ratios are shown in Figure 20. When the concentration of ethanol was increased, the disulphide to thiol ratio decreased for both method A and B at approximately the same rate, although the absolute values of method A were larger than method B. This implies both that ethanol seems to inhibit the formation of the disulphides and that mixing the MPTMS with ethanol first further prevents oxidation.

Again, the change in the disulphide to thiol ratios is not on the same scale as the change in size (Appendix), implying that the decreasing thiol concentration is not a direct correlation with the decreasing surface area to volume ratio. This again implies that the surface is not entirely thiols while the bulk is disulphides. All Ellman's reagent tests for these samples were below the limits of detection and as such could not be used to confirm this hypothesis.

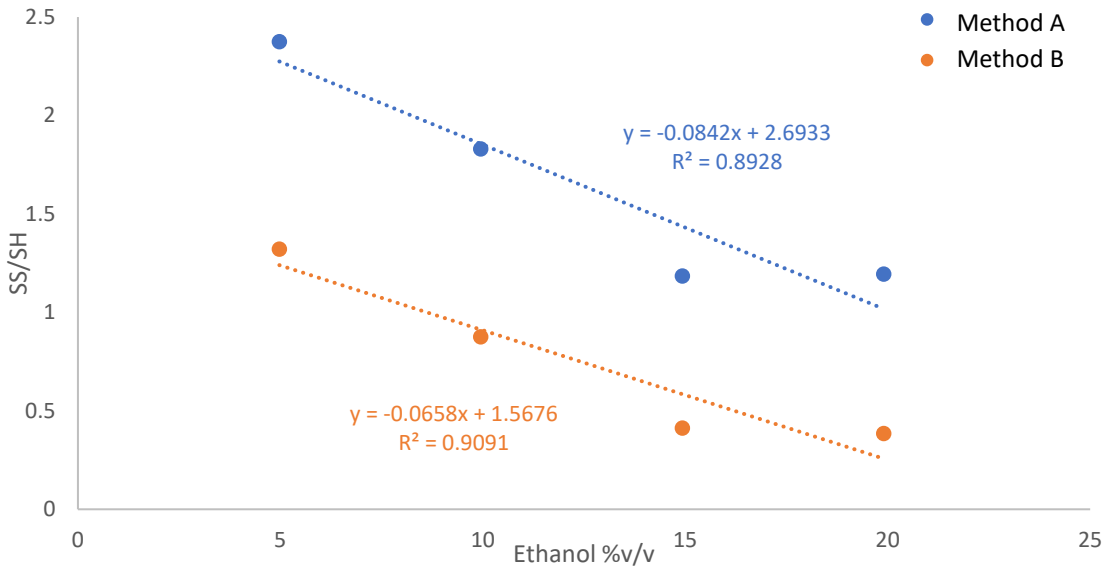

Figure 20: Dependence of disulphide to thiol Raman peak ratio on Ethanol concentration (Batch 1). Method A is shown in blue while Method B is shown in orange.

3.4.6 Nitrogen atmosphere

As the conversion of thiol to disulphide groups is an oxidation reaction, the role of atmospheric oxygen as the oxidising agent was investigated. Method A was repeated under a nitrogen atmosphere and the subsequent disulphide to thiol Raman peak ratio was investigated. This was achieved by bubbling the water/ethanol mix with N_2 before adding the ammonia solution and MPTMS in that order. The ammonia solution could not be bubbled in the same way, as the ammonia would evaporate. Consequently, not all atmospheric oxygen could be removed from the reaction mixture. This sample was found to have significantly less formation of disulphide groups than the equivalent made-in-air sample. This implies that atmospheric oxygen does act as the oxidising agent. A comparison of the disulphide to thiol Raman peak ratios for each of the different synthesis methods (method A, method B, method C, method A reduced, and method A in N_2) is shown in Figure 21 below.

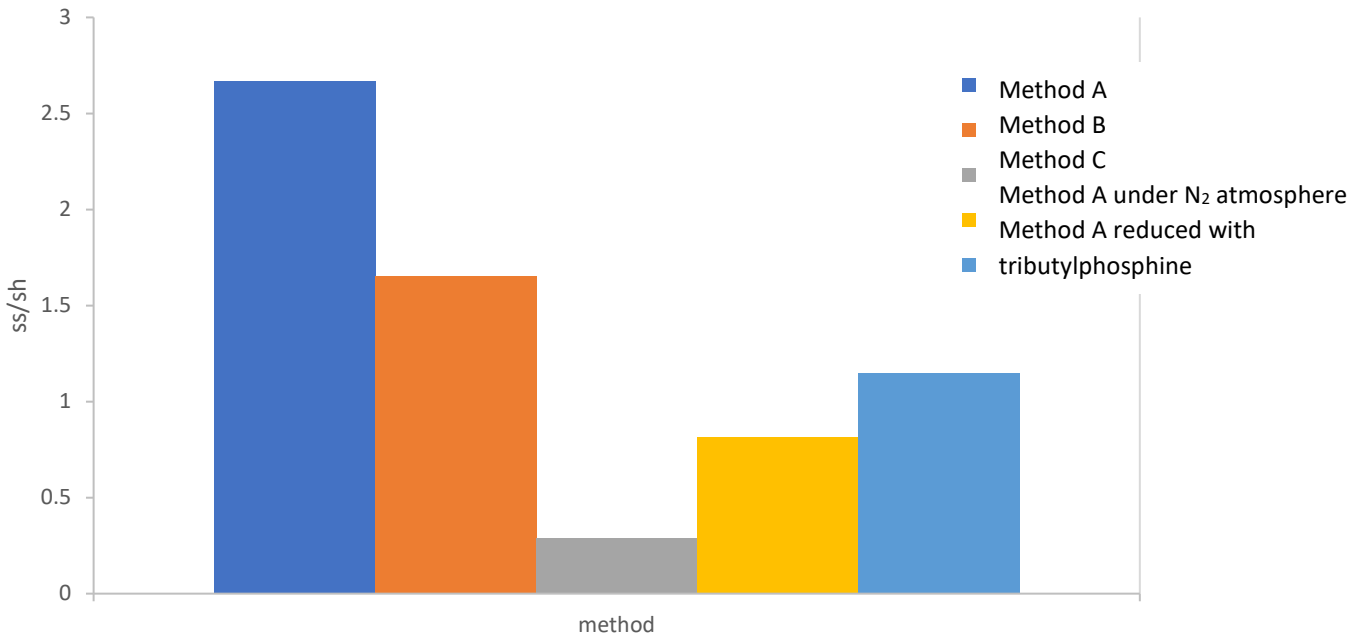

Figure 21: Summary of Raman results from different reaction methods. Dark blue is method A, orange is method B, grey is method C, yellow is method A under a N_2 atmosphere, and light blue is method A after reduction with tributyl phosphine.

3.4.7 Mechanism of Disulphide Formation

In the previous sections, it was found that ammonia and oxygen have a positive effect on the formation of disulphide groups while ethanol has a negative effect, and that atmospheric oxygen appears to be the oxidising agent. Using this information, a reaction mechanism was found to explain the conversion of thiols to disulphides under these conditions as shown in Figure 22 below.[305,306] In this mechanism a base (in this case ammonia) deprotonates the thiol to form a thiolate anion, which then reacts with oxygen (which is a di-radical) to form an oxyanion and a sulphur radical species. When two of these sulphur radicals combine, they form the disulphide in a combination reaction. As the sulphur groups in this case are held in close proximity by the by the forming silica network (particularly at the particle surface) the probability of sulphur radical recombination events is greatly increased, which would explain why there appears to be far more disulphides than thiols in most of the reaction methods tested. In method C, the particle synthesis is micellar, with SDBS acting as a surfactant. This phase separation of the MPTMS and the aqueous ammonia solution would drastically reduce the

formation of thiolate anions, resulting in the very low rates of oxidation observed in the previous sections.

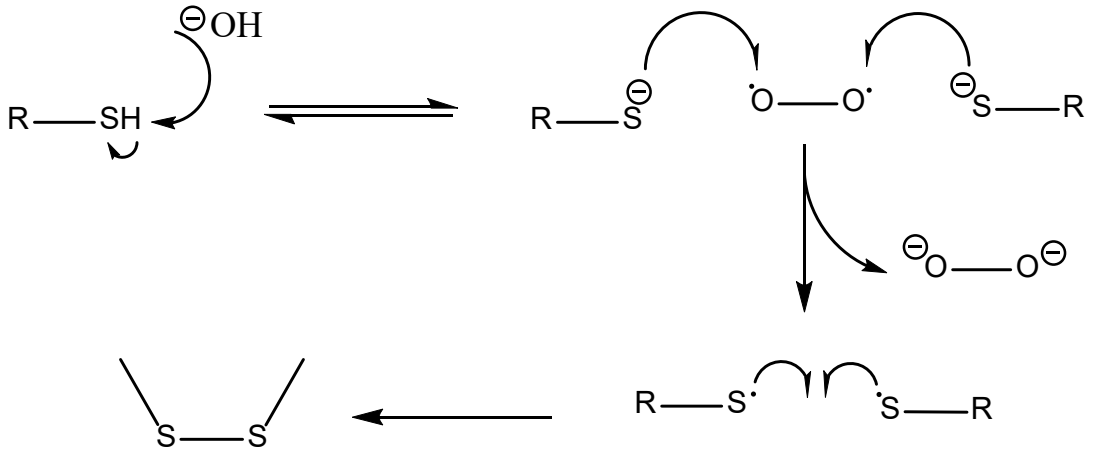

Figure 22: Thiol Oxidation Mechanism

In this mechanism, increasing the concentration of ammonia would in turn increase the concentration of thiolate anions, resulting in more oxidation. This explains the directly proportional relationship shown in Figure 19. Similarly, increasing the amount of oxygen results in increased sulphur radical formation and thus increased thiol oxidation.

Ethanol is used in the synthesis of MPTMS particles to control the rate of hydrolysis, with increasing ethanol concentration slowing down the reaction by shifting the equilibrium to the left. This slower reaction rate prevents uncontrolled reactions, resulting in the final uniform spherical shape of the particles. However, the role of ethanol in the oxidation of thiols remains unclear; it does not prevent oxygen dissolution (oxygen is more soluble in ethanol than water[307]), so there would be no inhibition of the oxidising agent. It could be that the ammonia is slightly less soluble in the ethanol than the water while the MPTMS is more soluble, resulting in slightly decreased formation of thiolate anions.

3.5 Conclusion

A systematic study into the oxidation state of sulphur in MPTMS silica particles was undertaken. Through Raman microscopy and Ellman's reagent assays it was found that silica particles grown from MPTMS via a modified Stöber process have a greater proportion of disulphide groups than thiols. In contrast, silica particles grown from MPTMS via a surfactant method were found to have more thiol groups than disulphides. Once formed, disulphide groups at the surface of the particles could be reduced to thiols via a reaction with tributylphosphine.

The ratio of disulphides to thiols was found to increase with increasing ammonia concentration and decrease with increasing ethanol concentration during the particle synthesis reaction. Atmospheric

oxygen was found to be the oxidising agent for the conversion of thiol groups to disulphides during particle synthesis. These factors were used to assign a mechanism to the formation of disulphides and can be used to tune the sulphur state of the final particles.

Whether or not the presence of thiols or disulphides at the particle surface is important for further reactions is investigated more in the next two chapters of this thesis.

Chapter 4: Thiol-Epoxy silica particle attachment

4.1 Summary

This chapter presents a novel synthesis method for raspberry particles from MPTMS and GPTMS silica particles as the attached and core particles respectively. This reaction utilises base-catalysed click chemistry between the thiol- and disulphide-groups of the MPTMS particles and the epoxy groups of the GPTMS particles. This reaction allows for a combinatorial approach to control the ratio of the small particles to the larger ones, with high-density attachment (≥90%) seen for all MPTMS particles greater than 90 nm in size.

The thiol oxidation state of the MPTMS particles was found to have negligible effects on the attachment density of the final particles. Zeta potential measurements showed that high pH can be used to create thiolate anions on the surface of MPTMS particles with both thiol and disulphide surface functionality.

These particles were then used in the production of superhydrophobic coatings with water contact angles of >150^{o} and sliding angles of <10^{o} in conjunction with PDMS. The effect of particle:polymer and small:large particle size ratios on the wettability of the final coatings was investigated.

4.2 Introduction

The production of so-called raspberry particles has gained increasing interest since approximately 2005, when it was shown that they could be incorporated into films that mimic the superhydrophobic and self-cleaning properties of the lotus leaf.[13] In order to truly mimic the surface of the lotus leaf, and a variety of other natural surfaces, the produced surface must have multiple scales of roughness.[178,179] Prior to the use of raspberry particles, methods such as lithography, soft lithography, electrochemical deposition, electrospinning, and chemical deposition were used to produce these roughened surfaces,[25,38,174] however many of these methods have several processing steps or instrumentation that require strict experimental conditions or expensive materials.[25,38]

A common alternative method for the production of hierarchal roughened surfaces is the synthesis of so-called raspberry particles.[5,8-13,15,17,19,20,24-27,74-79,148,154,155,161,162,173,308-312] In essence, raspberry particles are composed of a large core particle that has been covered with smaller shell particles, which allows these particles to mimic the dual-scale roughness of the lotus leaf. There have been many methods developed for the synthesis of raspberry particles, however these particles are usually either difficult to synthesise or give poor control over the size ratios of the dual-scale roughness.[5,79,148,154,155,161,162,173,308,309] As scale has found to play a large role in the wettability of single-scale roughened surfaces,[118,178] it is reasonable to assume that scale and size ratio of the dual-scale

roughened surfaces will be equally important. However, there is few studies into the practical impact that size ratio has on the wettability of the surface.[15,25]

In most of the above examples, ether the core or shell (or both) particles are silica. In all of these cases the silica particles are grown from tetraethylorthosilicate (TEOS) using the Stöber method which gives monodispersed particles with good control over the produced size at both the micro- and nanoscale.[121,216,217,220,221,227,228,148,154,161,216,217,221,222] However, this method produces silica spheres with hydroxyl functional groups instead of the amines, epoxies, and other functional groups that are required for many of the attachment reactions in literature. This leads to an additional functionalization step, which can be time consuming and requires extra materials.[80-82,84,85,121,150,158,164,171,229-231]

In order to avoid this post-growth functionalisation step, there has been development of modified Stöber processes that use silane precursors that already have the desired functional group in their structure.[194-196,198,231,232] Some examples of silica particle functionalisation that have been achieved in this way are thiols, epoxies, and alkenes.[194-198,231,232]

In this Chapter, we present a facile, combinatorial approach to the synthesis of raspberry particles using large epoxy-terminated silica particles as the core and smaller thiol-terminated silica particles as the shell. These silica particles were grown using a modified Stöber process that allows for the production of the desired functional groups without the need for post-synthesis functionalization. Additionally, this method allows for good control over the size ratio of the hierarchal roughness of the produced raspberry particles. These raspberry particles were then incorporated into superhydrophobic coatings with PDMS where the role of both the particle:polymer and raspberry size ratios on the final coating wettability was explored.

4.3 Methods

The methods relevant to this chapter are described in the following sections:

2.2.1.1 Method A, 2.2.3 Synthesis of Particles with Different Diameters, 2.2.6.1 Centrifuge, 2.3 Reduction of disulphides at MPTMS Particle Surface, 2.5 Effect of pH on MPTMS Particle Surface Charge, 2.6 GPTMS Particle Synthesis, 2.8 MPTMS-GPTMS Raspberry Particle Attachment, 2.9 Raspberry Particle Coatings, 2.14.1 Sputter Coating, 2.14.2 SEM Imaging, 2.14.3 Characterisation of Particle-on-Particle Attachment Density, 2.14.7 Zeta Potential, 2.14.9 Water Contact Angle Measurement, and 2.14.10 Sliding Angle Measurement.

4.4 Results/Discussion

4.4.1 Attachment Reaction Thiol-epoxy click reactions are used extensively in materials science, particularly in the area of polymer cross-linking and modification.[255,256,260-262] Thiol and epoxy functional groups are able to react together in a typical epoxy ring-opening reaction to form a β-(hydroxyl)thioether[256,261,264,265] as illustrated in Figure 23. These reactions are typically catalysed with bases, which generate a thiolate anion, which is able to attack the epoxy ring in a nucleophilic reaction, forming an oxyanion.[256,261,264,265] This oxyanion is then able to deprotonate a thiol group, producing a secondary hydroxyl group and a thiolate anion, which is in turn able to propagate the reaction.[256,261,264,265] Bases have also been used to break sulphur-sulphur bonds,[313,314] which should allow them to form thiolate anions and react in much the same way as thiol groups. As the MPTMS particles were found to have predominantly disulphide groups at their surfaces this is an important consideration in the development of the attachment reaction.

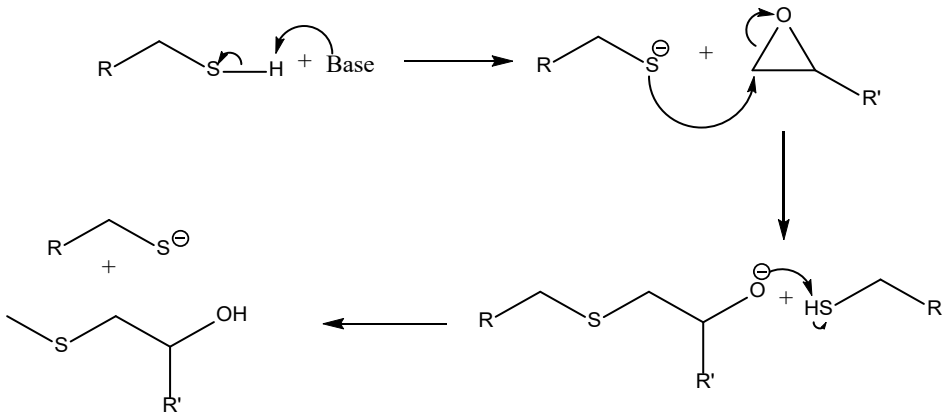

Figure 23: Mechanism of the base catalysed thiol-epoxy reaction

4.4.2 Zeta Potential

As this is a nucleophilic attack reaction, maximum reaction efficiency occurs when the sulphur groups have been completely reacted to form thiolate anions. In order to determine at which pH this deprotonation or disulphide bond breaking event occurs, a series of zeta potential measurements were taken of MPTMS particles with disulphide groups at the surface in suspensions with varying pH and are shown in Figure 24. At low pH, the particle suspension was immediately rendered unstable, causing the particles to aggregate and crash out of solution. As these particles could not remain in suspension, an accurate zeta potential could not be measured and 0 mV is used as a placeholder. Between pH 4-9, there is a plateau region in which the particle suspension is relatively stable with an average zeta potential of *ca.* -25 mV. In this range, the disulphide groups would be undergoing a constant equilibrium between the neutral and thiolate states, resulting in a partially negatively charged surface. The combination of the electrostatic repulsion between these thiolate anions and

the attractive forces between the polar particle surface groups and the surrounding aqueous medium results in a stable particle suspension. The sharp decrease in zeta potential at pH≥10 indicates that the magnitude of the surface charge is increasing and the equilibrium of the disulphide bond breaking reaction is shifted towards the thiolate species. This increase in negative surface charge would result in increased stability of the suspension due to the increase in electrostatic repulsion between the charged surfaces, preventing aggregation. However, at pH 13 and higher, the highly basic conditions catalyse the hydrolysis of the silanol groups, causing the particles to start to dissolve after a few hours. Thus, the disulphide terminated silica particles are likely only able to react effectively with the epoxide-terminated silica particles between pH 10-13. A comparison of MPTMS (disulphide) particles and reduced MPTMS (thiol) particles was then undertaken at pH 7-13. As can be seen in Figure 25 below. The thiol particles were found to have a similar trend to the disulphide particles with a deprotonation event occurring at pH 10, resulting in a more negatively charged surface due to more thiolate anion presence. The similarities between the zeta potential trends of both the thiol and disulphide trends indicates that despite the different sulphur oxidation states both particles should be available for attachment reactions with the epoxy particles. The thiol particles have a slightly higher surface charge magnitude than the disulphides, which would indicate that they should give rise to a higher attachment density on the core GPTMS particles, as they appear to have more thiolate anions at their surface.

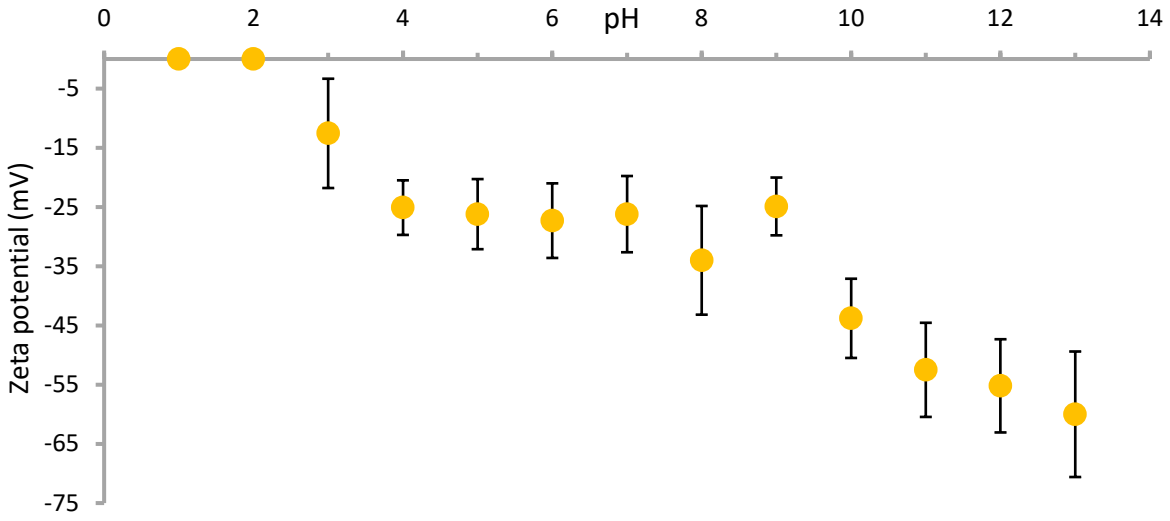

Figure 24: Deprotonation of thiol-terminated silica particles

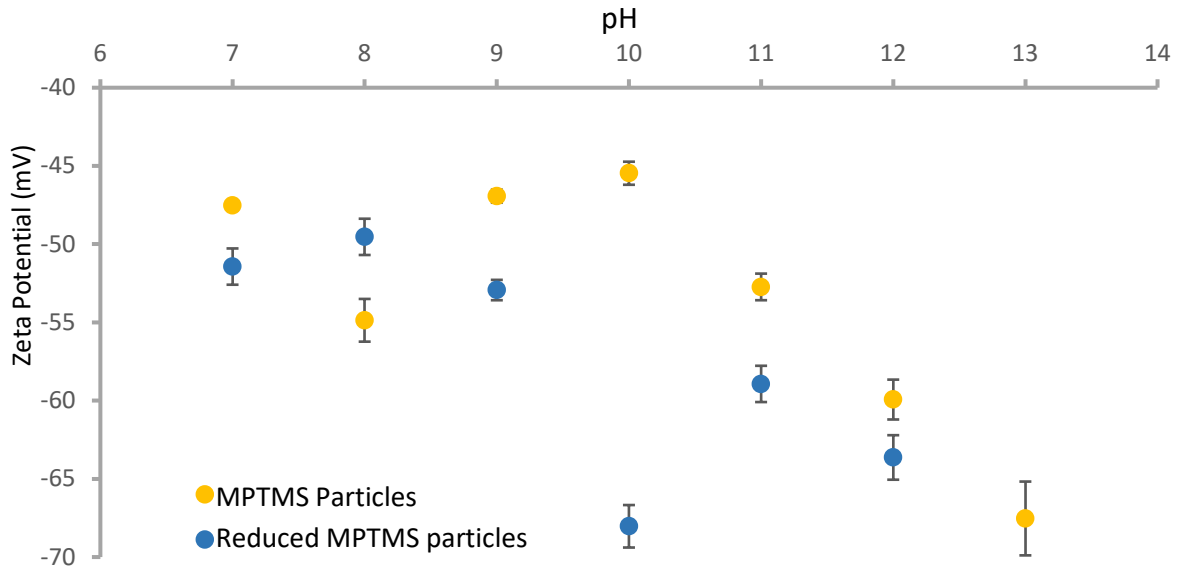

Figure 25: Zeta potential comparisons of disulphide particles in yellow and thiol particles blue

The raspberry particles were synthesised by combining the 2 µm GPTMS particles (to act as the core) and 143 nm MPTMS particles (to act as the shell particles) in acetonitrile as shown in Figure 26 below. Ammonia solution (25%) was then added in order to create a pH of 10-11 for the reaction to take place. The reaction mixture was left stirring for 2 days before the unattached MPTMS particles were removed *via* centrifugation and the raspberry particles were imaged using SEM. The attachment density was characterised as the number of MPTMS silica particles per unit area of the core GPTMS particle. The attachment density was also compared to a calculated "theoretical maximum" attachment density (example calculation shown in the Appendix) based on the sizes of the MPTMS and GPTMS silica particles.

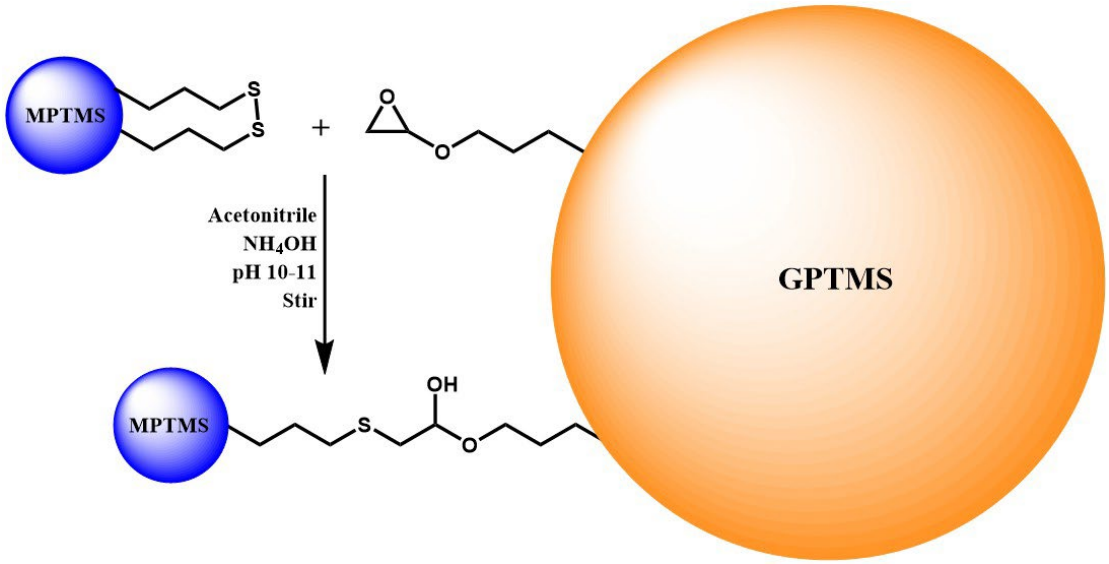

Figure 26: Raspberry particle attachment reaction schematic.

4.4.3 Particle Concentration

While optimising the attachment reaction, varying amounts of acetonitrile were added to the reaction mixture in order to test the effect of particle concentration on the attachment density (actual reaction conditions are shown in Table 7, as are the particle attachment densities measured as both particles/μm^2 and as a percentage of the theoretical maximum). While the overall trend (Figure 27) shows the expected increase in attachment density (displayed as a percentage of the theoretical maximum) as the particle concentration increases, at very low particle concentrations (<1%) the attachment density was found to be relatively high at 72%. This is highly unusual, as at low particle concentrations collisions between the MPTMS and GPTMS silica particles become less likely, which should in turn result in a lower attachment density. Above particle concentrations of approximately 10%w/w, there is no significant change in attachment density with increasing particle concentration, implying that a maximum has already been reached.

Table 7: Attachment densities of produced raspberry particles from different particle concentrations.

Particle concentration (%w/w)	**Attachment density (particles/μm^2)**	**Attachment relative to theoretical maximum (%)**
0.58	60.5 ± 11	72
2.87	28.9 ± 5.7	34
7.07	34.1 ± 9.1	41
10.09	85.3 ± 15	102
13.34	55.6 ± 10	95

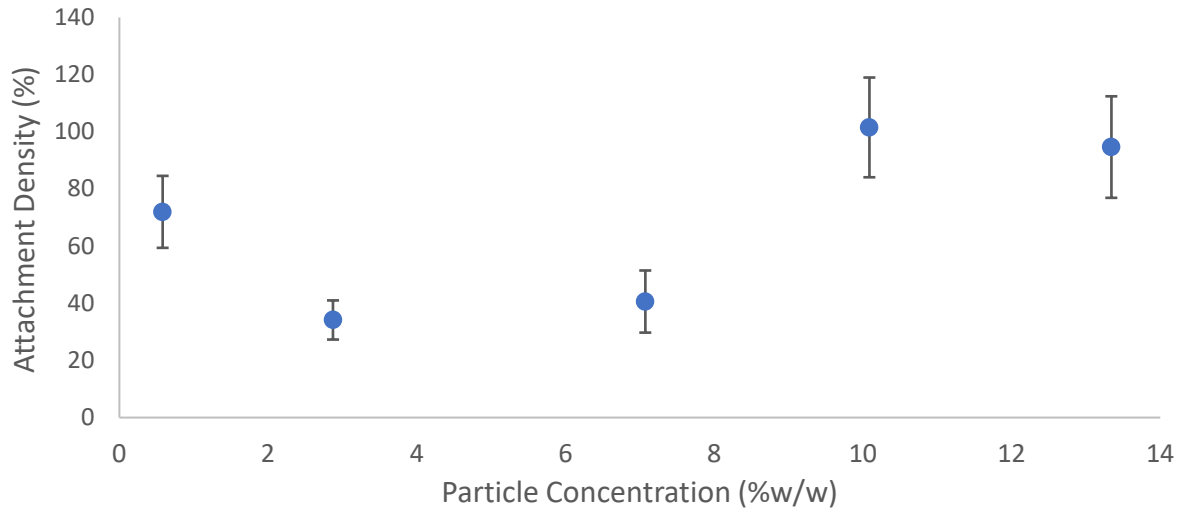

Figure 27: Effect of particle concentration on the resultant attachment relative to the theoretical maximum.

From these results, the maximum attachment density for the 143 nm MPTMS particles occurred at a pH of 10 and a particle concentration of 10.09 %w/w. Using these conditions, attachment reactions were undertaken with MPTMS particles with average diameters of 38 nm, 98 nm, 143 nm, 220 nm, and 235 nm. The resultant raspberry particles from these reactions are shown in Figure 28 below. The attachment densities of these reactions were found to be 45%, 121%, 95%, 99% and 89% of their theoretical maximums respectively. With the exception of the 38 nm particles, these attachment densities are consistently ≥90%. The calculated theoretical maximum is not a perfect depiction of the

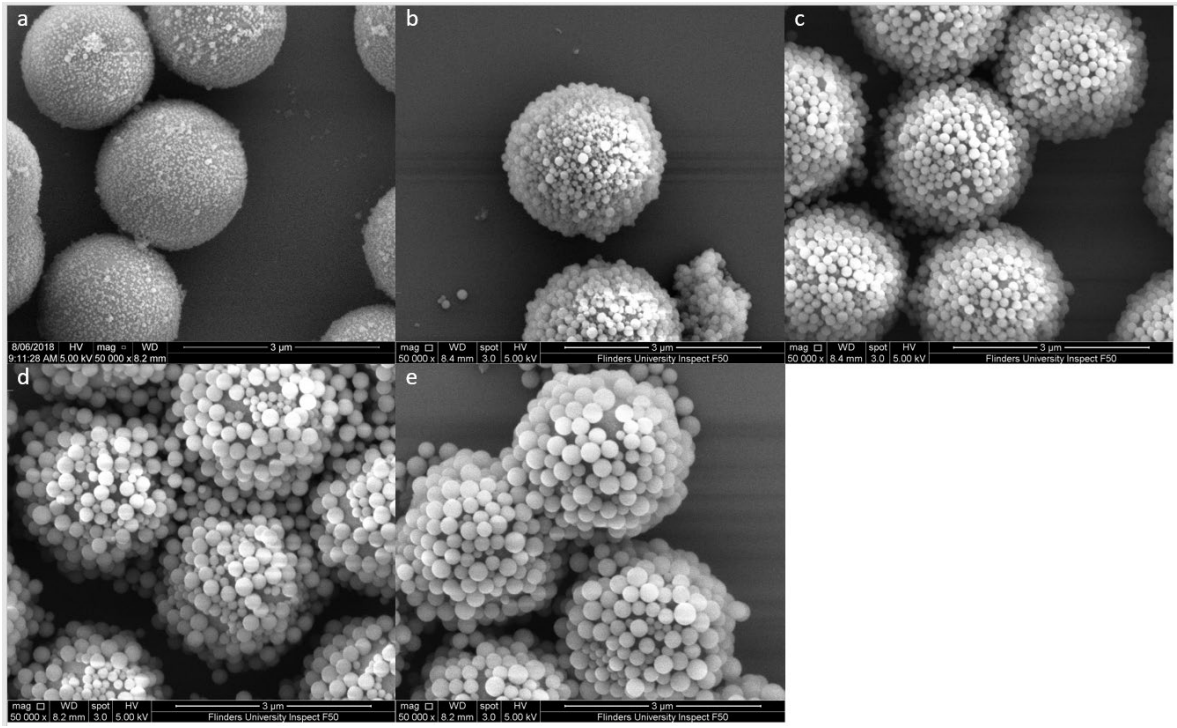

Figure 28: Resultant raspberry particles from the thiol-epoxy attachment reaction between SiP-Ep (1.7 µm) and SiNP-SH of a) 38 nm, attachment density of 45%; b) 98 nm, attachment density of 121%; c) 143 nm, attachment density of 95%; d) 220 nm, attachment density

actual conditions, namely because the calculation assumes that the particles are all perfectly monodispersed. This assumption is especially evident in the case of the 98 nm attachment reaction where the resultant attachment density was found to be >100% of the theoretical maximum. Despite this, the visibly high coverage of the GPTMS particles confirms that the final raspberry particles do have high density attachment. The lower attachment density of the smaller 38 nm particles could be a result of decreased Van der Waals interactions between particles as the particle size decreases[171] (in much the same way that molecules experience less Van der Waals attraction as they become smaller). These decreased attractive forces are likely to be unable to overcome the electrostatic repulsion between the negatively charged MPTMS particle surfaces to attach at higher densities.[171]

4.4.4 Reduced vs Non-reduced particles

In order to investigate the effect of thiols vs disulphides on the attachment of MPTMS particles to GPTMS particles, separate attachment reactions were undertaken with reduced thiol-MPTMS particles and regular disulphide-MPTMS particles. The resultant raspberry particles are shown in Figure 29 below, and the attachment densities were calculated as 78.1 ± 19.9 % and 87.5 ± 13.3% of the theoretical maximum for the thiol-MPTMS and disulphide-MPTMS particles respectively. From this, it can be seen that the thiol functional group has slightly lower attachment density than the equivalent disulphide particles, but this is well within the standard deviation and as such is not statistically significant. This is consistent with the zeta potential results (Figure 25), which showed that the thiol particles had less overall surface charge at the same pH than the disulphide particles. This implies that there is somewhat less thiolate anions that can undertake the epoxy-click attachment reaction. However, there does not need to be many attachment reactions per MPTMS particles in order for them to attach which could explain the lack of statistical significance.

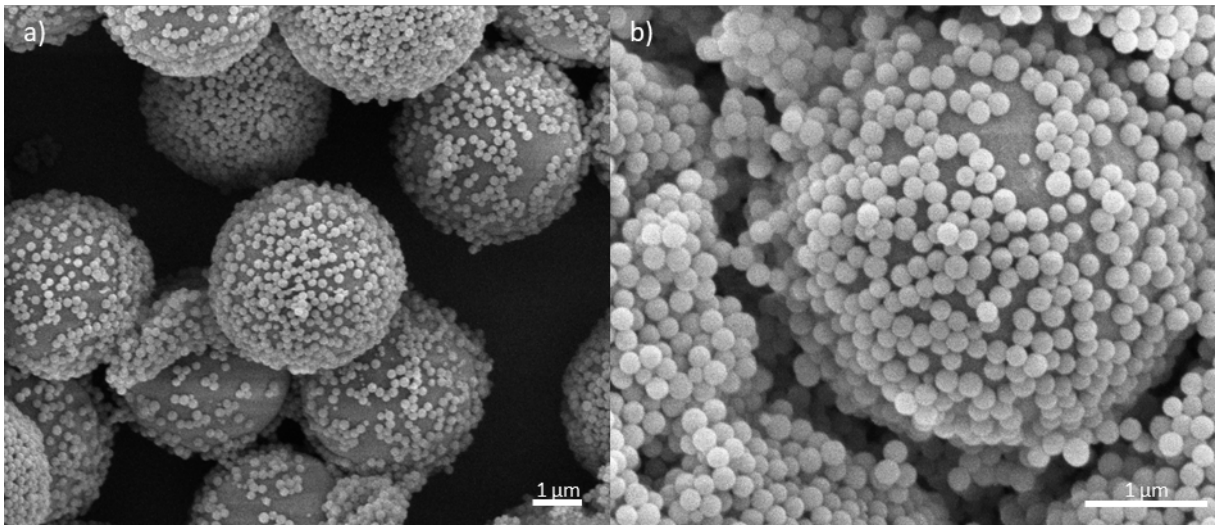

Figure 29: Attachment of a) thiol and b) disulphide particles to epoxy particles.

4.4.5 Incorporation of Raspberry Particles into Hydrophobic Coatings

When incorporating raspberry particles into a coating, there are three scales of roughness that must be considered. The first scale is the size of the smaller attached shell particles, the second scale is the size of the core particles and the third scale is the greater arrangement of the particles on the coated surface. These three scales may be very important to the hydrophobicity of the final coating and can be controlled in several ways. The two controls explored here are the ratio of particles to polymer and the ratio of the small particle size to the large particle size.

4.4.6 Effect of Particle:Polymer Ratio on Coating Wettability

When the ratio of raspberry particles to PDMS in coating solutions is altered, the morphology is also changed. In order to test how this would affect the wettability of the final raspberry particle coated surfaces, coatings were made with particle:polymer ratios of 0:1, 0.5:1, 1:1, 1.5:1, 2.4:1, and 3:1. The subsequent water contact angles were measured as 89.5° ± 5.1°, 99.6° ± 9.6°, 115.6° ± 7.4°, 128.9° ± 10.2°, 134.5° ± 4.7°, and 137.94° ± 7.8° respectively. This increase in water contact angle with increasing particle:polymer ratio can be seen in Figure 30 below. The sliding angle of all of these coatings was found to be extremely high, with an angle of 90° unable to induce a sliding motion in any water droplets on the surface (Appendix). This combination of high contact angles and high sliding angles is characteristic of the Wenzel wetting state. In the Wenzel state, the water droplet has a very high contact area with the surface as it sits within the groves of the surface features. This high contact area increases the adhesion forces between the surface and the droplet while the contact angle decreases due to the hydrophobic nature of the PDMS.[174,178,180]

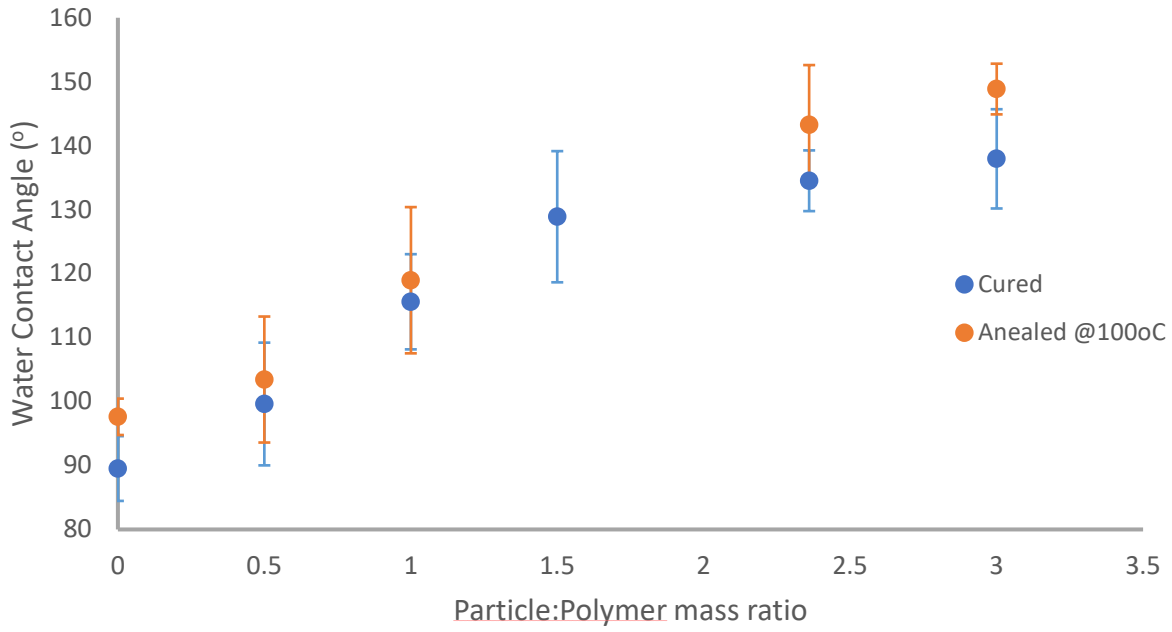

Figure 30: Effect of Particle:Polymer Mass Ratio on final coating water contact angle.

From Figure 30 it can also be seen that annealing the coatings at 100°C for 1 hour after they have been cured also results in an increase in contact angle, with a corresponding decrease in the sliding angle to $60^{o}<\theta<90^{o}$ (accurate measurements could not be performed due to instrumental limitations). This implies that during the annealing process the PDMS or particles move or settle in such a way to switch the wetting state from Wenzel to a mixed Cassie-Wenzel state. In the mixed Cassie-Wenzel state, the water droplet is partially sunken into the surface features, with some trapped air bubbles. In a similar way to the Wenzel state, this mixed state results in increased contact angles due to the increased contact area between the droplet and the surface. However, the presence of the trapped air reduces the contact area compared to the equivalent Wenzel state, which would in turn decrease the sliding angle somewhat, though there are still more adhesive forces than the ideal Cassie state.

From SEM images of these coatings (Figure 31), the coatings with more polymer than particle have a less distinct raspberry morphology, with the first two scales of roughness almost completely smoothed over in the 0.5:1 sample as the excess polymer fills in the gaps between both the small particles on top of the core and between the overall raspberry particles. This reduction in roughness would result in a lower aspect ratio, thus favouring either the Wenzel or Mixed wetting states over Cassie.[178,179] At a ratio of 1:1, the second scale of roughness becomes more pronounced, while the first scale remains relatively undefined as there is less excess polymer to fill in any gaps and create a smoother surface. The coating with a 1.5:1 ratio has a very well defined second scale of roughness with increasing definition for the first scale of roughness. The subsequent 2.4:1 and 3:1 coatings have roughly the same definition in their second-scale roughness as the 1.5:1 coating, however the first scale of roughness becomes more pronounced with increasing particle:polymer ratio. It is likely that if the particle:polymer ratio were to continue to increase further, there would no longer be enough PDMS to properly coat the raspberry particles, thus exposing their hydrophilic surface to the water droplet which could in turn reduce the contact angle again.[197] However, this was not reached during this project.

The third scale of roughness also appears to be affected by the particle:polymer ratio, with increasing particle proportions generally resulting in more dense arrangements of raspberry particles on the surface. The only exception to this is the 3:1 coating which had very similar particle densities to the 1:1 coating. As the particle packing becomes denser, the coating becomes more uniform across the surface. This would in turn reduce the likelihood that the water droplet would be touching uncoated glass thus lowering the contact angle. However, this change in the third scale of roughness may not be as critical as the first scale in terms of wettability. As mentioned, the 3:1 and 1:1 coatings appeared to have similar third-scale roughness from their SEM images, but the water contact angle increased from 115.6° for the 1:1 coating to 137.9° for the 3:1 coating. This increase of 22.3° cannot come from

the third scale of roughness as this remains relatively unchanged between these samples. As such this change is attributed to the large increase in definition of the first and second scales of roughness. However, as both the first and second scales of roughness have changed between these two samples this cannot provide any insight into how either one of these scales alone can affect wettability of the coating.

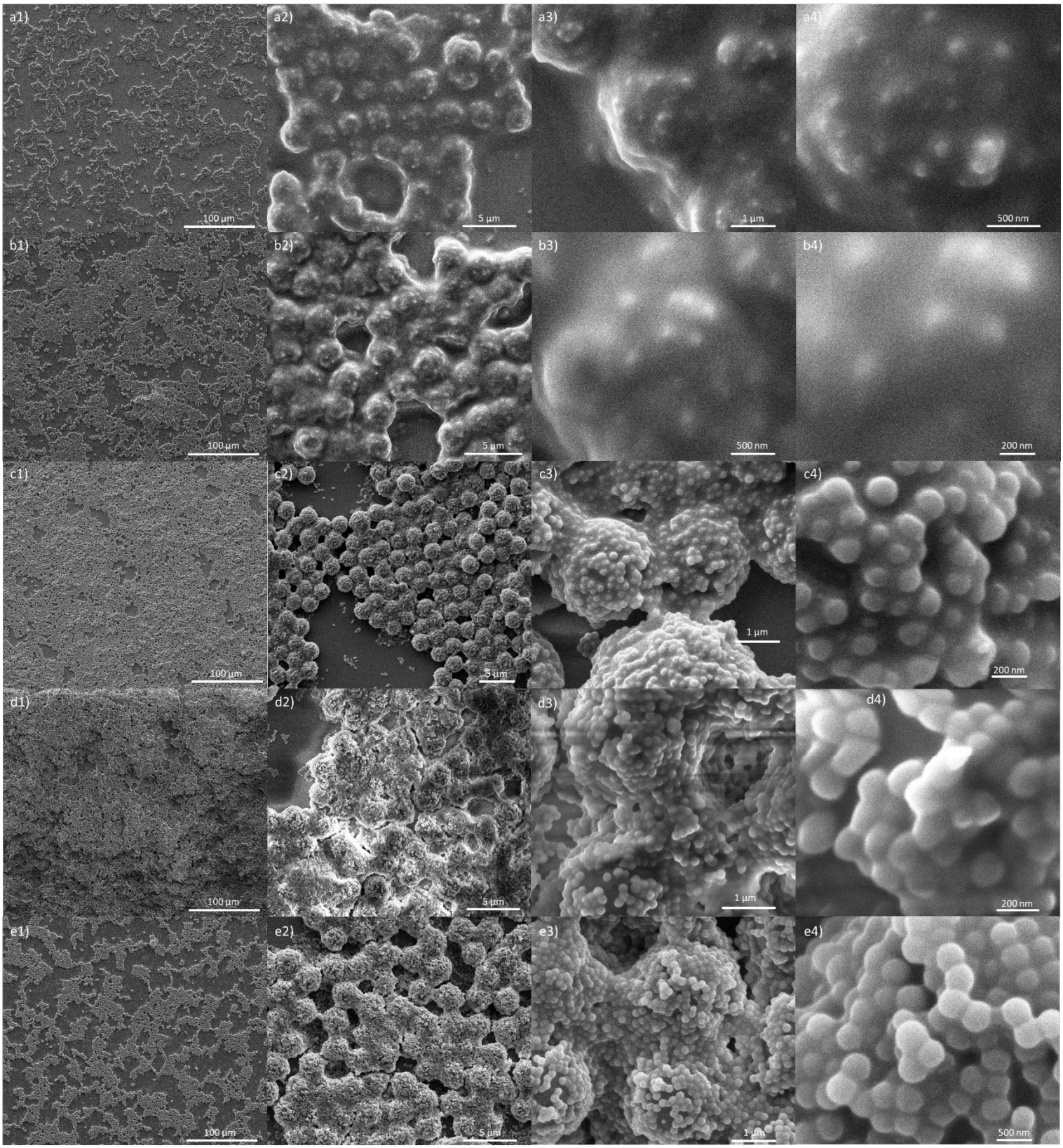

Figure 31: SEM images of raspberry PDMS coatings. Each column is a different magnification while each row has different particle:polymer ratios as follows: a1-4) 0.5:1, b1-4) 1:1, c1-4) 1.5:1, d1-4) 2.4:1, e1-4) 3:1

4.4.7 Effect of Raspberry Particle Size Ratio on Coating Wettability

Raspberry particles with small:large particle ratios of 0.045, 0.066, 0.101, and 0.108 were incorporated into coatings with particle:polymer ratios of 3:1. The water contact angles of these coatings were measured to be 155.5° ± 3.3°, 137.9° ± 4.7°, 154.9° ± 3.2°, and 157.5° ± 7.8° respectively. The sliding angles of most of these coatings were also found to be very low, with water droplets sliding off the surfaces as they are sitting flat for the 0.045, 0.101, and 0.108 coatings. Note that the 0.108 coating was least likely to have drops slide off the flat surface while the 0.101 coating was the most likely (Videos of sliding angles are presented in the supplementary information). In the instance that the water droplets would remain on the surface, these drops were used to measure the sliding angles as 12.0°, >60°, 6.82°, and 16.7° respectively. The relationships between particle size ratio, water contact angle, and sliding angle are shown in Figure 32 below. The SEM images for each of these coatings are shown in Figure 33.

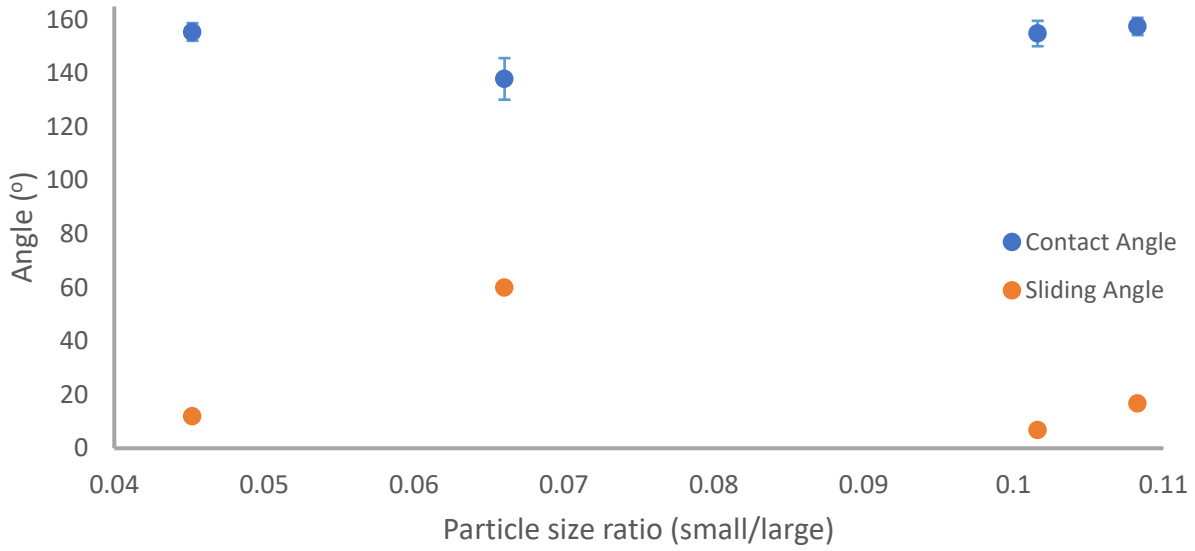

Figure 32: Water contact angles (blue) and sliding angles (orange) of raspberry particle-PDMS coatings with different particle size ratios.

Aside from the 0.066 coating there is no significant change in water contact angles across these samples, which implies that size ratio of small to large particles does not have a significant impact on wettability of the surface. However, the sliding angles do change from 16.7° to 6.8° with only a change in the size ratio of the small to the large particles from 0.108 to 0.101. From the SEM images, the third and second scales of roughness remain relatively unchanged from the 0.101 and 0.108 coatings with both samples having a very uniform distribution of raspberry particles with the same core size across the coated surface. Thus, the only significant change in the coating morphology is to the first scale of roughness with the decrease in small particle diameter (from 220.9 nm to 235.4 nm) resulting in a decrease in the observed sliding angle. The exact reason for this decrease is unclear and more research into the effect of size ratio on the sliding angle should be undertaken.

The 0.066 coating appears to be an outlier in both the water contact angle and sliding angle measurements. This could be due to the vast differences in the third scale of roughness in the produced coatings, with the 0.066 coating having a much sparser distribution of raspberry particles across the surface than the other coatings. The reason for this morphology difference is unclear as all coatings were made using the same method.

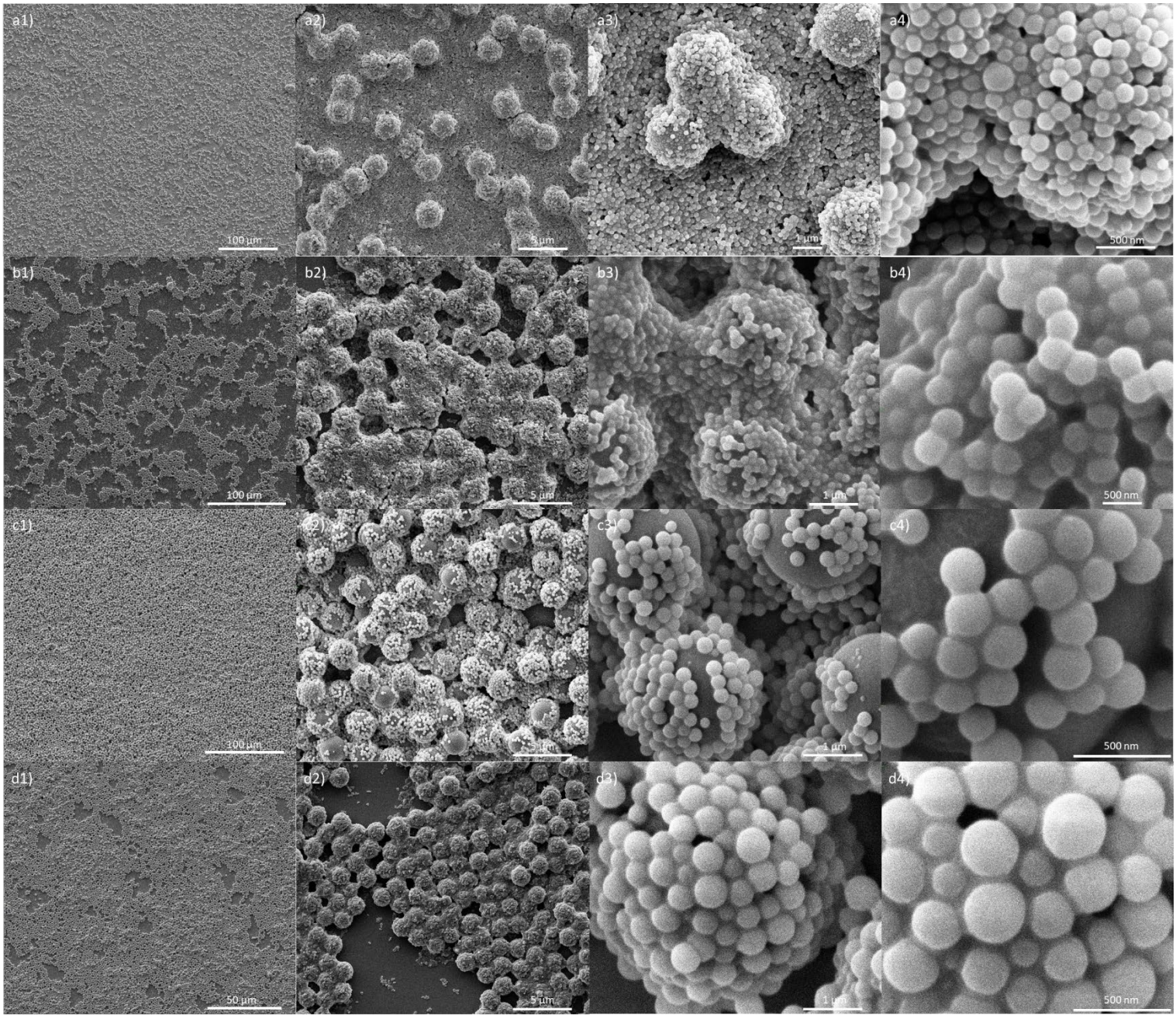

Figure 33: SEM images of raspberry PDMS coatings. Each column is a different magnification while each row has different small:large particle size ratio as follows: a1-4) 0.0452:1, b1-4) 0.0660:1, c1-4) 0.101:1, d1-4) 0.108:1,

The 0.045, 0.101, and 0.108 coatings had contact angles >150°C and low sliding angles of approximately 0° (or 12.0°, 6.82°, and 16.7° for pinned drops) which makes them superhydrophobic. These low sliding angles are very characteristic of the Cassie wetting state as the droplet sits on top of

the surface features trapping air bubbles in the roughened features. This drastically reduces the contact area between the drop and the surface, which in turn reduces the adhesion forces and allows the drop to slide off the surface at very low sliding angles. When considering the sliding angles of pinned drops, only the 0.101 coating can be considered superhydrophobic with a sliding angle of <10°. This could be due to the subtle changes in both the third and first scales of roughness but further research is required to investigate these scales as independent from one another.

4.5 Conclusion

In this chapter, we have presented a novel synthesis method for raspberry particles via the base-catalysed reaction of MPTMS and GPTMS based silica nanoparticles. This reaction results in high-density attachment (≥90%) of the thiol-terminated silica particles onto the larger epoxide-terminated silica particles with MPTMS particles greater than 90 nm in size. The lower attachment densities of the smaller particles (38 nm) may be due to reduced Van der Waals attractive forces being unable to overcome electrostatic repulsion. The sulphur state of the MPTMS particles was found to have negligible effects on the attachment density of the final particles. Zeta potential measurements showed that high pH can be used to create thiolate anions on the surface of MPTMS particles with both thiol and disulphide surface functionality.

Finally, these raspberry particles were incorporated into PDMS coatings and the hydrophobicity of the resultant coatings was investigated. The final coatings were found to have three scales of roughness: the size of the attached small particles, the size of the larger core particle, and the overall arrangement of raspberry particles on the surface. These scales of roughness were affected drastically by the mass ratio of particles to polymer in the coating solution, with increasing particle:polymer mass ratio resulting in an increase of the water contact angle from 103 ± 9.8° to 149 ± 4.0° for coatings with 0.5:1 and 3:1 ratios respectively. However, this ratio seemed to have little effect on the sliding angle with all samples having sliding angles of approximately 90°.

When raspberry particles with different size ratios were incorporated into PDMS coatings with a particle:polymer ratio of 3:1, the size ratio was found not to have a significant effect on water contact angle, with all coatings having contact angles of >150°. The sliding angles were dramatically decreased to <20°. The coating with a size ratio of 0.101 was very likely to allow drops to slide off the surface while flat and any drops that remained sitting on the surface had a sliding angle of 6.82°, making it the only true superhydrophobic coating produced.

Further investigation is necessary to determine the individual effects that each of these three scales of roughness have on the final properties of the coating.

Chapter 5: Thiol-Gold particle attachment

5.1 Summary

This chapter focuses on the development of a reaction for the attachment of gold nanoparticles onto the surface of silica particles.

Firstly, the relative affinity of gold particles for thiols and disulphides was tested via a small molecule model reaction with 3-methyl butanethiol and diisoamyl disulphide. This was then further confirmed by attaching the citrate-stabilised gold particles to both disulphide and thiol functionalised MPTMS particles.

Model attachment reactions were then conducted by attaching citrate-gold particles to glass functionalised with MPTMS and APTMS to determine whether amines or thiols would be more appropriate for gold particle attachment.

Lastly, the gold particles were attached to GPTMS silica particles at relatively high density via the use of a diamine linker molecule.

5.2 Introduction

Silica-Gold core-shell particles have been of interest since the late 1990s due to their potential applications in SERS,[86,237,240,241,315] biomedicine,[86,164,168] and laser perforation,[316] among others.[59,60,82,86] The production of these thin gold shells is often achieved by attaching small gold particles to use as seeds for further deposition or reduction of gold onto the particle surface to form a 'smooth' gold shell. [59,80,82-86,121,157-159,163-171] However, low initial seed attachment density tends to lead to uneven shell growth.[80,86] In addition, the idea of high-density attachment of gold particles leads to the question of whether gold particles in close proximity will behave as nanoparticles or as the bulk material, or have properties of both.

Westcott et al[251] reported the first attachment of gold nanoparticles onto a silica particle surface in 1998. In this paper, gold nanoparticles with a diameter of 2-3 nm were synthesised via reduction of cholorauric acid using THPC as a stabilising ligand. Silica particles with amine functional groups at the surface were synthesised by using TEOS and the Stöber process to grow the base particles at approximately 100 nm in diameter. These were then functionalised via the condensation of APTMS onto the particle surface before the particles were cleaned and redispersed in ethanol. By using this method, gold attachment densities of ≤30% were achieved.[251] This has since become the standard for the production of gold@silica core-shell structures.

There have been some modifications to this method,[121] including using citrate-stabilised gold particles,[81,156,157,164,171,237,239-243] testing of different TEOS particle surface functionality,[60,171] and growing gold particles directly onto the silica surface.[317,318]

However, this method has some limitations. The highest attachment density of seed gold nanoparticles achieved using this method appears to be 30% and the gold particles are often not very stable and have to be used within 1 week , or otherwise aged.[80] In addition, the ratio of gold particles to silica particles in the reaction mix is not often investigated, neither is the concentration of particle solids in the reaction solution. Both of which were found to be critical in high-density attachment of raspberry particles in Chapter 4: Thiol-Epoxy silica particle attachment.

In this chapter, a new method for the attachment of gold particles to silica particles was developed, and high gold to silica ratios and total particle concentrations were used to achieve higher attachment densities than reported in literature for other gold-silica attachments.

5.3 Methods

The methods relevant to this chapter are described in the following sections:

2.2.1.1 Method A, 2.3 Reduction of disulphides at MPTMS Particle Surface, 2.6 GPTMS Particle Synthesis, 2.10 Gold Particle Synthesis, 2.11 Gold Particle Ligand Swap, 2.12 Glass Functionalisation, 2.13 Gold Particle Attachments, 2.14.1 Sputter Coating, 2.14.2 SEM Imaging, 2.14.3 Characterisation of Particle-on-Particle Attachment Density, 2.14.5 FTIR Spectroscopy, 2.14.6 UV-Vis Spectroscopy, and 2.14.8 Dynamic Light Scattering.

5.4 Results and discussion

5.4.1 AuNp Synthesis

Citrate stabilised gold (citrate-gold) nanoparticles with an average diameter of 26 ± 7.5 nm were made using the Turkevich method and the resultant particles are shown in Figure 34.

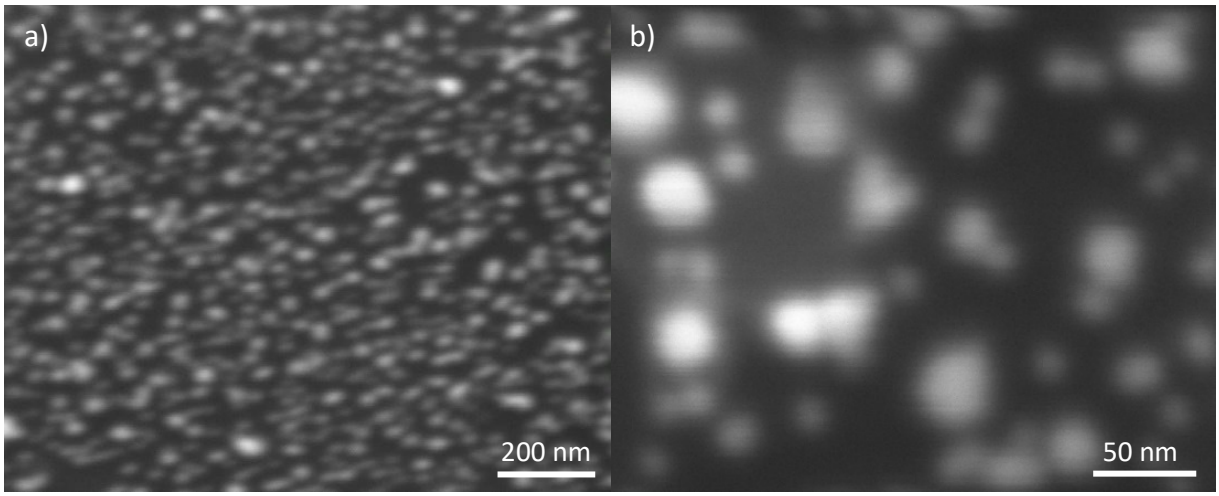

Figure 34: SEM images of citrate-gold particles

5.4.2 Small molecule model reaction

Following the discovery that MPTMS particles have predominantly disulphide groups at the surface rather than thiols (Chapter 3: MPTMS particle surface chemistry), ligand-exchange reactions were performed in order to test the citrate-gold particle's relative affinity for thiol and disulphide groups. The citrate-gold particles were mixed with solutions of 3-methyl butanethiol and diisoamyl disulphide as illustrated in Figure 35. The extent of ligand exchange was measured using FTIR, UV-Vis and DLS spectrometry.

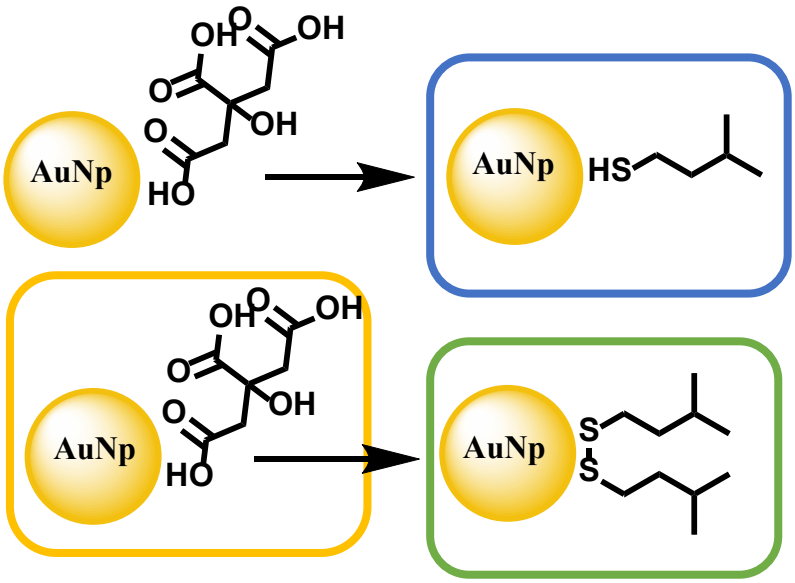

Figure 35: Gold nanoparticle ligand swap schematic

The gold ligand exchange samples were analysed via ATR-FTIR as shown in Figure 36 below. The carbonyl peaks for citrate can be seen at 1570 cm^{-1} and 1740 cm^{-1}.[319] As no C=O bonds are present in 3-methyl butanethiol or diisoamyl disulphide, the extent of the ligand exchange can be monitored by the reduction in these peaks. As can be seen in Figure 36b, the alkanethiol-gold sample still had some

residual carbonyl peaks in its FTIR spectrum, while the alkanedisulphide-gold does not. This implies that the gold is better able to bond to disulphides rather than thiols.

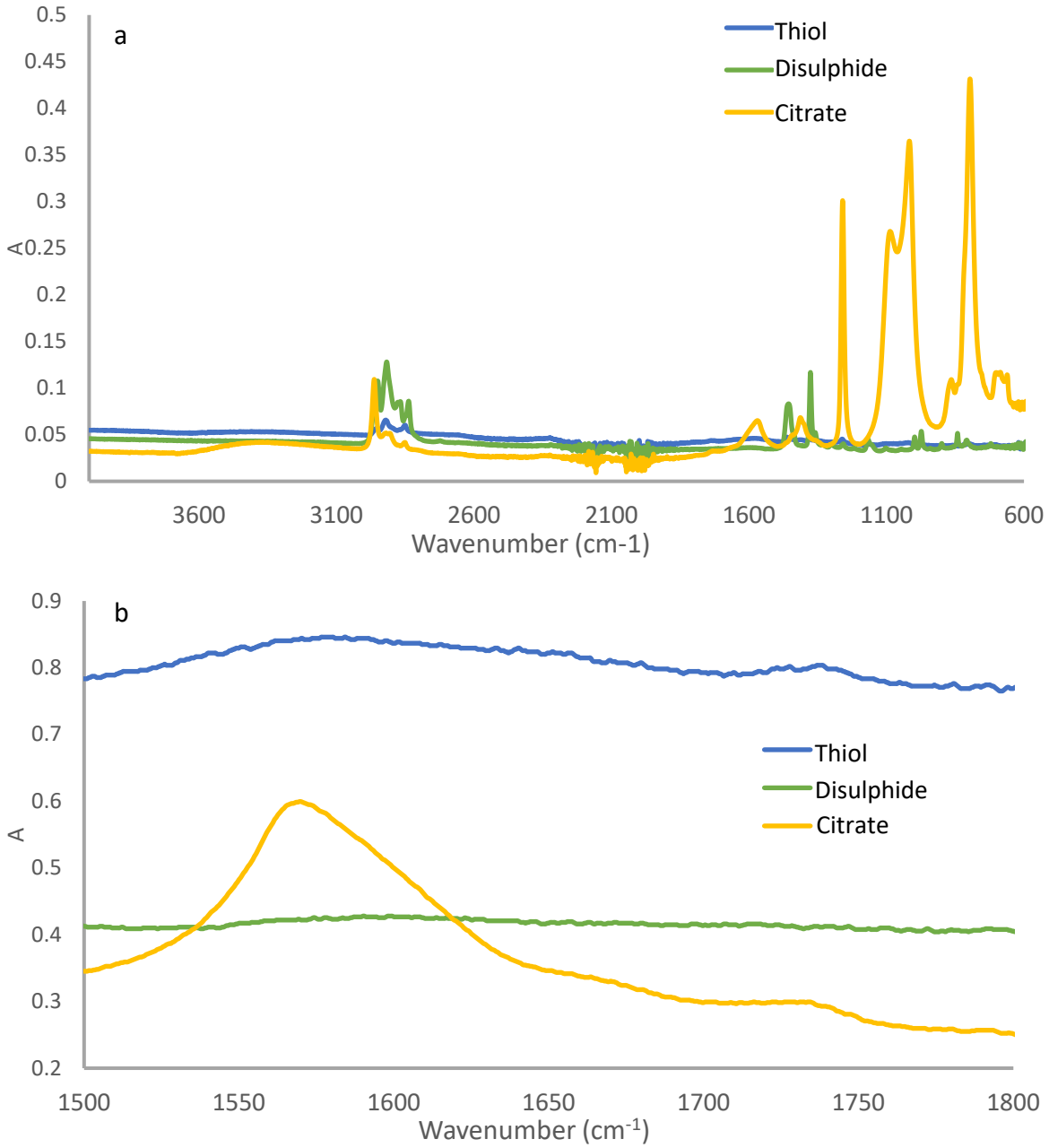

Figure 36: FTIR of gold ligand swap reactions. a) full spectrum b) region of interest around 1600cm^{-1}. Yellow is citrate-gold, blue is alkanethiol-gold, and green is alkanedisulphide gold.

A comparison of the UV-Vis spectra of the citrate-gold, the alkanethiol-gold and the alkanedisulphide-gold is shown in Figure 37a below. From this, it can be seen that citrate-gold has higher relative absorbance in the 400-550 nm range compared to both ligand swap samples. It also has lower relative absorbance at 650 nm and 725 nm compared to both ligand swap samples. The increase of absorption at higher wavelengths implies aggregation has occurred as the citrate is exchanged for the alkane thiol/disulphide molecules, which is to be expected as the alkane end groups are less miscible in water

than citrate and has lower electrostatic repulsion, both of which can lead to colloid destabilisation and aggregation. However, there is no discernible difference in the spectra for the alkanethiol- and alkanedisulphide-gold samples and as such no preference of gold particles for either the thiol or disulphide groups can be ascertained from UV-Vis analysis.

DLS was used as a more direct measure of particle aggregation than Uv-Vis analysis and is shown in Figure 37b below. From this, it can clearly be seen that the alkanedisulphide-gold has agglomerated more than the alkanethiol-gold sample, which implies that the ligand swap was more extensive for

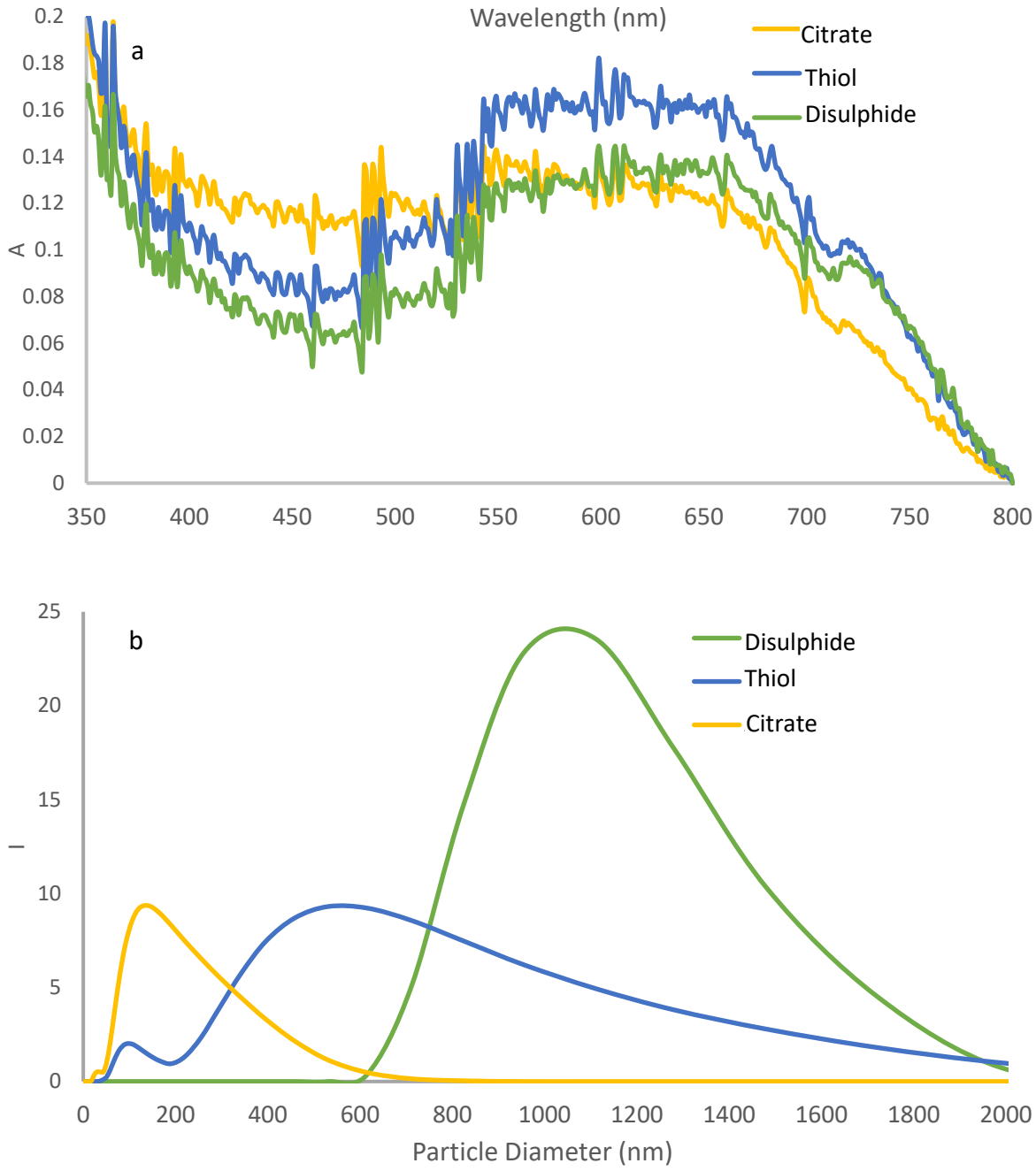

Figure 37: a) UV-Vis and b) DLS data for gold ligand swap reactions. Yellow is citrate-gold, blue is alkanethiol-gold, and green is alkanedisulphide gold.

the disulphide than the thiol. This in turn suggests that the gold is more likely to bond with disulphides than thiols, which supports the FTIR results.

5.4.3 Attachment of gold particles to MPTMS particles

In order to attach the citrate-gold particles to a larger silica-core particle and to investigate the effect of the sulphur oxidation state in the efficiency of the reaction, MPTMS particles were made and reduced as described in Chapter 3: MPTMS particle surface chemistry . The citrate-gold was then mixed with both the disulphide-silica particles (non-reduced MPTMS) and thiol-silica particles (reduced MPTMS) at the same conditions to see if the differences in gold-disulphide and gold-thiol attachments seen in the ligand swap reactions would persist in a significant way when trying to achieve particle-on-particle attachment. SEM images were taken of the gold-disulphide particles and gold-thiol particles and are shown in Figure 38a and Figure 38b respectively.

The attachment density was characterised as the number of gold nanoparticles per unit area of the core silica particle. The attachment density was also compared to a calculated "theoretical maximum" attachment density based on the sizes of the gold and silica particles. The thiol-particles had an attachment density of 118 ± 196 particles/um^2 (5.3 ± 5.5% theoretical max) while the disulphide-particles had an attachment density of 459 ± 270 particles/um^2 (13 ± 8% of the theoretical max). From this, it can be seen that the disulphide-particles had a higher average attachment density than the thiol-particles, which was expected from the previous gold ligand exchange reactions. However, both samples had very low attachment densities, much lower than were expected from the completeness of the ligand swap reactions. This is most likely due to electrostatic repulsion between the negatively charged citrate ligand and the negative surface charge of the silica particles. The zeta potentials of both the thiol- and disulphide-silica particles was measured across a range of pH values and is shown in Figure 25 in Chapter 4: Thiol-Epoxy silica particle attachment. These measurements show that both types of MPTMS particles have negative surface charges at a neutral pH, though the thiol-silica particles had a more negatively charged surface than the disulphide-silica particles. This would result

in more electrostatic repulsion and subsequently less attachment onto the thiol-silica particles compared to the disulphide-silica particles, which supports the experimental attachment densities.

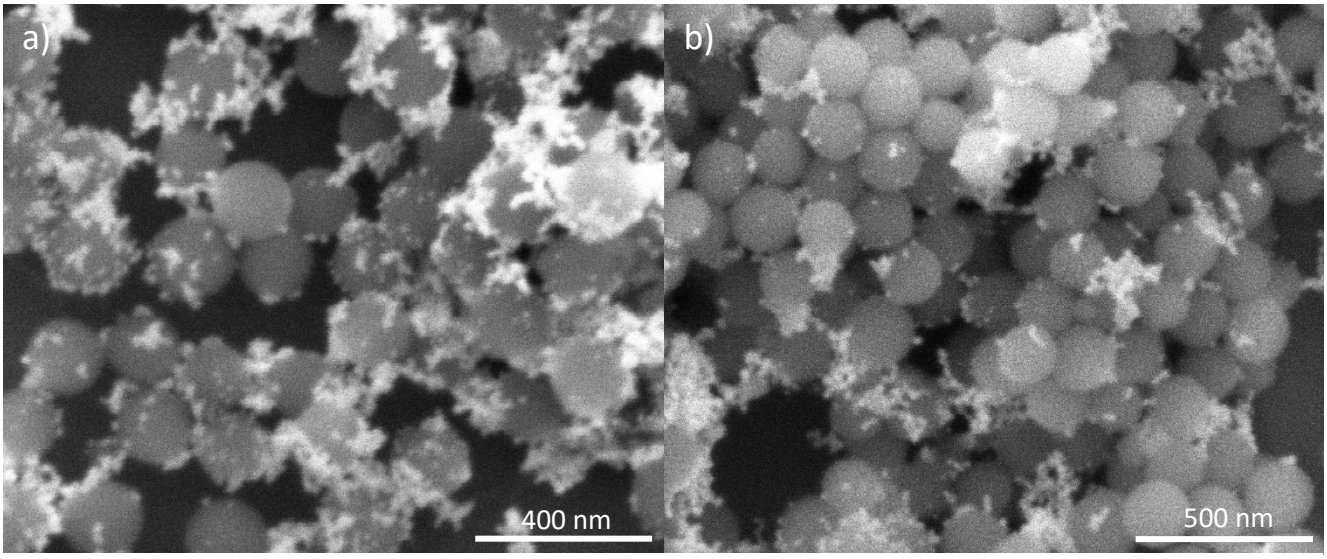

Figure 38: Attachment of citrate-gold nanoparticles to a) disulphide-silica particles and b) thiol-silica particles

5.4.4 Flat surface trials

In order to find an alternative functional group to overcome electrostatic repulsion during gold-silica particle attachments, test reactions were done on flat surfaces. In these reactions, citrate-gold nanoparticles were attached to glass slides that had been functionalised with MPTMS and APTMS.

From the SEM images (Figure 39), the attachment densities of citrate-gold particles on the MPTMS and APTMS surfaces after 2 hours were calculated to be 79 ± 18 particles/μm^2 and 1265 ± 139 particles/μm^2 respectively. Thus the APTMS was found to be 16 times more effective for citrate-gold particle attachment than MPTMS. From this, we can infer that amine functional groups are better suited to gold-particle attachment than thiols, despite the sulphur-gold covalent bond being much

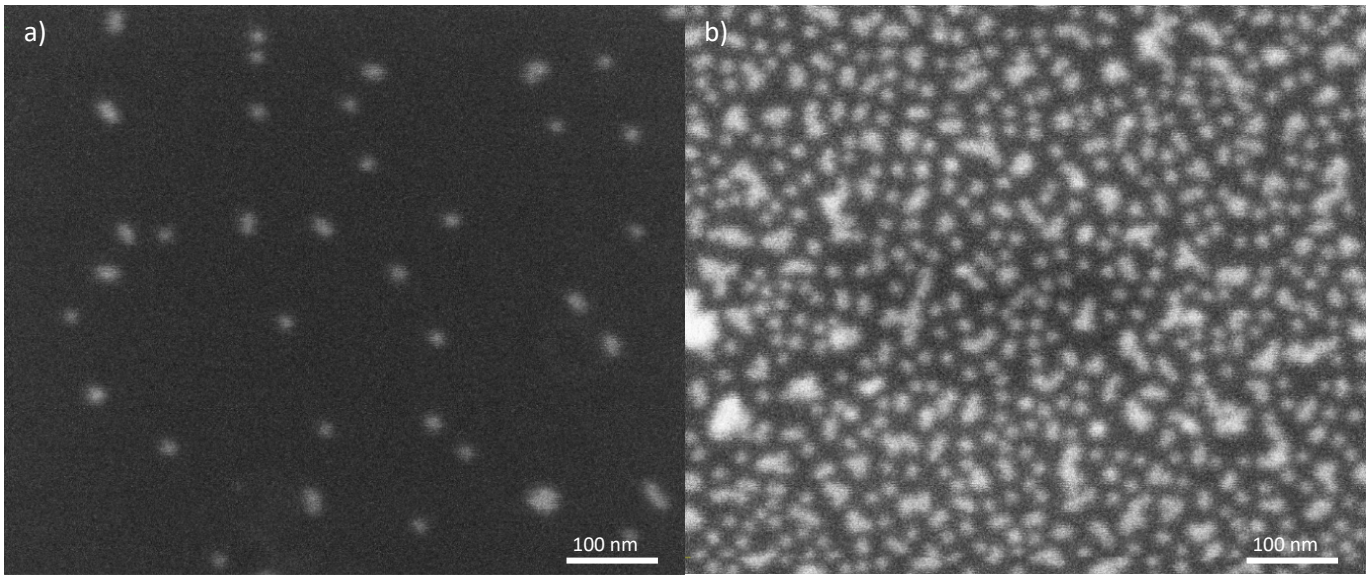

Figure 39: SEM images of citrate-gold particle attachment to a) MPTMS and b) GPTMS functionalised glass slides

stronger than the amine-gold electrostatic interactions. This could be due to electrostatic repulsion between the negatively charged thiol surface and the negatively charged citrate-gold particles that prevents the gold particles approaching the surface in a way where sulphur-gold bonds can be formed, while the positively charged amine surface would attract the gold particles.

The effect of reaction time and temperature on citrate-gold particle attachment for both APTMS and MPTMS surfaces was also investigated. UV-Vis spectrophotometry was used as a measure for relative attachment density by looking at the absorption of each sample at λ_{max} (529 nm).

The effect of reaction time on gold particle attachment to APTMS and MPTMS surfaces are shown in Figure 40a and Figure 40b below. From this, it can be seen that the APTMS samples achieved maximum attachment after 1 hour, with increasing reaction time having no effect. This is consistent with results found in literature.[241] However, the MPTMS samples were found to have increasing attachment with increasing reaction time up to 20 hours, which is contrary to reports by Vakarelski *et al* (2007)[320] and Chumanov *et al* (1995)[237]. Increasing temperature had a very small effect on attachment of citrate-gold particles to APTMS surfaces Figure 40c) with an increase of approximately 60°C only resulting in a 25% increase in attachment. The effect of temperature on MPTMS attachment Figure 40d) was found to be much more significant with a 60°C increase in reaction temperature resulting in a 685% increase in attachment.

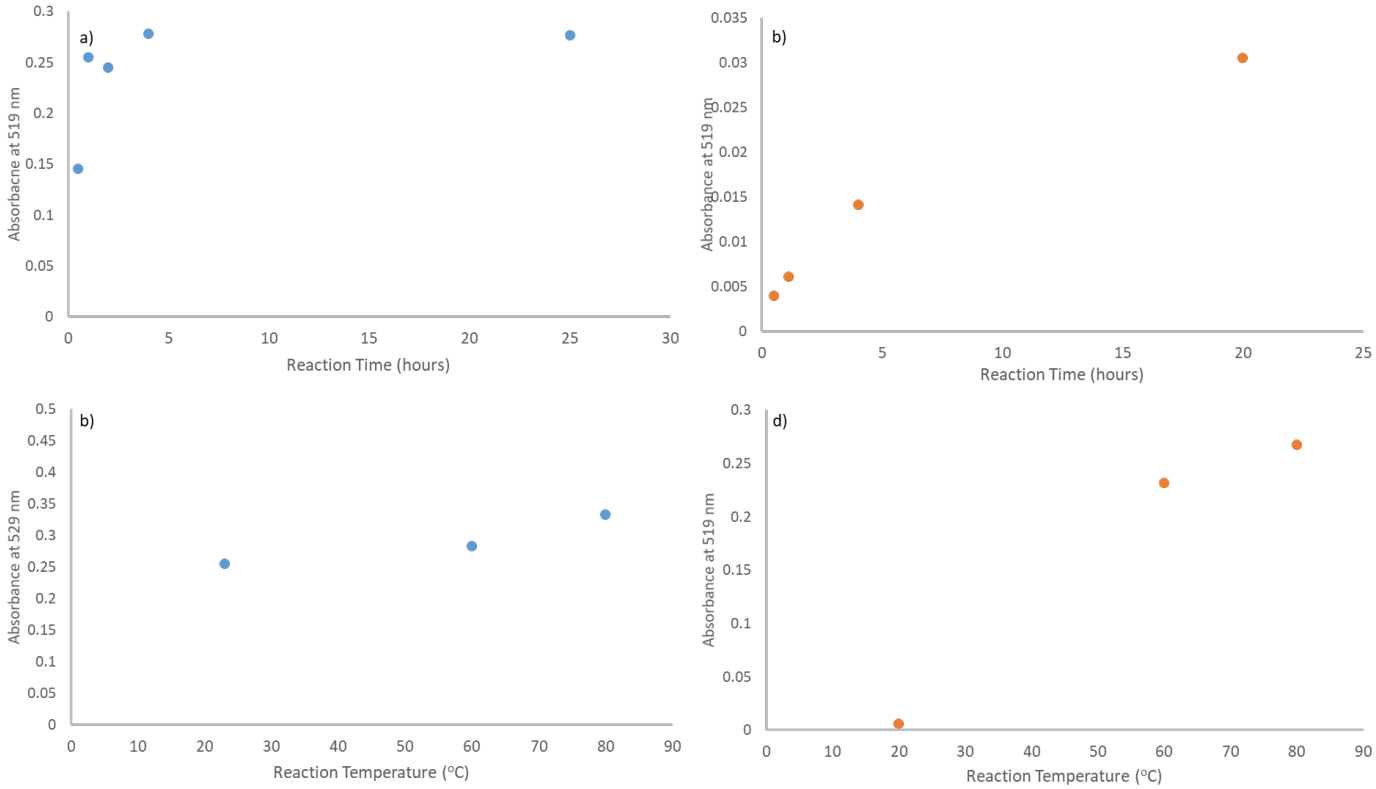

Figure 40: Effect of reaction time and temperature on the attachment of citrate-stabilised gold particles to functionalised glass surfaces. a) APTMS-functionalised, reaction time. b) MPTMS functionalised, reaction time. c) APTMS-functionalised, reaction temperature. d) MPTMS-functionalised, reaction temperature.

Increasing reaction time and temperature may fail to have a significant impact on attachment density on APTMS surfaces due to the surface becoming more negatively charged as citrate-gold particles are deposited which would in turn prevent gold particles from solution approaching the surface. In essence, the APTMS surface has already reached a saturation point. MPTMS on the other hand forms bonds with the gold particles that are stronger than the electrostatic repulsion between the surface and the particles. As such, though the particles have to overcome electrostatic repulsion to approach the surface, once there they would be far less likely to be removed from the MPTMS than the APTMS. In addition, the gold particle attachment on the MPTMS samples, even at high temperature and reaction time, remained lower than the APTMS samples so it is possible that the MPTMS sample had just not reached saturation with the given conditions and a similar plateau could be seen if longer reaction times and/or higher temperatures were tested.

When a highly concentrated solution of gold particles was left to dry on an APTMS-functionalised glass slide at 80°C, the resultant film changes colour depending on the viewing angle. At reflected angles, the film appeared to have a shiny 'yellow' gold sheen like that of bulk gold. However when held up to the light, the film appeared blue, like that of aggregated gold particles in solution. This phenomenon was investigated via transmission and reflectance UV-Vis spectroscopy and is shown in Figure 41 below. From this, it can be seen that the transmission spectrum has a higher absorbance in the 525 – 750 nm region than the reflectance spectra and vice versa for the 300 – 525 nm region. This difference in transmission and reflection spectra is characteristic of gold particles, with the Lycurgus Cup being one of the most famous examples.[321]

When comparing these spectra to that of bulk gold[322] the transmission spectrum of the gold particle film shares several characteristic with that of bulk gold. In particular, they both have a local minimum in absorbance at approximately 500 nm. However, the spectra are not identical as the gold film absorbance starts to decrease above 670 nm while the provided spectrum of bulk gold continues to increase until at least 1000 nm. The gold particle film also has a lower relative absorption below 450 nm than the bulk gold. The reflectance spectrum bears very little resemblance to both the particle films made at lower particle concentrations/temperatures (which had a peak at 529 nm).

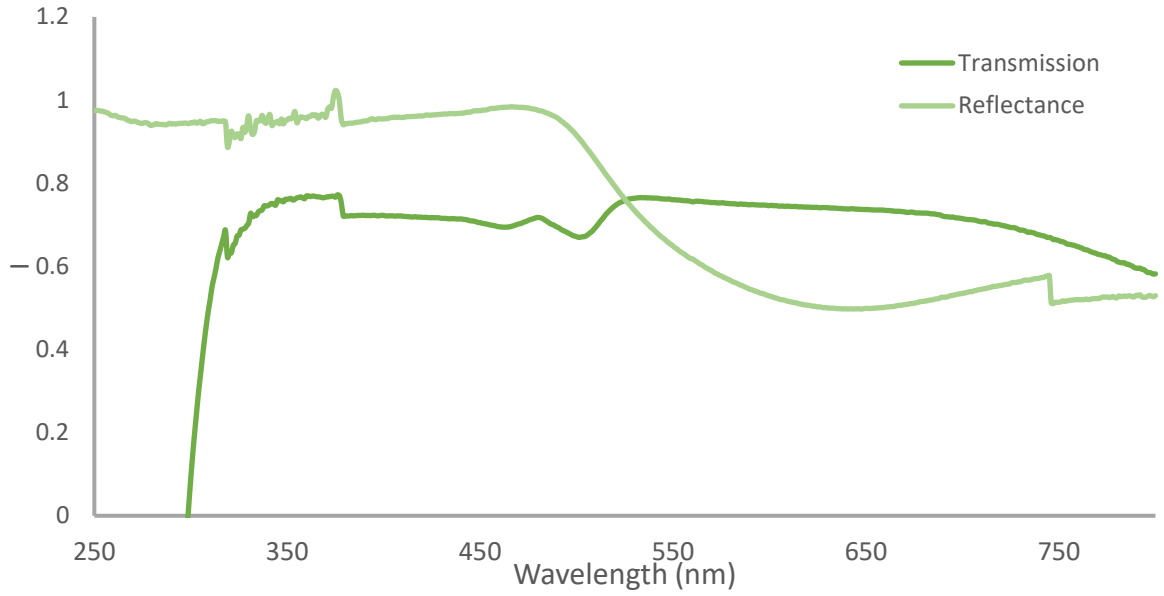

Figure 41: Transmission and Reflectance UV-Vis spectra for gold particle film attached to an APTMS surface at high concentration and temperature.

The combination of the observed bulk-gold like colour and the different reflection and transmission spectra implies that the particles are close enough together on the surface to give some of the properties of bulk gold while still being separate particles to give a nanoparticle effect. This brings up the question of where exactly and at what size a material switched from bulk to nano, and what properties can be achieved at the boundary between these two regimes. This also gives proof of concept that holding gold particles in close proximity can give interesting optical properties. Both of these ideas require further research.

5.4.5 Attachment of gold to epoxy-silica particles

Given that amines were found to be more effective than thiols for citrate-gold particle immobilisation on flat surfaces, a reaction scheme was devised to attach gold particles to GPTMS particles via a diamine-linking group. This was achieved by exchanging the citrate ligand on the gold particles for ethylene diamine. These amine-gold particles were then mixed with the epoxy-silica particles (from Chapter 4: Thiol-Epoxy silica particle attachment) where an amine-epoxy reaction would occur to bond the gold particles to the silica particles. This reaction scheme is shown in Figure 42 below.

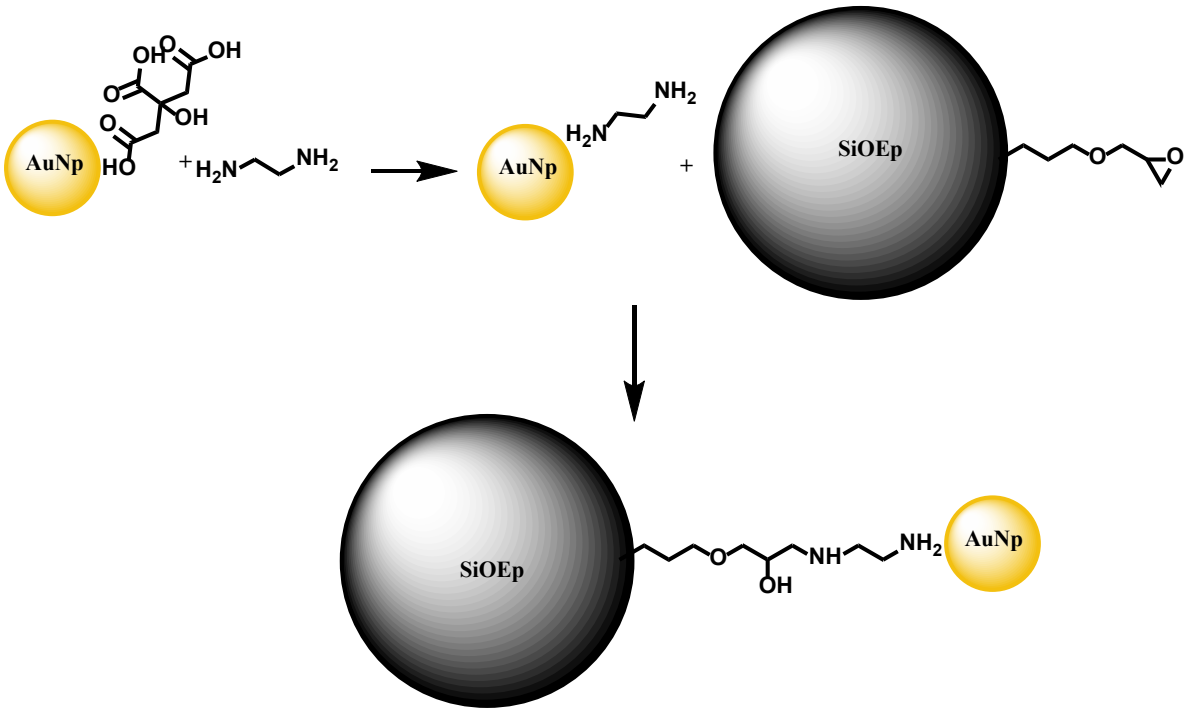

Figure 42: Gold-amine particle attachment scheme 1. Gold particles are first functionalised with an amine group before they are reacted with GPTMS particles.

In the first step, citrate-gold was mixed with an aqueous solution of ethylene diamine to exchange the citrate for the ethylene diamine. The resultant particles were analysed via SEM, and UV-Vis. In the SEM images (Figure 43), large agglomerates of gold particles can be seen that were not present in the citrate-gold particles shown in Figure 34. This is accompanied by a large shift in the UV-Vis spectrum (Figure 44) from a peak at 540 nm for a normal citrate-gold colloid to a consistently high absorbance across the visible spectrum. This agglomeration indicates that the citric acid has been switched for the ethylene diamine, which has fewer polar groups and would be somewhat less dispersible in water. However, the extent of the agglomeration is surprising given that if the ethylene diamine had attached in a highly ordered SAM, the molecule would be positioned such that there is an amine group protruding into the water. The agglomeration could be the result of either both ends of the ethylene diamine 'bridging' between gold particles or 'curling up' so that both ends of the amine are on the gold, leaving the hydrophobic middle section is exposed to the solvent.

Both ends of the ethylene diamine attaching to the same particle would be the less probable option as the reaction takes place in water and it would be unlikely that the ethylene diamine would arrange in such a way to expose the hydrophobic part of the molecule while hiding the hydrophilic ends. Especially considering the interactions between the gold and amine are electrostatic in nature, which are reversible and should allow room for molecular rearrangement post attachment. However, if the ethylene diamine was acting as a linking agent between the particles, large agglomerates would be expected as the gold particles are held in close proximity. Adding a large amount of ethylene diamine excess was done in an attempt to avoid this issue by increasing the probability of particle-solution amine interactions while reducing the probability of particle-particle interactions. Nevertheless, it appears to be the most likely occurrence, given the appearance of large agglomerates in the SEM images and the extent of the colour shift in the UV-Vis spectra from citrate-stabilised gold to amine-gold.

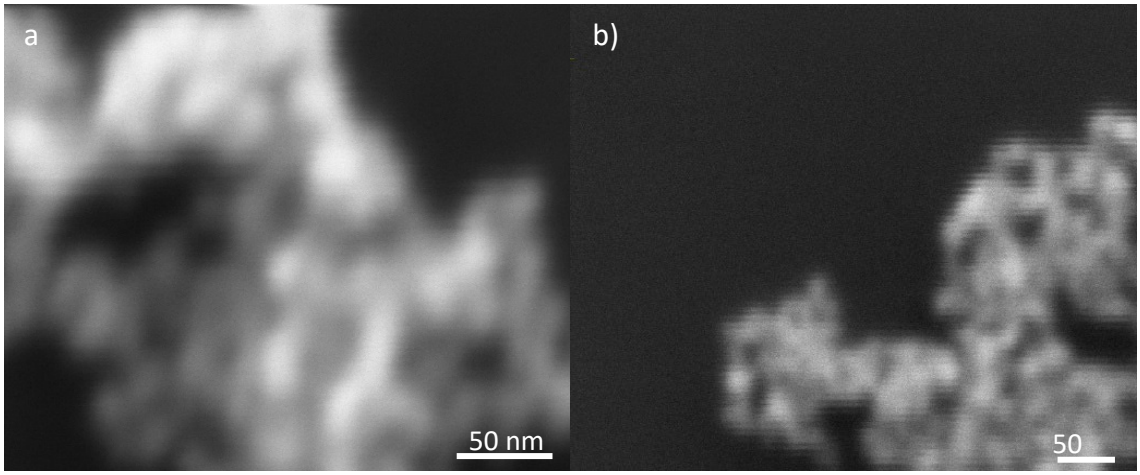

Figure 43: Gold particles after ethylene diamine ligand swap. Sample was prepared by drying a drop of particle suspension on a silicon wafer.

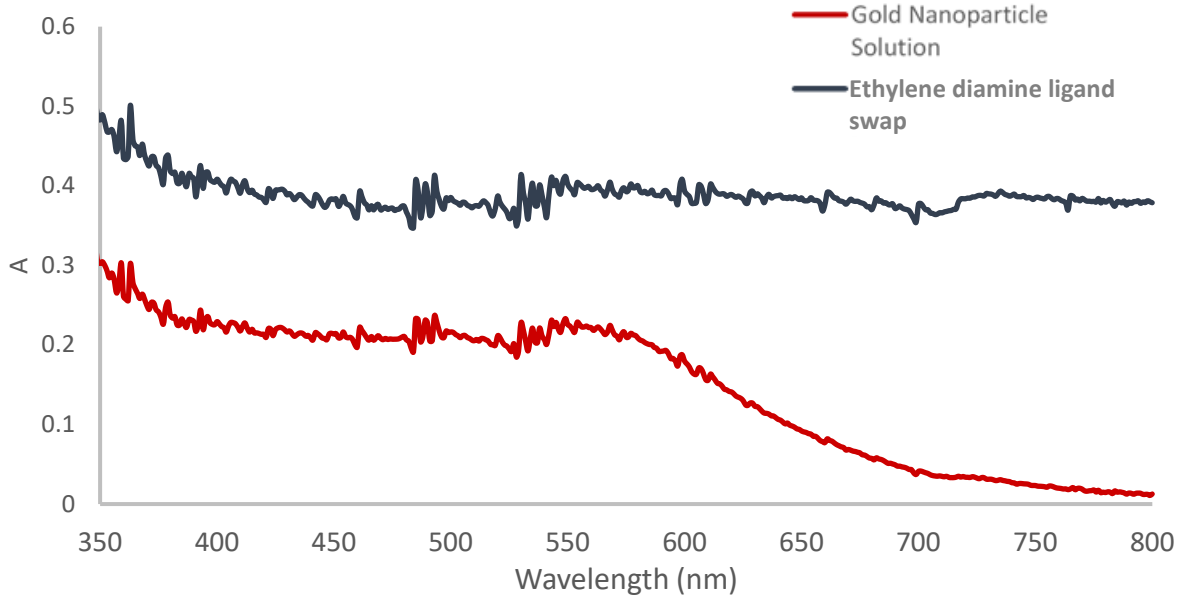

Figure 44: UV-Vis of citrate-amine gold ligand swap. Black is amine-gold ligand swap. Red is normal citrate-gold.

The amine-gold particles were mixed with epoxy-silica particles in water and allowed to react overnight with 100 times excess of gold particles (with 1 time excess being the amount of gold particles needed to form a monolayer on the silica particle surface). The final gold-silica particles were analysed via SEM (Figure 45). The resultant attachment of gold onto the silica was very low and inconsistent, with an attachment density of 13 ± 16 particles/μm^2 or 0.8 ± 1.0 % of the theoretical maximum. Interestingly at the solvent edge of the drop-casted SEM sample, higher gold attachment was seen. However, the gold particles had aggregated/coalesced to form "noodle" like shapes on the surface of the silica particles. These strange formations could be due to the aggregation of the amine-gold particles prior to the epoxy-silica attachment.

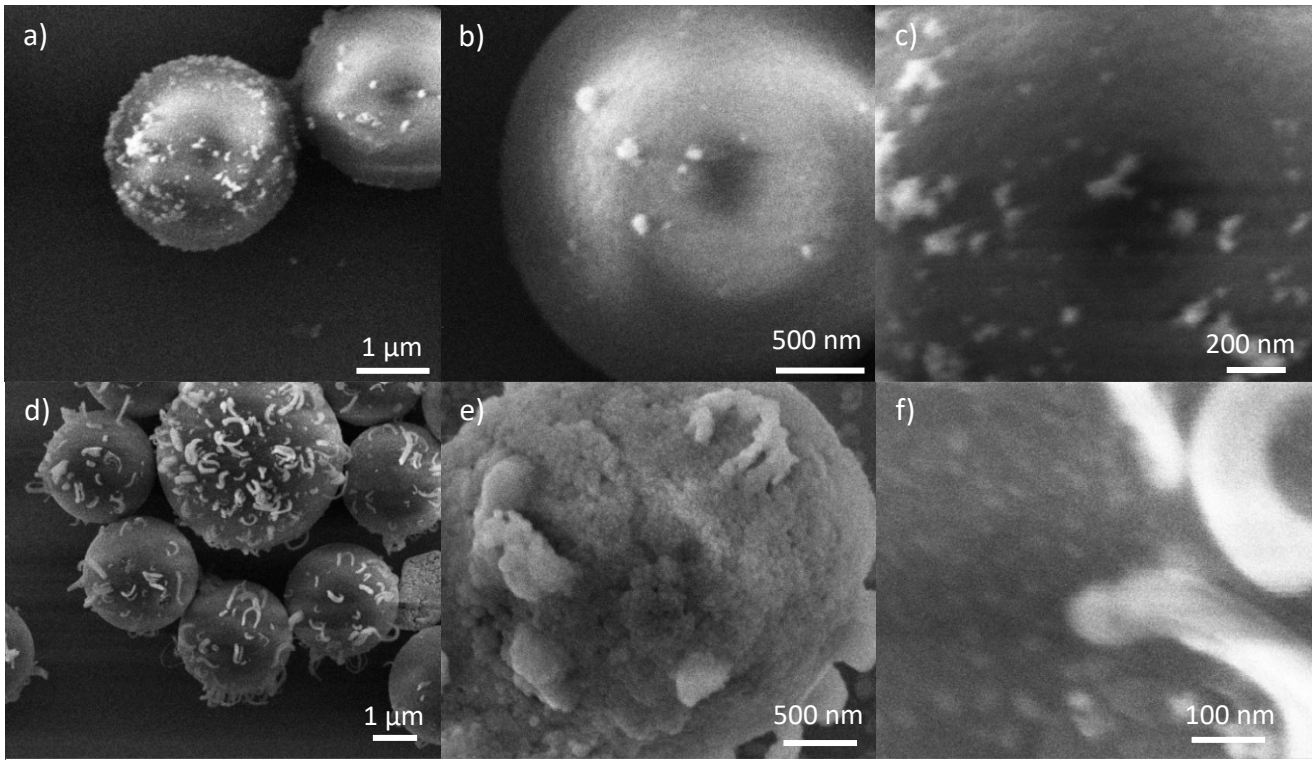

Figure 45: Gold-silica particles resulting from the attachment of amine-gold particles to silca-epoxy particles. a-c) particles at the centre pf the dried drop. d-f) particles from the solvent front of the dried sample.

In order to avoid the gold particle agglomeration an alternative reaction scheme was devised. The ethylene diamine was first reacted with the epoxy-silica particles via an amine-epoxy nucleophilic ring-opening reaction. This results in the surface functional group conversion from an epoxy to an amine. The citrate-gold particles were then mixed with the amine-silica particles at 100x excess of gold particles. This reaction scheme is shown in Figure 46 below. The resultant gold-silica particles were analysed via SEM and UV-Vis.

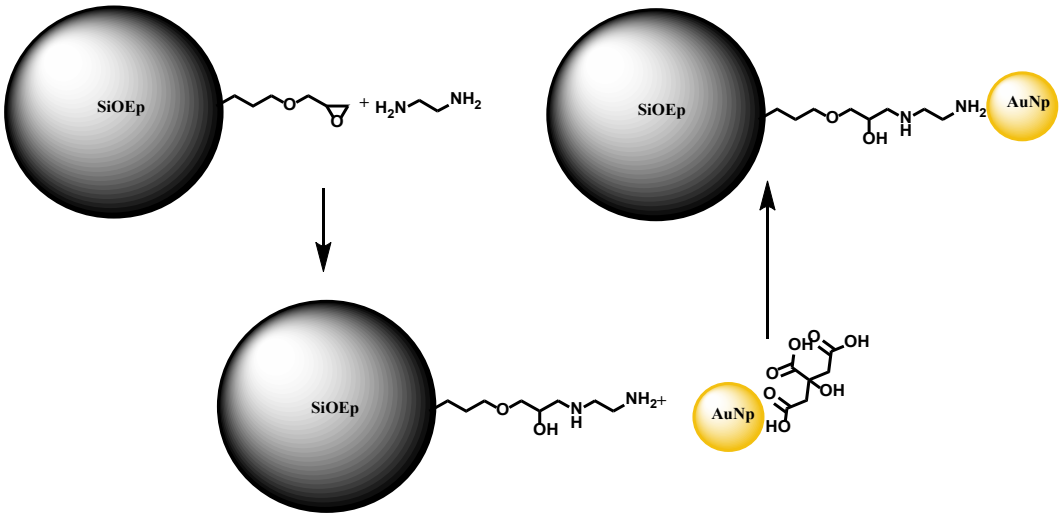

Figure 46: Gold-amine particle attachment scheme 2. GPTMS particles are first functionalised with an amine group before they are reacted with citrate-gold particles.

The SEM images in Figure 47 below show a high and uniform attachment of the citrate-gold particles onto the silica particles, with an average attachment density of 852 particles/µm^2 or 39 ± 16% of the theoretical maximum. These high attachment densities are accompanied with a substantial shift in the UV-Vis spectrum (Figure 48). The normal citrate-gold colloid has a peak at approximately 540 nm whereas the gold-silica particles have a high absorption across the entire visible spectrum, corresponding with a colour change from red to blue/black. This UV-Vis spectrum is very similar to that of the aggregated gold particles seen in Figure 44 above, however the SEM shows no gold aggregates. Instead, individual gold particles are attached to the surface of the epoxy particles.

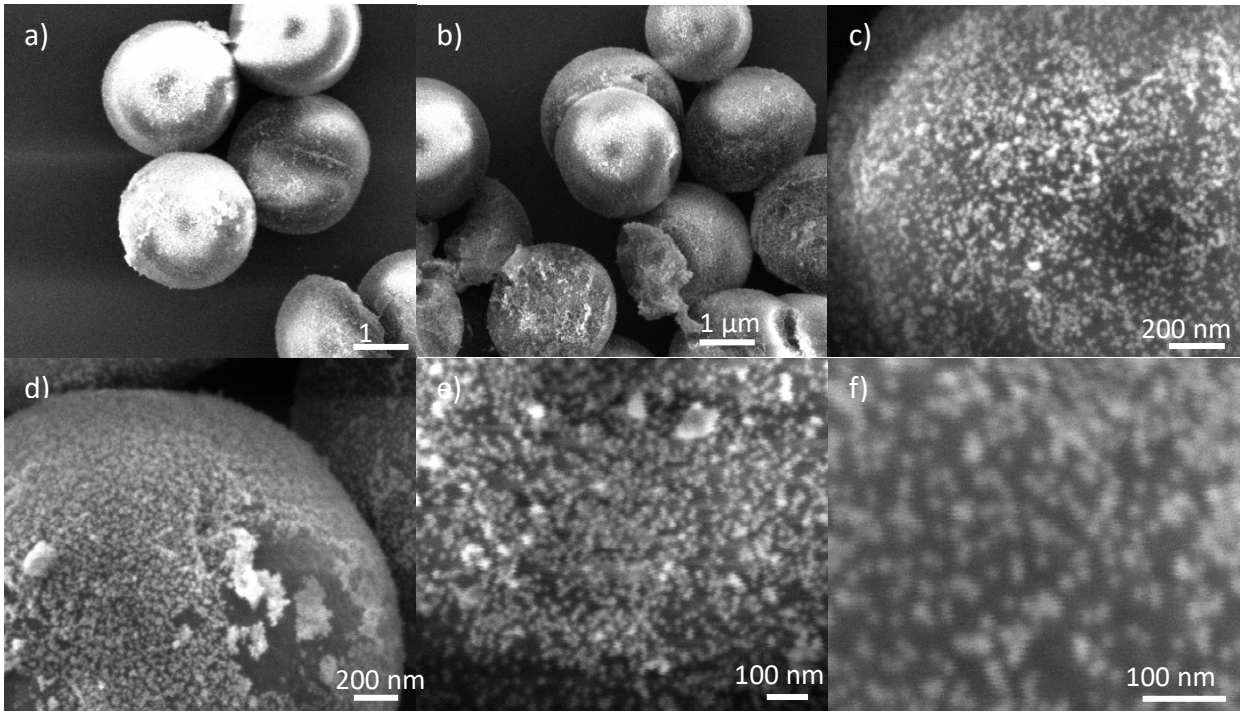

Figure 47: Gold-silica particles resulting from the attachment of citrate-gold particles to amine-functionalised epoxy particles at different magnifications.

The close proximity of these gold particles could be causing coupling of their plasmon resonances in such a way that the UV-Vis spectrum appears like that of aggregated gold particles.

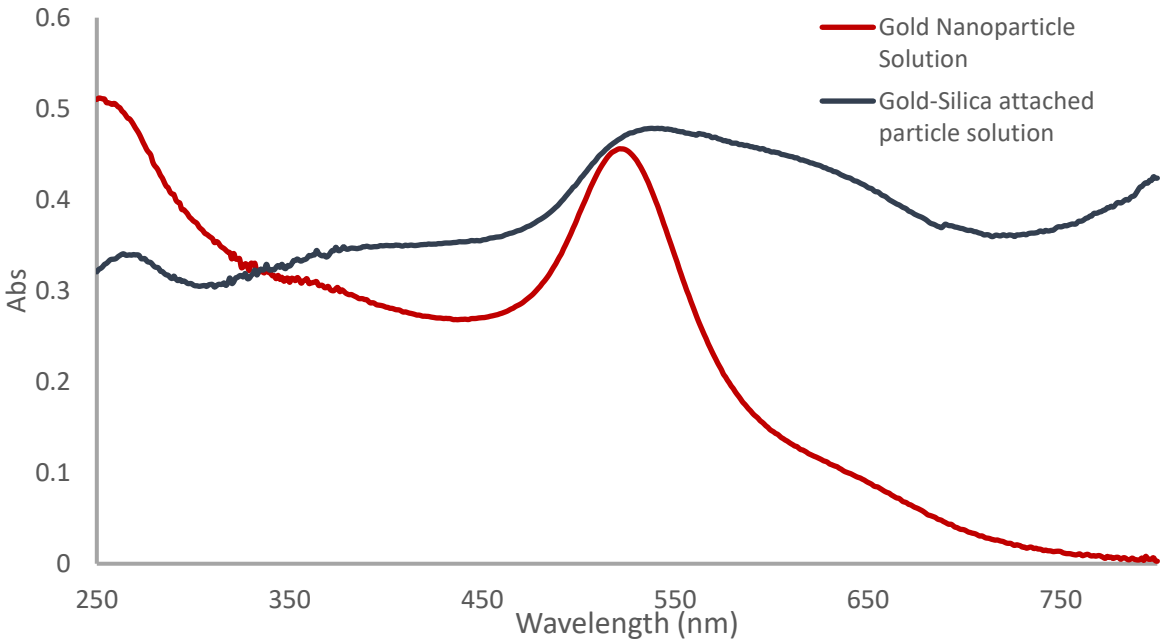

Figure 48: Uv-Vis comparison of citrate-gold (red) and gold-silica raspberries (black)

This attachment density of 39 ± 16% is higher than any other gold-silica particle attachment densities reported in literature where the highest attachment density appears to be approximately 30%.[80] This high attachment density could be the result of having a higher gold particle concentration and excess than usually used in literature. Westcott et al (1998)[251] achieved attachment densities of ≤30% by using only 1x excess of small particles. In order to test the effect of gold particle excess on the resultant gold-silica attachment density, the attachment reaction was repeated with 1, 50, and 100 times excess of gold particles. The SEM images for the resultant gold-silica particles are shown in Figure 49 below. The attachment densities of the 1, 50, and 100 times excess reaction were found to be 3.7 ± 1.9%, 23 ± 15%, and 41 ± 12% respectively. This is a strongly linear trend, as shown in Figure 50 below.

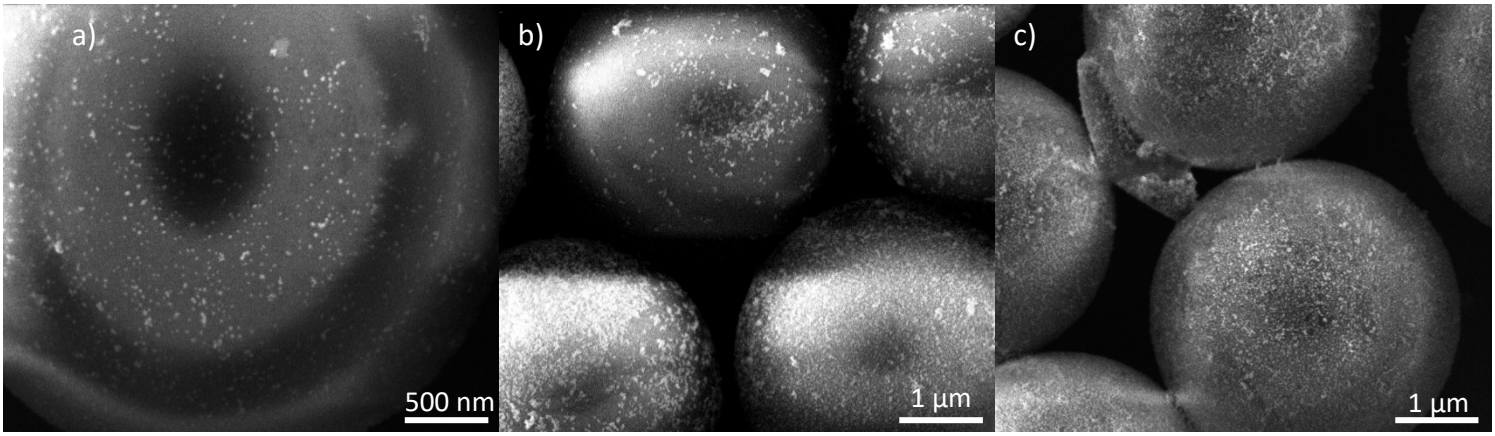

Figure 49: SEM images of gold-silica particle attachment conducted with a) 1 time, b) 50 times, and c) 100 times particle excess.

From this it can be seen that high attachment densities of >30% can only be achieved with a large gold particle excess. This is unsurprising as it has been found that when attaching small molecules onto particle surfaces high attachment densities are only achieved at very high molecule excess.[195]

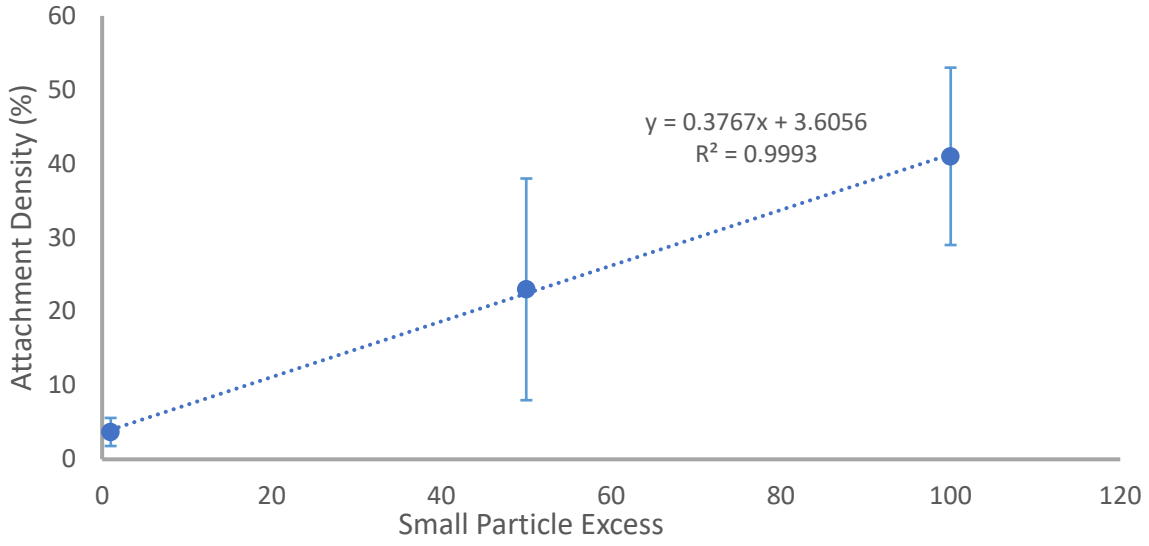

Figure 50: Dependence of final gold particle attachment density on the excess concentration of gold particles in the reaction solution.

5.5 Conclusion

In this chapter, it has been shown that citrate-stabilised gold nanoparticles are more effectively able to attach to and ligand exchange with disulphide groups rather than thiols. Similarly, unreduced (disulphide-functionalised) silica particles were found to have higher gold particle attachment densities than the corresponding reduced (thiol-functionalised) silica particles. However, neither thiol- or disulphide-functionalised MPTMS particles are capable of achieving high citrate–gold particle attachment due to electrostatic repulsion between the negatively charged surfaces. To this end, amines appear to be a more effective attachment group for citrate-stabilised gold particles than sulphur-containing groups, despite the differences in final bond strength. This is likely due to the positively charged amine having attractive electrostatic interactions with the negatively charged citrate-gold particle.

In addition, when attaching gold particles to the GPTMS particles, the order of operations in is important. The ethylene diamine should first be attached to the epoxy rather than to the gold in order to prevent aggregation of gold before the subsequent attachment reaction can be conducted. This order results in much higher attachment density. It was also found that large gold particle excess and higher total particle concentrations are required for high attachment densities to be achieved.

Once attached to the silica core particle, the plasmon resonance peak of the gold particles broadens substantially and appears blue/black instead of red. This implies that the gold particles are close

enough that the plasmon resonances can couple in much the same way as when gold particles aggregate.

Chapter 6: Conclusions and Future Work

6.1 Conclusion

The development of new materials with complex microstructures has a wide variety of applications including superhydrophobic coatings, drug delivery, synthetic opals, antifouling, and catalysis.

One way in which these types of materials can be obtained is through the attachment of nanoparticles to one another, particularly nanoparticles of different sizes and materials. As such, the development of new methods to attach particles of different sizes and materials to each other is an important field of study. In particular, the use of silica-on-silica and gold-on-silica raspberry particles in the development of superhydrophobic, and photonic materials was investigated in this work.

In Chapter 3, the disulphide to thiol ratio of silica particles grown from MPTMS was systematically investigated using Raman Microscopy and Ellman's Reagent assays. It was initially found that the oxidation of the thiol groups in MPTMS to disulphides was a by-product of the particle synthesis reaction. In addition, particles made via modified Stöber processes with MPTMS as the sole precursor were found to have significantly more disulphide groups than thiols, in contrast to the surfactant method, where significantly more thiols than disulphides were observed. This indicates that the synthesis method has a very significant impact on the state of the final sulphur-containing groups. It was also found that the disulphide groups were at the surface of the particle, not just the interior, as reaction with tributylphosphine increased the thiols present.

The effect of different reagent concentrations on thiol oxidation during the modified Stöber process showed that increasing ammonia concentration resulted in an increased ratio of disulphides to thiols while increasing ethanol concentration resulted in decreased thiol oxidation. Atmospheric oxygen was also found to participate in the formation of disulphides leading to a proposed reaction mechanism for the formation of disulphides.

In Chapter 4, a new synthesis reaction was presented for the formation of raspberry particles via the base-catalysed reaction of MPTMS and GPTMS based silica nanoparticles. This reaction results in high-density attachment (≥90%) of with a variety of MPTMS particle sizes. The thiol oxidation state of the MPTMS particles was found to have negligible effects on the attachment density of the final particles.

This reaction method enables a combinatorial approach to the formation of multiscale coatings using PDMS as the binder. This investigation showed the effect of particle:polymer mass ratio and

small:large particle size ratio on the wettability and sliding angle of the final coatings. The particle:polymer ratio of 3:1 and a small:large ratio of 0.101:1 was found to give a superhydrophobic coating, with a contact angle of 157°, a sliding angle of 6.82°, and a high probability of sliding at 0°.

Lastly, in chapter 5 a new synthesis method was developed for the attachment of citrate-stabilised gold particles to silica particles. Disulphide groups were found to be a more effective ligand exchange agent for the citrate-stabilised gold particles than thiol groups. However, both thiols and disulphides were consistently found to underperform amine groups in terms of gold attachment, despite the differences in the final gold-sulphur and gold-amine bond strengths. From this, it can be concluded that the citrate stabilising ligand plays a highly significant role in the attachment of gold particles.

In the final method developed, GPTMS silica particles were modified with ethylene diamine before a suspension of citrate-gold particles was added. It was found that large gold particle excess and higher total particle concentrations are required for high attachment densities to be achieved. This method resulted in attachment densities of ≥40%, which is higher than similar attachments in literature. The high attachment density allowed for plasmon resonance coupling between the gold particles, resulting in a broadening of the plasmon peak.

6.2 Future Work

There are several ideas brought up in this work that require further investigation. These include:

(i) Modelling the formation of disulphides during MPTMS particle synthesis to gain a deeper understanding of the particle growth mechanism.
(ii) Increasing the durability of the superhydrophobic raspberry particle coatings.
(iii) The role of size ratio in the wettability of the raspberry particle/PDMS coatings.
(iv) Increasing the attachment density of the gold-on-silica raspberry particles
(v) Preparation of high-density gold nanoparticle materials and exploration of their potential optical properties.

Chapter 7: Appendix

A1: Raman Spectra for MPTMS Particles made from different ammonia and ethanol concentrations.

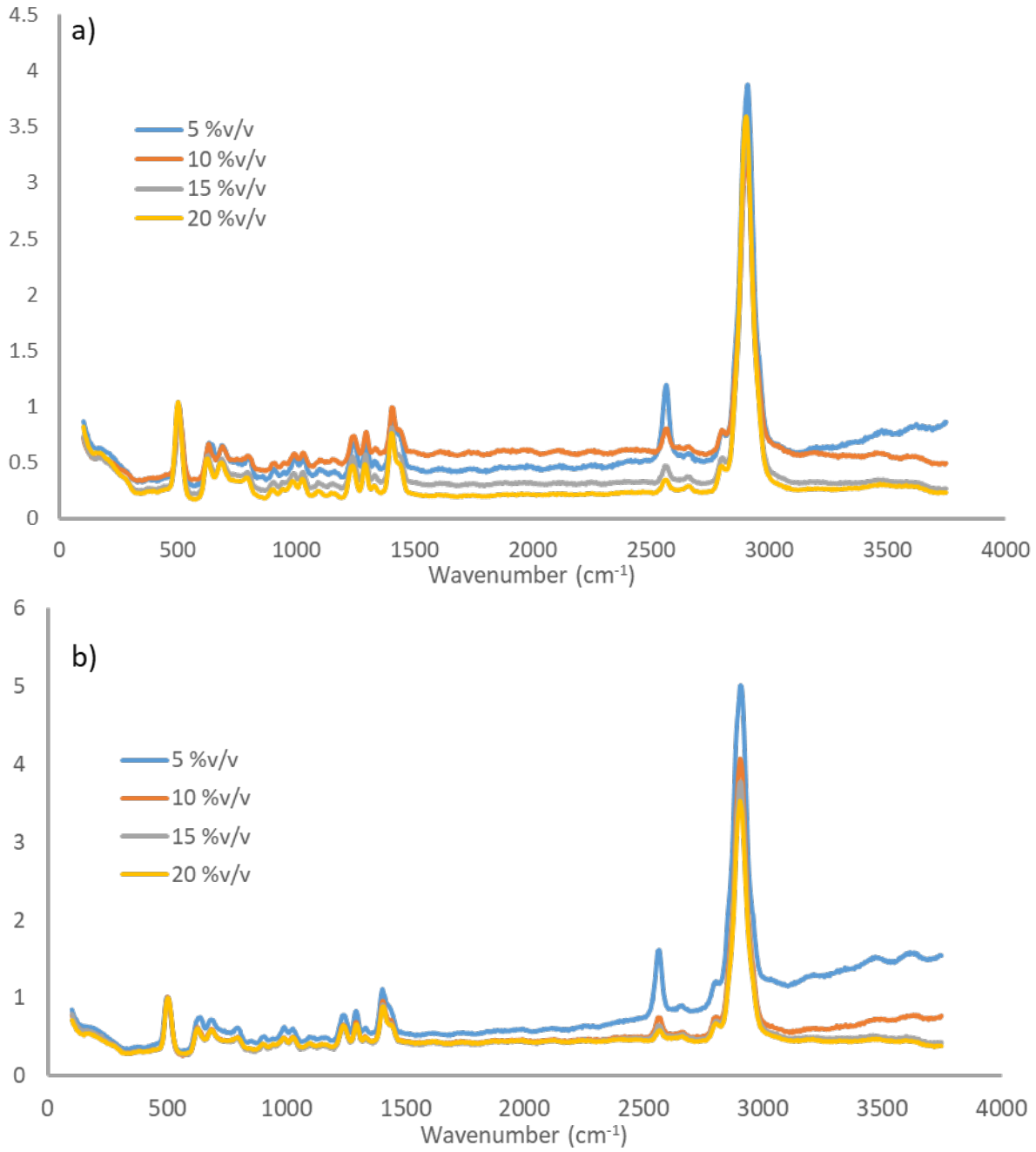

Figure 51: Raman Spectra for MPTMS particles made using different ammonia concentrations. a) Method A, b) Method B.

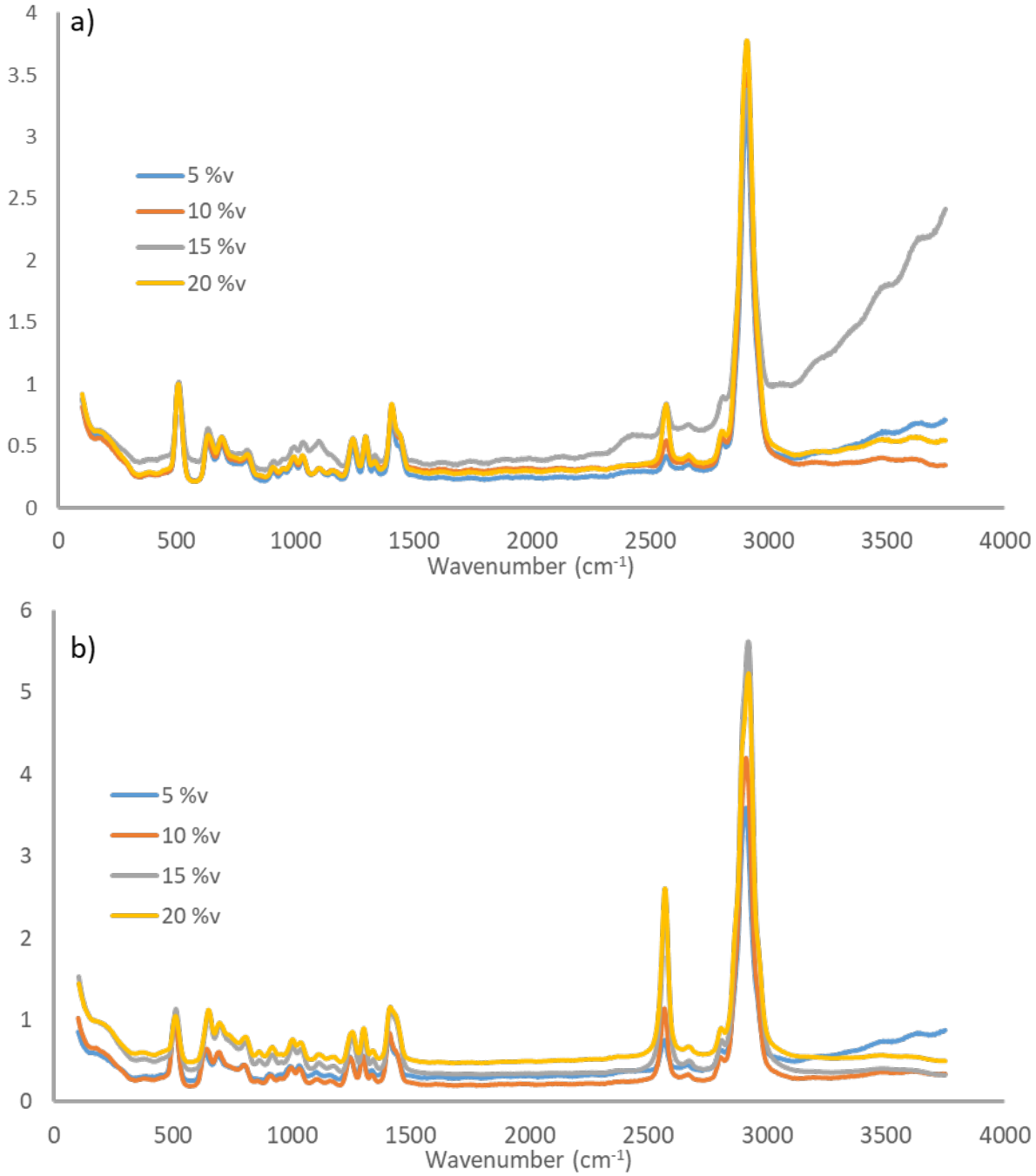

Figure 52: Raman Spectra for MPTMS particles made using different Ethanol concentrations. a) Method A, b) Method B.

A2: Comparisons of volume:surface area and disulphide:thiol ratios for different ethanol and ammonia concentrations.

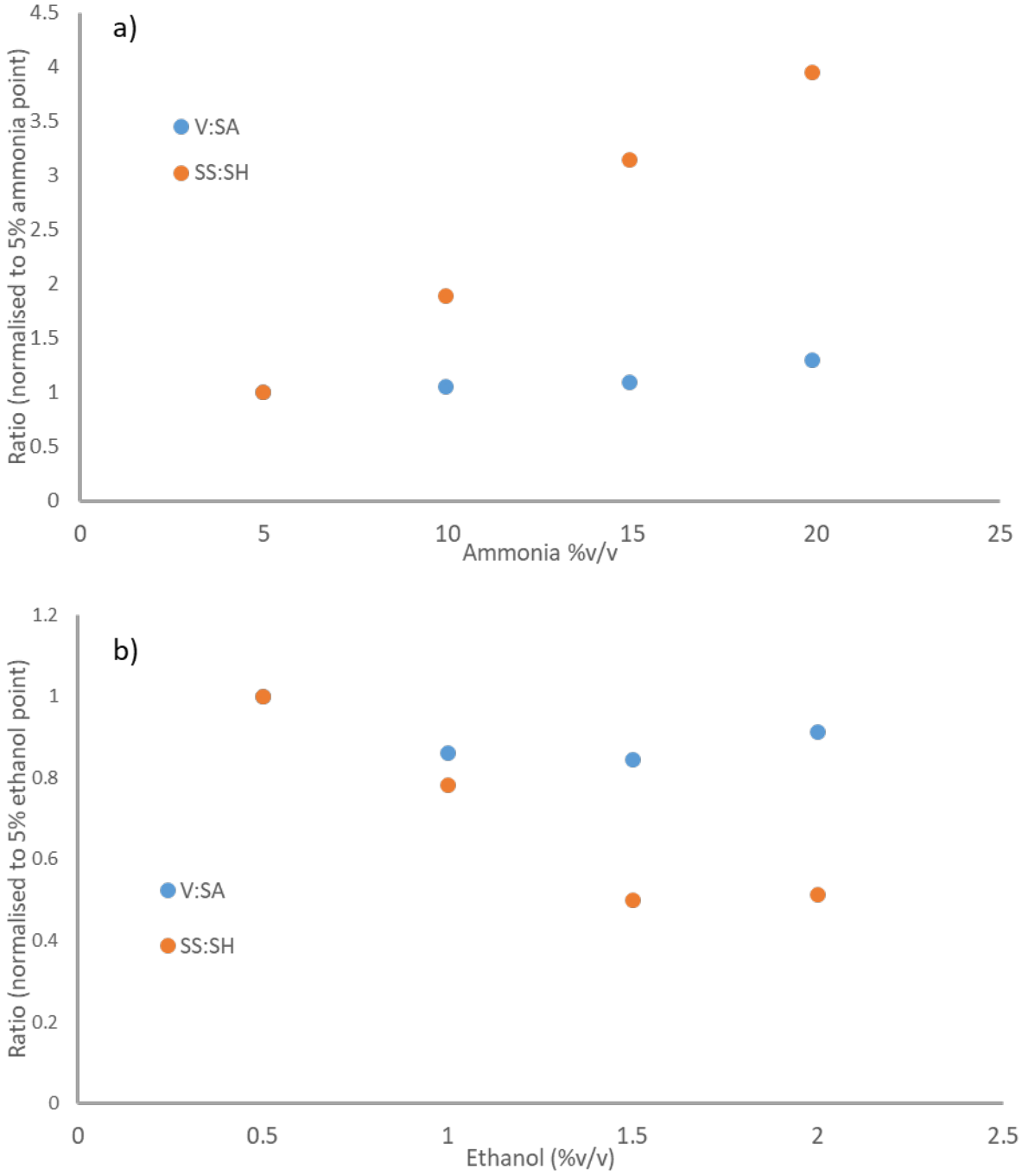

Figure 53: Comparisons of volume to surface area ratio (V:SA, in blue) and Disulphide:Thiol Raman peak ratio (SS:SH, in orange) for Method A with changes in a)ammonia concentration, b) ethanol concentration. All data points are normalised to the 5 %v/v data point.

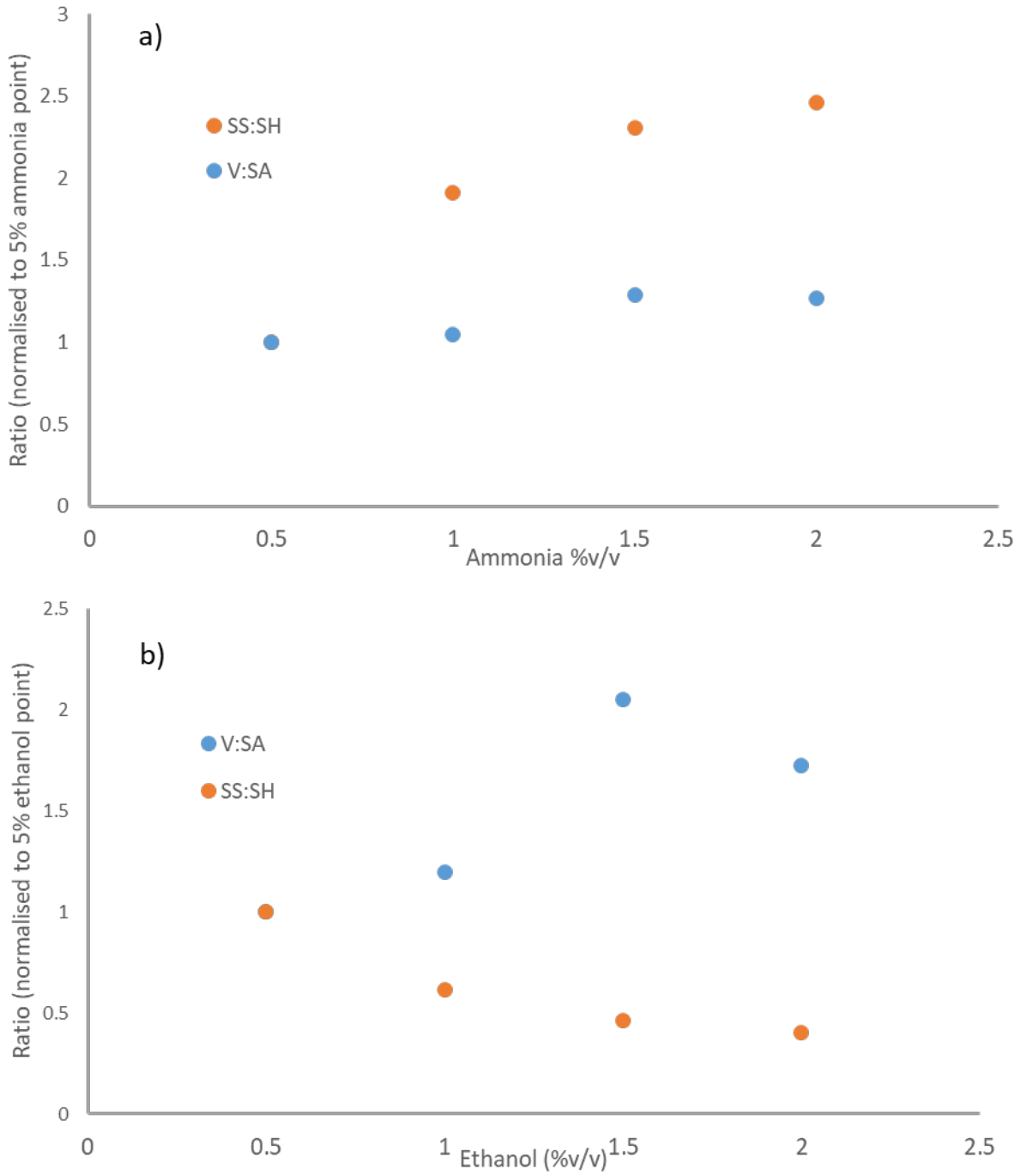

Figure 54: Comparisons of volume to surface area ratio (V:SA, in blue) and Disulphide:Thiol Raman peak ratio (SS:SH, in orange) for Method B with changes in a)ammonia concentration, b) ethanol concentration. All data points are normalised to the 5 %v/v data point.

A3: Example Theoretical Maximum Attachment Density Calculation

$Surface\ Area\ of\ large\ particle = SA = 4\pi r_l^2$

$r_l = 850\ nm$

$SA = 4\pi(850\ nm)^2$

$SA = 9.08 \times 10^6\ nm^2 = 9.08\ \mu m^2$

$Cross\ sectional\ area\ of\ small\ particle = A = \pi r_s^2$

$r_s = 99\ nm$

$A = \pi(99\ nm)^2$

$A = 3.08 \times 10^4\ nm^2$

$Highest\ possible\ packing\ density\ of\ circles = \eta = 0.907$

$Maximum\ surface\ area\ of\ the\ large\ partice\ which\ can\ be\ covered = SA_{max} = \eta SA$

$SA_{max} = (0.907)(9.08 \times 10^6\ nm^2)$

$SA_{max} = 8.23 \times 10^6\ nm^2$

$Number\ of\ small\ particles\ to\ give\ mazimum\ packing = N = \frac{SA_{max}}{A}$

$N = \frac{8.23 \times 10^6\ nm^2}{3.08 \times 10^4\ nm^2}$

$N = 267\ particles$

$Theoretical\ attachment\ density = \rho_A = \frac{N}{SA}$

$\rho_A = \frac{267\ particles}{9.08\ \mu m^2}$

$\rho_A = 29.5\ particles/\mu m^2$

A4: Water Contact Angle Images

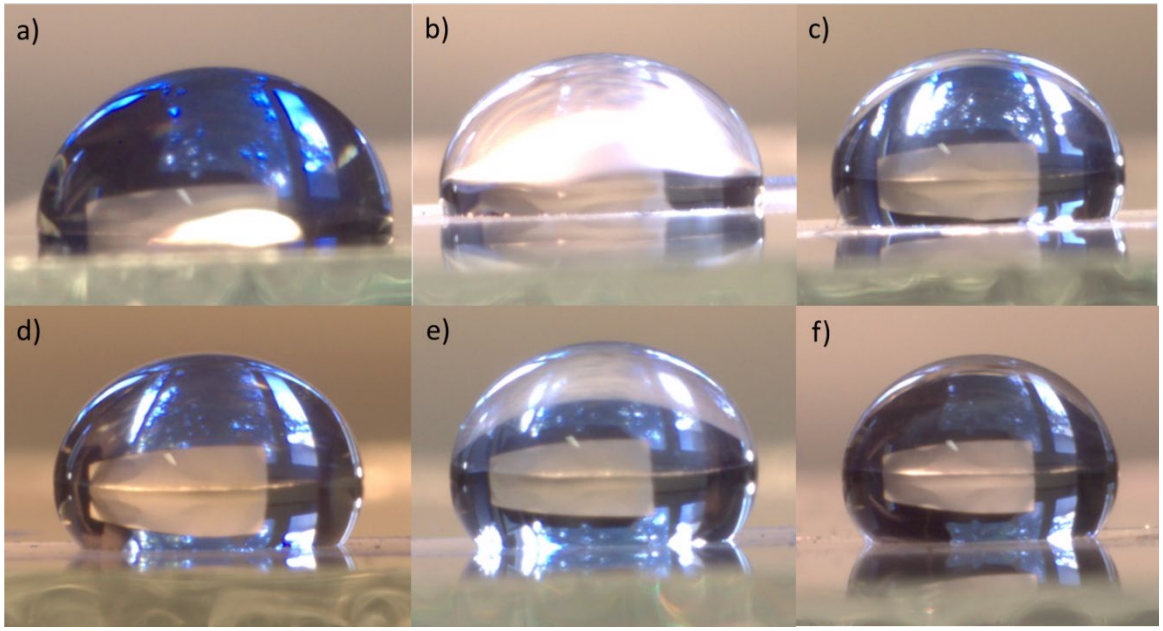

Figure 55: Water contact angle of raspberry/PDMS coatings with particle:polymer ratios of a)0:1, b) 0.5:1, c) 1:1, d) 1.5:1, e) 2.4:1, f) 3:1.

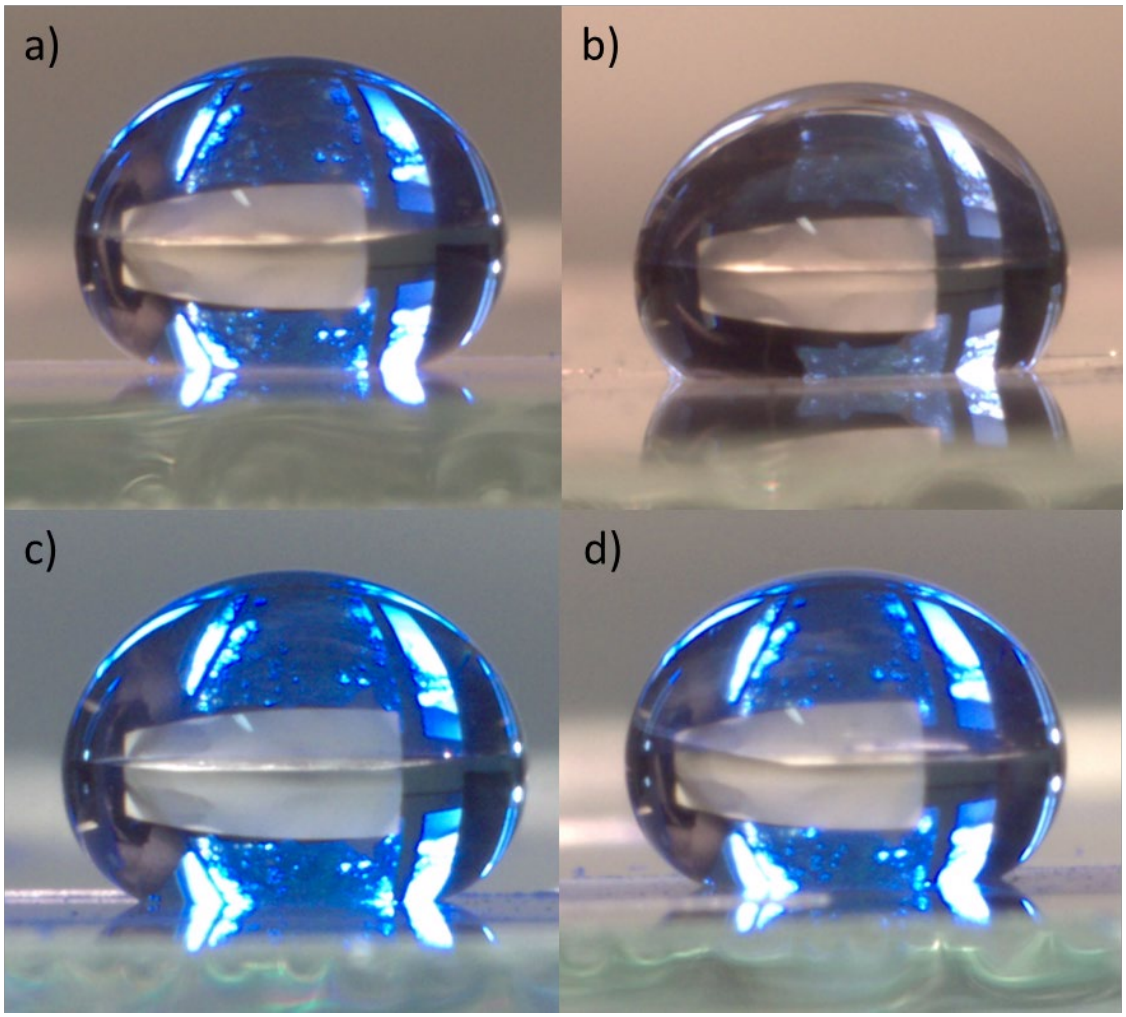

Figure 56: Water contact angle images for raspberry/PDMS coatings with small:large particle size ratios of a) 0.45:1, b) 0.066:1, c) 0.101:1, d) 0.108:1.

Chapter 8: References

1 Douma, M. *Opal*, <http://www.webexhibits.org/causesofcolor/15F.html> (2008).

2 Darragh, P. J., Gaskin, A. J., Terrell, B. C. & Sanders, J. V. Origin of Precious Opal. *Nature* **209**, 13, doi:10.1038/209013a0 (1966).

3 Choo, S., Choi, H.-J. & Lee, H. Replication of rose-petal surface structure using UV-nanoimprint lithography. *Materials Letters* **121**, 170-173, doi:10.1016/j.matlet.2014.01.037 (2014).

4 Erbil, H. Y., Demirel, A. L., Avci, Y. & Mert, O. Transformation of a Simple Plastic into a Superhydrophobic Surface. *Science* **299**, 1377-1380, doi:10.1126/science.1078365 (2003).

5 Fu, K. *et al.* All-Organic Superhydrophobic Coating Comprising Raspberry-Like Particles and Fluorinated Polyurethane Prepared via Thiol-Click Reaction. *Macromol Rapid Commun* **43**, e2100599-n/a, doi:10.1002/marc.202100599 (2022).

6 Guldin, S. *et al.* Self-cleaning antireflective optical coatings. *Nano letters* **13**, 5329-5335, doi:10.1021/nl402832u (2013).

7 Guo, F., Wen, Q., Peng, Y. & Guo, Z. Multifunctional hollow superhydrophobic SiO2 microspheres with robust and self-cleaning and separation of oil/water emulsions properties. *J Colloid Interface Sci* **494**, 54-63, doi:10.1016/j.jcis.2017.01.070 (2017).

8 Jiang, W., Grozea, C. M., Shi, Z. & Liu, G. Fluorinated Raspberry-like Polymer Particles for Superamphiphobic Coatings. *ACS Appl. Mater. Interfaces* **6**, 2629-2638, doi:10.1021/am4051074 (2014).

9 Li, Z., Wu, C., Zhao, K., Peng, B. & Deng, Z. Polydopamine-assisted synthesis of raspberry-like nanocomposite particles for superhydrophobic and superoleophilic surfaces. *Colloids and Surfaces A: Physicochemical and Engineering Aspects* **470**, 80-91, doi:10.1016/j.colsurfa.2015.01.067 (2015).

10 Liu, S., Latthe, S. S., Yang, H., Liu, B. & Xing, R. Raspberry-like superhydrophobic silica coatings with self-cleaning properties. *Ceramics international* **41**, 11719-11725, doi:10.1016/j.ceramint.2015.05.137 (2015).

11 Lu, Y. *et al.* Robust self-cleaning surfaces that function when exposed to either air or oil. *Science* **347**, 1132-1135, doi:10.1126/science.aaa0946 (2015).

12 Martin, S. & Bhushan, B. Transparent, wear-resistant, superhydrophobic and superoleophobic poly(dimethylsiloxane) (PDMS) surfaces. *J Colloid Interface Sci* **488**, 118-126, doi:10.1016/j.jcis.2016.10.094 (2017).

13 Ming, W., Wu, D., van Benthem, R. & de With, G. Superhydrophobic films from raspberry-like particles. *Nano letters* **5**, 2298-2301, doi:10.1021/nl0517363 (2005).

14 Pakdel, E., Daoud, W. A. & Wang, X. Self-cleaning and superhydrophilic wool by TiO2/SiO2 nanocomposite. *Applied Surface Science* **275**, 397-402, doi:10.1016/j.apsusc.2012.10.141 (2013).

15 Qian, Z., Zhang, Z., Song, L. & Liu, H. A novel approach to raspberry-like particles for superhydrophobic materials. *Journal of materials chemistry* **19**, 1297-1304, doi:10.1039/b810808k (2009).

16 Shang, B., Wang, Y., Peng, B. & Deng, Z. Bioinspired polydopamine particles-assisted construction of superhydrophobic surfaces for oil/water separation. *J Colloid Interface Sci* **482**, 240-251, doi:10.1016/j.jcis.2016.07.081 (2016).

17 Shang, Q., Wang, M., Liu, H., Gao, L. & Xiao, G. Facile fabrication of superhydrophobic raspberry-like SIO2/polystyrene composite particles. *Polym Compos* **34**, 51-57, doi:10.1002/pc.22376 (2013).
18 Swerin, A., Sundin, M. & Wåhlander, M. One-pot waterborne superhydrophobic pigment coatings at high solids with improved scratch and water resistance. *Colloids and Surfaces A: Physicochemical and Engineering Aspects* **495**, 79-86, doi:10.1016/j.colsurfa.2016.01.058 (2016).
19 Telford, A. M., Easton, C. D., Hawkett, B. S. & Neto, C. Waterborne, all-polymeric, colloidal 'raspberry' particles with controllable hydrophobicity and water droplet adhesion properties. *Thin Solid Films* **603**, 69-74, doi:10.1016/j.tsf.2016.01.052 (2016).
20 Telford, A. M., Hawkett, B. S., Such, C. & Neto, C. Mimicking the Wettability of the Rose Petal using Self-assembly of Waterborne Polymer Particles. *Chemistry of Materials* **25**, 3472-3479, doi:10.1021/cm4016386 (2013).
21 Tung, W. S. & Daoud, W. A. Self-cleaning fibers via nanotechnology: a virtual reality. *Journal of Materials Chemistry* **21**, 7858, doi:10.1039/c0jm03856c (2011).
22 Wang, C., Tang, F., Li, Q., Zhang, Y. & Wang, X. Spray-coated superhydrophobic surfaces with wear-resistance, drag-reduction and anti-corrosion properties. *Colloids and Surfaces A: Physicochemical and Engineering Aspects* **514**, 236-242, doi:10.1016/j.colsurfa.2016.11.059 (2017).
23 Wisdom, K. M. *et al.* Self-cleaning of superhydrophobic surfaces by self-propelled jumping condensate. *Proc Natl Acad Sci U S A* **110**, 7992-7997, doi:10.1073/pnas.1210770110 (2013).
24 Xu, D., Wang, M., Ge, X., Hon-Wah Lam, M. & Ge, X. Fabrication of raspberry SiO2/polystyrene particles and superhydrophobic particulate film with high adhesive force. *Journal of Materials Chemistry* **22**, 5784, doi:10.1039/c2jm15364e (2012).
25 Xu, L., Jin, H., Wu, D., Liu, B. & Zhang, M. Superhydrophobic polystyrene coating based on phase separation of raspberry structure particle. *Colloid and Polymer Science* **299**, 1695-1702, doi:10.1007/s00396-021-04891-w (2021).
26 Ye, Z., Chen, Y., Yang, X., Hu, W. & Ye, H. Development of perfluoropolyether modified raspberry paticles with fine hierarchical structure and their application in superhydrophobic surface. *Colloids and Surfaces A: Physicochemical and Engineering Aspects* **514**, 251-259, doi:10.1016/j.colsurfa.2016.11.063 (2017).
27 Zhang, L., Li, L. & Dang, Z. M. Bio-inspired durable, superhydrophobic magnetic particles for oil/water separation. *J Colloid Interface Sci* **463**, 266-271, doi:10.1016/j.jcis.2015.10.065 (2016).
28 Patra, J. K. *et al.* Nano based drug delivery systems: recent developments and future prospects. *Journal of Nanobiotechnology* **16**, 71, doi:10.1186/s12951-018-0392-8 (2018).
29 Colvin, V. L. From Opals to Optics: Colloidal Photonic Crystals. *MRS Bulletin* **26**, 637-641, doi:10.1557/mrs2001.159 (2011).
30 Cong, H., Yu, B., Tang, J., Li, Z. & Liu, X. Current status and future developments in preparation and application of colloidal crystals. *Chem. Soc. Rev.* **42**, 7774-7800, doi:10.1039/c3cs60078e (2013).
31 Fu, F. *et al.* Bio-inspired self-healing structural color hydrogel. *Proceedings of the National Academy of Sciences of the United States of America* **114**, 5900, doi:10.1073/pnas.1703616114 (2017).
32 Gao, W., Rigout, M. & Owens, H. Facile control of silica nanoparticles using a novel solvent varying method for the fabrication of artificial opal photonic crystals. *An Interdisciplinary Forum for Nanoscale Science and Technology* **18**, 1-10, doi:10.1007/s11051-016-3691-8 (2016).
33 Gao, W., Rigout, M. & Owens, H. The structural coloration of textile materials using self-assembled silica nanoparticles. *An Interdisciplinary Forum for Nanoscale Science and Technology* **19**, 1-11, doi:10.1007/s11051-017-3991-7 (2017).

34 Hoppe, C. E., Galante, M. J., Oyanguren, P. A. & Williams, R. J. J. Optical properties of novel thermally switched PDLC films composed of a liquid crystal distributed in a thermoplastic/thermoset polymer blend. *Materials Science and Engineering: C* **24**, 591-594, doi:10.1016/j.msec.2004.08.002 (2004).
35 Jiang, P., Bertone, J. F., Hwang, K. S. & Colvin, V. L. Single-crystal colloidal multilayers of controlled thickness. *Chemistry of Materials* **11**, 2132-2140, doi:10.1021/cm990080+ (1999).
36 Kalinin, D. V., Serdobintseva, V. V. & Shabanov, V. F. A new method for building photonic-crystal opal films by stacking monodisperse spherical silica particles into a regular structure in a surfactant medium. *Nanotechnologies in Russia* **4**, 359-365, doi:10.1134/s1995078009050140 (2009).
37 Lee, H., Shim, T., Hwang, H., Yang, S. M. & Kim, S. Colloidal Photonic Crystals toward Structural Color Palettes for Security Materials. *Chem. Mat.* **25**, 2684-2690, doi:10.1021/cm4012603 (2013).
38 Li, Y. *et al.* Biomimetic Surfaces for High-Performance Optics. *Advanced Materials* **21**, 4731-4734, doi:10.1002/adma.200901335 (2009).
39 Liljeström, V., Chen, C., Dommersnes, P., Fossum, J. O. & Gröschel, A. H. Active structuring of colloids through field-driven self-assembly. *Current opinion in colloid & interface science* **40**, 25-41, doi:10.1016/j.cocis.2018.10.008 (2019).
40 Lim, C. H., Kang, H. & Kim, S. H. Colloidal assembly in Leidenfrost drops for noniridescent structural color pigments. *Langmuir* **30**, 8350-8356, doi:10.1021/la502157p (2014).
41 Moroz, A. Photonic crystals of coated metallic spheres. *Europhysics letters* **50**, 466-472, doi:10.1209/epl/i2000-00292-4 (2000).
42 Mulderig, A. *et al.* Structural Emergence in Particle Dispersions. *Langmuir* **33**, 14029-14037, doi:10.1021/acs.langmuir.7b03033 (2017).
43 Nakamura, H. & Ishii, M. Effects of medium composition on optical properties and microstructures of non-close-packed colloidal crystalline arrays. *Kolloid-Zeitschrift und Zeitschrift für Polymere* **285**, 833-837, doi:10.1007/s00396-006-1618-0 (2007).
44 Nakamura, H. & Ishii, M. Optical properties of colloidal crystalline arrays composed of hollow polystyrene spheres. *Journal of Applied Polymer Science* **103**, 2364-2368, doi:10.1002/app.25234 (2007).
45 Ruhl, T., Spahn, P. & Hellmann, G. P. Artificial opals prepared by melt compression. *Polymer* **44**, 7625-7634, doi:10.1016/j.polymer.2003.09.047 (2003).
46 Serdobintseva, V., Kalinin, D. & Sobolev, N. Liophilization of the surface of monodisperse spherical silica particles and synthesis of opal photon-crystalline structures from liophile suspensions. *Doklady Earth Sciences* **417**, 1224-1227, doi:10.1134/S1028334X0708020X (2007).
47 Smolyaninov, I. I. Critical opalescence in hyperbolic metamaterials. *Journal of Optics* **13**, doi:10.1088/2040-8978/13/12/125101 (2011).
48 Spahn, P. *et al.* Modification of the refractive-index contrast in polymer opal films. *Journal of Materials Chemistry* **21**, 8893-8897, doi:10.1039/C1JM00063B (2011).
49 Takeoka, Y. *et al.* Structural Coloration of a Colloidal Amorphous Array is Intensified by Carbon Nanolayers. *Langmuir* **34**, 4282-4288, doi:10.1021/acs.langmuir.8b00242 (2018).
50 Trofimova, E. Y. *et al.* Monodisperse spherical mesoporous silica particles: fast synthesis procedure and fabrication of photonic-crystal films. *Nanotechnology* **24**, 155601, doi:10.1088/0957-4484/24/15/155601 (2013).
51 Wang, F., Gou, Z., Ge, Y. & An, K. Preparation of tunable structural colour film by coating PS with titania on glass. *Micro & Nano Letters* **11**, 50-53, doi:10.1049/mnl.2015.0264 (2016).
52 Yi, B. & Shen, H. Structurally colored films with superhydrophobicity and wide viewing angles based on bumpy melanin-like particles. *Applied Surface Science* **427**, 1129-1136, doi:10.1016/j.apsusc.2017.09.091 (2018).

53 Ying, Y. & Foulger, S. H. Color characteristics of mechanochromic photonic bandgap composites. *Sensors and Actuators B: Chemical* **137**, 574-577, doi:10.1016/j.snb.2008.12.061 (2009).
54 Yurii, A. V., Xiang-Zheng, B., James, C. S. & David, J. N. On-chip natural assembly of silicon photonic bandgap crystals. *Nature* **414**, 289, doi:10.1038/35104529 (2001).
55 Zhang, Y. *et al.* Preferential self-assembly behavior of polydisperse silica particles under negative pressure. *Colloids and Surfaces A: Physicochemical and Engineering Aspects* **529**, 832-839, doi:10.1016/j.colsurfa.2017.06.042 (2017).
56 Beltran-Osuna, A. A. *et al.* New antifouling silica hydrogel. *Langmuir* **28**, 9700-9706, doi:10.1021/la301561j (2012).
57 Mamaghani, M. Y., Pishvaei, M. & Kaffashi, B. Synthesis of latex based antibacterial acrylate polymer/nanosilver via in situ miniemulsion polymerization. *Macromolecular research* **19**, 243-249, doi:10.1007/s13233-011-0307-0 (2011).
58 Haruta, M. Size- and support-dependency in the catalysis of gold. *Catalysis today* **36**, 153-166, doi:10.1016/S0920-5861(96)00208-8 (1997).
59 Lee, K. Y. *et al.* One-step fabrication of gold nanoparticles-silica composites with enhanced catalytic activity. *Chemical physics letters* **453**, 77-81, doi:10.1016/j.cplett.2008.01.017 (2008).
60 Shi, H., Xu, N., Zhao, D. & Xu, B.-Q. Immobilized PVA-stabilized gold nanoparticles on silica show an unusual selectivity in the hydrogenation of cinnamaldehyde. *Catalysis communications* **9**, 1949-1954, doi:10.1016/j.catcom.2008.03.025 (2008).
61 Zidki, T., Cohen, H., Meyerstein, D. & Meisel, D. Effect of Silica-Supported Silver Nanoparticles on the Dihydrogen Yields from Irradiated Aqueous Solutions. *J. Phys. Chem. C* **111**, 10461-10466, doi:10.1021/jp070984f (2007).
62 Zobl, S., Salvenmoser, W., Schwerte, T., Gebeshuber, I. C. & Schreiner, M. Morpho peleides butterfly wing imprints as structural colour stamp. *Bioinspiration and Biomimetics* **11**, 2-17, doi:10.1088/1748-3190/11/1/016006

10.1088/1748-3190/11/3/039601 (2016).
63 Becker, E. W., Ehrfeld, W., Hagmann, P., Maner, A. & Münchmeyer, D. Fabrication of microstructures with high aspect ratios and great structural heights by synchrotron radiation lithography, galvanoforming, and plastic moulding (LIGA process). *Microelectronic Engineering* **4**, 35-56, doi:https://doi.org/10.1016/0167-9317(86)90004-3 (1986).
64 Bernardeschi, I., Ilyas, M. & Beccai, L. A Review on Active 3D Microstructures via Direct Laser Lithography. *Advanced intelligent systems* **3**, 2100051-n/a, doi:10.1002/aisy.202100051 (2021).
65 Jiang, G., Baig, S. & Wang, M. R. Prism-assisted inclined UV lithography for 3D microstructure fabrication. *J. Micromech. Microeng* **22**, 85022-85028, doi:10.1088/0960-1317/22/8/085022 (2012).
66 Kang, M., Byun, J. H., Na, S. & Jeon, N. L. Fabrication of functional 3D multi-level microstructures on transparent substrates by one step back-side UV photolithography. *RSC advances* **7**, 13353-13361, doi:10.1039/c6ra28812j (2017).
67 Rezaei, M., Jiang, H. & Kaminska, B. Structural colour printing from a reusable generic nanosubstrate masked for the target image. *Nanotechnology* **27**, 1-7, doi:10.1088/0957-4484/27/8/085301

10.1088/0957-4484/27/17/179502 (2016).
68 LaFratta, C. N., Li, L. & Fourkas, J. T. Soft-lithographic replication of 3D microstructures with closed loops. *Proceedings of the National Academy of Sciences* **103**, 8589-8594, doi:doi:10.1073/pnas.0603247103 (2006).
69 Gleason, K. K. Nanoscale control by chemically vapour-deposited polymers. *Nature Reviews Physics* **2**, 347-364, doi:10.1038/s42254-020-0192-6 (2020).

70 Chen, K., Shi, L., Zhang, Y. & Liu, Z. Scalable chemical-vapour-deposition growth of three-dimensional graphene materials towards energy-related applications. *Chem Soc Rev* **47**, 318-336, doi:10.1039/c7cs00852j (2018).
71 Landon, P. B. & Glosser, R. Self-assembly of spherical colloidal silica along the [100] direction of the FCC lattice and geometric control of crystallite formation. *J Colloid Interface Sci* **276**, 92-96, doi:10.1016/j.jcis.2004.01.021 (2004).
72 Liu, C., Li, Y.-J., Wang, M.-H., He, Y. & Yeung, E. S. Rapid fabrication of large-area nanoparticle monolayer films via water-induced interfacial assembly. *Nanotechnology* **20**, 065604, doi:10.1088/0957-4484/20/6/065604 (2009).
73 Lu, H.-Y., Teng, C.-L., Kung, C.-H. & Wan, B.-Z. Preparing Mesoporous Low-kFilms with High Mechanical Strength from Noncrystalline Silica Particles. *Industrial & Engineering Chemistry Research* **50**, 3265-3273, doi:10.1021/ie1018436 (2011).
74 Larson-Smith, K., Jackson, A. & Pozzo, D. C. Small angle scattering model for Pickering emulsions and raspberry particles. *J Colloid Interface Sci* **343**, 36-41, doi:10.1016/j.jcis.2009.11.033 (2010).
75 Minami, H., Mizuta, Y. & Suzuki, T. Preparation of Raspberry-like Polymer Particles by a Heterocoagulation Technique Utilizing Hydrogen Bonding Interactions between Steric Stabilizers. *Langmuir* **29**, 554-560, doi:10.1021/la3043507 (2012).
76 Puretskiy, N. & Ionov, L. Synthesis of robust raspberry-like particles using polymer brushes. *Langmuir* **27**, 3006-3011, doi:10.1021/la104614t (2011).
77 Song, T., Liu, T., Yang, X. & Bai, F. Raspberry-like particles via the heterocoagulated reaction between reactive epoxy and amino groups. *Colloids and Surfaces A: Physicochemical and Engineering Aspects* **469**, 60-65, doi:10.1016/j.colsurfa.2015.01.016 (2015).
78 Wang, L. *et al.* Role of surface functionality on the formation of raspberry-like polymer/silica composite particles: Weak acid–base interaction and steric effect. *Applied Surface Science* **342**, 92-100, doi:10.1016/j.apsusc.2015.03.042 (2015).
79 Shirman, E. *et al.* Modular Design of Advanced Catalytic Materials Using Hybrid Organic-Inorganic Raspberry Particles. *Advanced Functional Materials*, 1704559, doi:10.1002/adfm.201704559 (2017).
80 García-Soto, M. J. & González-Ortega, O. Synthesis of silica-core gold nanoshells and some modifications/variations. *Gold bulletin (World Gold Council)* **49**, 111-131, doi:10.1007/s13404-016-0188-2 (2016).
81 Kumari, P., Rickard, H. & Majewski, P. Deposition of silver and gold nanoparticles on surface engineered silica particles and their potential applications. *J Nanosci Nanotechnol* **12**, 8001-8007, doi:10.1166/jnn.2012.6655 (2012).
82 Graf, C. & van Blaaderen, A. Metallodielectric Colloidal Core−Shell Particles for Photonic Applications. *Langmuir* **18**, 524-534, doi:10.1021/la011093g (2002).
83 Lim, Y. T., Park, O. O. & Jung, H.-T. Gold nanolayer-encapsulated silica particles synthesized by surface seeding and shell growing method: near infrared responsive materials. *J Colloid Interface Sci* **263**, 449-453, doi:10.1016/S0021-9797(03)00322-9 (2003).
84 Oldenburg, S. J., Averitt, R. D., Westcott, S. L. & Halas, N. J. Nanoengineering of optical resonances. *Chemical physics letters* **288**, 243-247, doi:10.1016/S0009-2614(98)00277-2 (1998).
85 Otoufi, M. K., Shahtahmasebebi, N., Kompany, A. & Goharshadi, E. A systematic growth of Gold nanoseeds on Silica for Silica@Gold core-shell nanoparticles and investigation of optical properties. *International journal of nano dimension* **5**, 525 (2014).
86 Radloff, C., Vaia, R. A., Brunton, J., Bouwer, G. T. & Ward, V. K. Metal Nanoshell Assembly on a Virus Bioscaffold. *Nano Lett* **5**, 1187-1191, doi:10.1021/nl050658g (2005).
87 Badia, A., Lennox, R. B. & Reven, L. A Dynamic View of Self-Assembled Monolayers. *Acc. Chem. Res* **33**, 475-481, doi:10.1021/ar9702841 (2000).

88 Kumar, A., Biebuyck, H. A. & Whitesides, G. M. Patterning Self-Assembled Monolayers: Applications in Materials Science. *Langmuir* **10**, 1498-1511, doi:10.1021/la00017a030 (1994).
89 Love, J. C., Estroff, L. A., Kriebel, J. K., Nuzzo, R. G. & Whitesides, G. M. Self-Assembled Monolayers of Thiolates on Metals as a Form of Nanotechnology. *Chem. Rev* **105**, 1103-1170, doi:10.1021/cr0300789 (2005).
90 Schreiber, F. Structure and growth of self-assembling monolayers. *Progress in surface science* **65**, 151-257, doi:10.1016/S0079-6816(00)00024-1 (2000).
91 Smith, R. K., Lewis, P. A. & Weiss, P. S. Patterning self-assembled monolayers. *Progress in Surface Science* **75**, 1-68, doi:10.1016/j.progsurf.2003.12.001 (2004).
92 Ulman, A. Formation and Structure of Self-Assembled Monolayers. *Chem. Rev* **96**, 1533-1554, doi:10.1021/cr9502357 (1996).
93 Wink, T., Van Zuilen, S. J., Bult, A. & Van Bennekom, W. P. Self-assembled monolayers for biosensors. *Analyst* **122**, R43-R50, doi:10.1039/a606964i (1997).
94 Abbott, N. L., Folkers, J. P. & Whitesides, G. M. Manipulation of the Wettability of Surfaces on the 0.1 to 1-Micrometer Scale Through Micromachining and Molecular Self-Assembly. *Science* **257**, 1380-1382, doi:10.1126/science.257.5075.1380 (1992).
95 Xu, Z., Song, K., Yuan, S.-L. & Liu, C.-B. Microscopic Wetting of Self-Assembled Monolayers with Different Surfaces: A Combined Molecular Dynamics and Quantum Mechanics Study. *Langmuir* **27**, 8611-8620, doi:10.1021/la201328y (2011).
96 Harris, J. K., Brothers, M., Ratcliff, E. L., St. Lawrence, M. & Kim, S. Self-Assembled Monolayers for Anti-Fouling and Highly Selective Electrode Interfaces. *Meeting abstracts (Electrochemical Society)* **MA2020-01**, 2420-2420, doi:10.1149/MA2020-01352420mtgabs (2020).
97 Ostuni, E. *et al.* Self-Assembled Monolayers That Resist the Adsorption of Proteins and the Adhesion of Bacterial and Mammalian Cells. *Langmuir* **17**, 6336-6343, doi:10.1021/la010552a (2001).
98 Chaki, N. K. & Vijayamohanan, K. Self-assembled monolayers as a tunable platform for biosensor applications. *Biosens Bioelectron* **17**, 1-12, doi:10.1016/S0956-5663(01)00277-9 (2002).
99 Calestani, D. in *Exposure to Engineered Nanomaterials in the Environment* (eds Nelson Marmiroli, Jason C. White, & Jing Song) 31-57 (Elsevier, 2019).
100 Vollath, D., Fischer, F. D. & Holec, D. Surface energy of nanoparticles - influence of particle size and structure. *Beilstein J Nanotechnol* **9**, 2265-2276, doi:10.3762/bjnano.9.211 (2018).
101 Yu, X. H. *et al.* Surface Tension and Surface Energy of Nanomaterials. *Journal of Computational and Theoretical Nanoscience* **12**, 5318-5322, doi:10.1166/jctn.2015.4522 (2015).
102 Heneghan, A. F., Justin Moore, H., Randall Lee, T. & Haymet, A. D. J. Statistics of heterogeneous nucleation of supercooled aqueous solutions in a self-assembled monolayer-coated container. *Chemical physics letters* **385**, 441-445, doi:10.1016/j.cplett.2004.01.025 (2004).
103 Yantasee, W., Lin, Y., Fryxell, G. E. & Busche, B. J. Simultaneous detection of cadmium, copper, and lead using a carbon paste electrode modified with carbamoylphosphonic acid self-assembled monolayer on mesoporous silica (SAMMS). *Analytica chimica acta* **502**, 207-212, doi:10.1016/j.aca.2003.10.001 (2004).
104 Das, A. K., Kilty , H. P., Marto, P. J., Andeen, G. B. & Kumar, A. The Use of an Organic Self-Assembled Monolayer Coating to Promote Dropwise Condensation of Steam on Horizontal Tubes. *Journal of Heat Transfer* **122**, 278-286, doi:10.1115/1.521465 (1999).
105 Shakiba, A., Zenasni, O., D. Marquez, M. & Randall Lee, T. Advanced drug delivery via self-assembled monolayer-coated nanoparticles. *AIMS bioengineering* **4**, 275-299, doi:10.3934/bioeng.2017.2.275 (2017).

106 Taguchi, T., Isozaki, K. & Miki, K. Enhanced Catalytic Activity of Self-Assembled-Monolayer-Capped Gold Nanoparticles. *Adv. Mater* **24**, 6462-6467, doi:10.1002/adma.201202979 (2012).
107 Holec, D., Dumitraschkewitz, P., Vollath, D. & Fischer, F. D. Surface Energy of Au Nanoparticles Depending on Their Size and Shape. *Nanomaterials (Basel)* **10**, 484, doi:10.3390/nano10030484 (2020).
108 Polte, J. Fundamental growth principles of colloidal metal nanoparticles – a new perspective. *CrystEngComm* **17**, 6809-6830, doi:10.1039/C5CE01014D (2015).
109 Yao, Y., Wei, Y. & Chen, S. Size effect of the surface energy density of nanoparticles. *Surface science* **636**, 19-24, doi:10.1016/j.susc.2015.01.016 (2015).
110 Astruc, D. Introduction: Nanoparticles in Catalysis. *Chem. Rev* **120**, 461-463, doi:10.1021/acs.chemrev.8b00696 (2020).
111 Sarmah, M. *et al.* Effect of Substrates on Catalytic Activity of Biogenic Palladium Nanoparticles in C–C Cross-Coupling Reactions. *ACS Omega* **4**, 3329-3340, doi:10.1021/acsomega.8b02697 (2019).
112 Huang, W. *et al.* Highly Active Heterogeneous Palladium Nanoparticle Catalysts for Homogeneous Electrophilic Reactions in Solution and the Utilization of a Continuous Flow Reactor. *J. Am. Chem. Soc* **132**, 16771-16773, doi:10.1021/ja108898t (2010).
113 Obermayer, D. *et al.* Nanocatalysis in continuous flow: supported iron oxide nanoparticles for the heterogeneous aerobic oxidation of benzyl alcohol. *Green chemistry : an international journal and green chemistry resource : GC* **15**, 1530-1537, doi:10.1039/c3gc40307f (2013).
114 Guo, X.-C. & Dong, P. Multistep Coating of Thick Titania Layers on Monodisperse Silica Nanospheres. *Langmuir* **15**, 5535-5540, doi:10.1021/la990220u (1999).
115 Wang, W., Gu, B. & Liang, L. Effect of anionic surfactants on synthesis and self-assembly of silica colloidal nanoparticles. *J Colloid Interface Sci* **313**, 169-173, doi:10.1016/j.jcis.2007.04.042 (2007).
116 Dust Repellent Surface Coating. United States patent (2010).
117 Hamence, S. *The Use of Surfactand-Growth Silica Particles in Dust Repellent Coatings* (Flinders University, 2021).
118 Toster, J. & Lewis, D. Investigation of Roughness Periodicity on the Hydrophobic Properties of Surfaces*. *Australian Journal of Chemistry* **68**, 1228-1232, doi:https://doi.org/10.1071/CH15310 (2015).
119 Langer, J. *et al.* Present and Future of Surface-Enhanced Raman Scattering. *ACS Nano* **14**, 28-117, doi:10.1021/acsnano.9b04224 (2020).
120 Szaniawska, A. & Kudelski, A. Applications of Surface-Enhanced Raman Scattering in Biochemical and Medical Analysis. *Frontiers in Chemistry* **9**, doi:10.3389/fchem.2021.664134 (2021).
121 Ghimire, P. P. & Jaroniec, M. Renaissance of Stöber method for synthesis of colloidal particles: New developments and opportunities. *J Colloid Interface Sci* **584**, 838-865, doi:10.1016/j.jcis.2020.10.014 (2021).
122 Glover, B. J. & Whitney, H. M. Structural colour and iridescence in plants: the poorly studied relations of pigment colour. *Annals of botany* **105**, 505-511, doi:10.1093/aob/mcq007 (2010).
123 Vigneron, J. P. & Simonis, P. Natural Photonic Crystals. *Physica B* **407**, 4032-4036, doi:10.1016/j.physb.2011.12.130 (2012).
124 Nakamura, H., Ishii, M., Tsukigase, A., Harada, M. & Nakano, H. Close-packed colloidal crystalline arrays composed of silica spheres coated with titania. *Langmuir* **22**, 1268-1272, doi:10.1021/la052034w (2006).

125 Huang, H. *et al.* Facile synthesis of silica–titania core–shell microsphere and their optical transmission spectra. *Materials Letters* **110**, 260-263, doi:10.1016/j.matlet.2013.08.027 (2013).
126 Jiang, Y. *et al.* Electrothermally driven structural colour based on liquid crystal elastomers. *Journal of Materials Chemistry* **22**, 11943, doi:10.1039/c2jm30176h (2012).
127 Joannopoulos, J. D., Johnson, S. G., Winn, J. N. & Meade, R. D. *Photonic Crystals: Molding the Flow of Light*. 2 edn, (Princeton University Press, 2008).
128 Biró, L. P. & Vigneron, J. P. Photonic nanoarchitectures in butterflies and beetles: valuable sources for bioinspiration. *Laser & Photonics Reviews* **5**, 27-51, doi:10.1002/lpor.200900018 (2011).
129 Dechkrong, P. *et al.* Fine structure of wing scales of butterflies, Euploea mulciber and Troides aeacus. *J Struct Biol* **176**, 75-82, doi:10.1016/j.jsb.2011.07.006 (2011).
130 Didari, A. & Mengüç, M. P. A biomimicry design for nanoscale radiative cooling applications inspired by Morpho didius butterfly. *Scientific reports* **8**, 16891-16891, doi:10.1038/s41598-018-35082-3 (2018).
131 Han, Z.-w., Wu, L.-y., Qiu, Z.-m., Guan, H.-y. & Ren, L.-q. Structural colour in butterfly apatura ilia scales and the microstructure simulation of photonic crystal. *J. of Bionic Engineering Suppl.* **27**, 14-19 (2008).
132 Kinoshita, S., Yoshioka, S. & Kawagoe, K. Mechanisms of structural colour in the Morpho butterfly: Cooperation of regularity and irregularity in an iridescent scale. *Proceedings of the Royal Society B: Biological Sciences* **269**, 1417-1421, doi:10.1098/rspb.2002.2019 (2002).
133 Parker, A. R. & Martini, N. Structural colour in animals—simple to complex optics. *Optics & Laser Technology* **38**, 315-322, doi:10.1016/j.optlastec.2005.06.037 (2006).
134 Srinivasarao, M. Nano-optics in the biological world: Beetles, butterflies, birds, and moths. *Chem. Rev.* **99**, 1935-1961, doi:10.1021/cr970080y (1999).
135 Vukusic, P. Photonic structures in biology. *Nature* **424**, 852-855, doi:10.1038/nature01941 (2003).
136 Vignolini, S. *et al.* Structural colour from helicoidal cell-wall architecture in fruits of Margaritaria nobilis. *J R Soc Interface* **13**, doi:10.1098/rsif.2016.0645 (2016).
137 Vignolini, S. *et al.* Is floral iridescence a biologically relevant cue in plant-pollinator signalling. A response to van der Kooi *et al.* (2014b). *New Phytol* **205**, 205 (2015).
138 Vignolini, S. *et al.* The flower of Hibiscus trionum is both visibly and measurably iridescent. *New Phytol* **205**, 97-101, doi:10.1111/nph.12958 (2015).
139 Wang, F., Zhang, X., Zhu, J. & Lin, Y. Preparation of structurally colored films assembled by using polystyrene@silica, air@silica and air@carbon@silica coreshell nanoparticles with enhanced color visibility. *RSC Adv.* **6**, 37535-37543, doi:10.1039/c5ra25680a (2016).
140 Vignolini, S. *et al.* Pointillist structural color in Pollia fruit. *PNAS* **109**, 15712-15715, doi:10.1073/pnas.1210105109

10.1073/pnas.1210105109/-/DCSupplemental (2012).
141 Demirörs, A. F., van Blaaderen, A. & Imhof, A. Synthesis of Eccentric Titania−Silica Core−Shell and Composite Particles. *Chemistry of Materials* **21**, 979-984, doi:10.1021/cm803250w (2009).
142 Kalele, S. *et al.* Synthesis and characterization of silica—titania core—shell particles. *Pramana* **65**, 787-791, doi:10.1007/BF02704076 (2005).
143 Kamaruddin, S. & Stephan, D. The preparation of silica–titania core–shell particles and their impact as an alternative material to pure nano-titania photocatalysts. *Catalysis Today* **161**, 53-58, doi:https://doi.org/10.1016/j.cattod.2010.10.038 (2011).
144 Lim, S. H., Phonthammachai, N., Pramana, S. S. & White, T. J. Simple Route to Monodispersed Silica−Titania Core−Shell Photocatalysts. *Langmuir* **24**, 6226-6231, doi:10.1021/la703899j (2008).

145 Pang, S. C., Kho, S. Y. & Chin, S. F. Fabrication of Magnetite/Silica/Titania Core-Shell Nanoparticles. *Journal of Nanomaterials* **2012**, 6, doi:10.1155/2012/427310 (2012).
146 Viravathana, P. & Marr, D. W. M. Optical Trapping of Titania/Silica Core-Shell Colloidal Particles. *J Colloid Interface Sci* **221**, 301-307, doi:https://doi.org/10.1006/jcis.1999.6603 (2000).
147 Tao, G. *et al.* Digital design of multimaterial photonic particles. *Proceedings of the National Academy of Sciences of the United States of America* **113**, 6839, doi:10.1073/pnas.1601777113 (2016).
148 Zhao, Z.-B., Zhang, D.-M., Meng, Y.-F., Tai, L. & Jiang, Y. One-pot fabrication of fluoride-silica@silica raspberry-like nanoparticles for superhydrophobic coating. *Ceramics International* **42**, 14601-14608, doi:10.1016/j.ceramint.2016.06.076 (2016).
149 Tian, L. *et al.* Generalized Approach for Fabricating Monodisperse Anisotropic Microparticles via Single-Hole Swelling PGMA Seed Particles. *Macromolecules* **48**, 7592-7603, doi:10.1021/acs.macromol.5b01319 (2015).
150 Kurdyukov, D. A., Eurov, D. A., Kirilenko, D. A., Sokolov, V. V. & Golubev, V. G. Tailoring the size and microporosity of Stöber silica particles. *Microporous and mesoporous materials* **258**, 205-210, doi:10.1016/j.micromeso.2017.09.017 (2018).
151 Baba, E. M., Cansoy, C. E. & Zayim, E. O. Investigation of wettability and optical properties of superhydrophobic polystyrene-SiO2 composite surfaces. *Progress in organic coatings* **99**, 378-385, doi:10.1016/j.porgcoat.2016.06.016 (2016).
152 Balmer, J. A. *et al.* Packing Efficiency of Small Silica Particles on Large Latex Particles: A Facile Route to Colloidal Nanocomposites. *Langmuir* **25**, 5339-5347, doi:10.1021/la8041555 (2009).
153 Zou, H. & Wang, X. Adsorption of Silica Nanoparticles onto Poly(N-vinylpyrrolidone)-Functionalized Polystyrene Latex. *Langmuir* **33**, 1471-1477, doi:10.1021/acs.langmuir.6b03977 (2017).
154 Li, X. & He, J. In situ Assembly of Raspberry- and Mulberry-like Silica Nanospheres toward Antireflective and Antifogging Coatings. *ACS applied materials & interfaces* **4**, 2204-2211, doi:10.1021/am3002082 (2012).
155 Yang, J. *et al.* A novel method to fabricate superhydrophobic surfaces based on well-defined mulberry-like particles and self-assembly of polydimethylsiloxane. *Applied surface science* **255**, 3507-3512, doi:10.1016/j.apsusc.2008.09.092 (2009).
156 Pastoriza-Santos, I., Gomez, D., Perez-Juste, J., Liz-Marzan, L. M. & Mulvaney, P. Optical properties of metal nanoparticle coated silica spheres: a simple effective medium approach. *Physical chemistry chemical physics : PCCP* **6**, 5056-5060, doi:10.1039/B405157B (2004).
157 Caruso, F., Spasova, M., Salgueiriño-Maceira, V. & Liz-Marzán, L. M. Multilayer Assemblies of Silica-Encapsulated Gold Nanoparticles on Decomposable Colloid Templates. *Adv. Mater* **13**, 1090-1094, doi:10.1002/1521-4095(200107)13:14<1090::AID-ADMA1090>3.0.CO;2-H (2001).
158 Kim, J.-H. *et al.* Gold, Palladium, and Gold−Palladium Alloy Nanoshells on Silica Nanoparticle Cores. *ACS Appl. Mater. Interfaces* **1**, 1063-1069, doi:10.1021/am900039a (2009).
159 Pol, V. G., Gedanken, A. & Calderon-Moreno, J. Deposition of Gold Nanoparticles on Silica Spheres: A Sonochemical Approach. *Chem. Mater* **15**, 1111-1118, doi:10.1021/cm021013+ (2003).
160 Revina, A. A., Potapov, V. V., Baranova, E. K. & Smirnov, Y. V. Studying the interaction between silica nanoparticles and metals by spectrophotometry. *Russian Journal of Physical Chemistry A* **87**, 257-264, doi:10.1134/S0036024413020258 (2013).
161 Behme, N., Hintersatz, H., Tegenkamp, C. & Goedel, W. A. Preparation of microsieves with a hierarchical structure via float-casting, using raspberry particles. *Journal of membrane science* **642**, 119941, doi:10.1016/j.memsci.2021.119941 (2022).

162 Zhang, L., Li, Z., Jing, J., Ding, H. & Chen, Z. DTT–Au NCs Interact with DNA to Form Raspberry-Like Particles. *Particle & particle systems characterization* **36**, 1800517-n/a, doi:10.1002/ppsc.201800517 (2019).
163 Ashayer, R., Mannan, S. H. & Sajjadi, S. Synthesis and characterization of gold nanoshells using poly(diallyldimethyl ammonium chloride). *Colloids and surfaces. A, Physicochemical and engineering aspects* **329**, 134-141, doi:10.1016/j.colsurfa.2008.07.004 (2008).
164 Babaei, M. *et al.* Synthesis of theranostic epithelial cell adhesion molecule targeted mesoporous silica nanoparticle with gold gatekeeper for hepatocellular carcinoma. *Nanomedicine (Lond)* **12**, 1261-1279, doi:10.2217/nnm-2017-0028 (2017).
165 Kandpal, D., Kalele, S. & Kulkarni, S. K. Synthesis and characterization of silica-gold core-shell (SiO2@Au) nanoparticles. *Pramana* **69**, 277-283, doi:10.1007/s12043-007-0128-z (2007).
166 Kim, J.-H., Bryan, W. W. & Randall Lee, T. Preparation, Characterization, and Optical Properties of Gold, Silver, and Gold−Silver Alloy Nanoshells Having Silica Cores. *Langmuir* **24**, 11147-11152, doi:10.1021/la8016497 (2008).
167 Kim, L. n. *et al.* Fabrication and Manipulation of Gold 1D Chain Assemblies Using Magnetically Controllable Gold Nanoparticles. *Bulletin of the Korean Chemical Society* **33**, 3735-3739, doi:10.5012/bkcs.2012.33.11.3735 (2012).
168 Li, X., Li, J. & Jiang, L. A silica-gold core-shell structure to mimic the large size of gold particles for promoting cell growth: A comparative study of the silica core size and the nanogold amount in the shell. *Colloids and surfaces. A, Physicochemical and engineering aspects* **459**, 211-216, doi:10.1016/j.colsurfa.2014.07.013 (2014).
169 Otoufi, M. K., Shahtahmasebi, N., Kompany, A., Goharshadi, E. K. & Roghani, A. Gradual Growth of Gold Nanoseeds on Silica for Silica@Gold Core–Shell Nano Applications by Two Different Methods: A Comparison on Structural Properties. *Journal of cluster science* **25**, 1307-1317, doi:10.1007/s10876-014-0709-1 (2014).
170 Rezvani Nikabadi, H., Shahtahmasebi, N., Rezaee Rokn-Abadi, M., Bagheri Mohagheghi, M. M. & Goharshadi, E. K. Gradual growth of gold nanoseeds on silica for SiO2@gold homogeneous nano core/shell applications by the chemical reduction method. *Phys. Scr* **87**, 25802, doi:10.1088/0031-8949/87/02/025802 (2013).
171 Sadtler, B. & Wei, A. Spherical ensembles of gold nanoparticles on silica: electrostatic and size effects. *Chem Commun (Camb)*, 1604-1605, doi:10.1039/b204760h (2002).
172 Solga, A., Cerman, Z., Striffler, B. F., Spaeth, M. & Barthlott, W. The dream of staying clean: Lotus and biomimetic surfaces. *Bioinspir Biomim* **2**, S126-S134, doi:10.1088/1748-3182/2/4/S02 (2007).
173 Ebert, D. & Bhushan, B. Durable Lotus-effect surfaces with hierarchical structure using micro- and nanosized hydrophobic silica particles. *J Colloid Interface Sci* **368**, 584-591, doi:10.1016/j.jcis.2011.09.049 (2012).
174 Ji, H. *et al.* Biomimetic Superhydrophobic Surfaces. *Journal of Dispersion Science and Technology* **34**, 1-21, doi:10.1080/01932691.2011.646625 (2013).
175 Yuan, Y. & Lee, T. R. 3-34 (Berlin, Heidelberg: Springer Berlin Heidelberg).
176 Zhang, M., Feng, S., Wang, L. & Zheng, Y. Lotus effect in wetting and self-cleaning. *Biotribology (Oxford)* **5**, 31-43, doi:10.1016/j.biotri.2015.08.002 (2016).
177 Hans, J. E., Petra, D.-K., Christoph, N. & Wilhelm, B. Superhydrophobicity in perfection: the outstanding properties of the lotus leaf. *Beilstein Journal of Nanotechnology* **2**, 152-161, doi:10.3762/bjnano.2.19 (2011).
178 Marmur, A. Wetting on Hydrophobic Rough Surfaces: To Be Heterogeneous or Not To Be? *Langmuir* **19**, 8343-8348, doi:10.1021/la0344682 (2003).
179 Patankar, N. A. Mimicking the Lotus Effect: Influence of Double Roughness Structures and Slender Pillars. *Langmuir* **20**, 8209-8213, doi:10.1021/la048629t (2004).
180 Bormashenko, E. Wetting transitions on biomimetic surfaces. *Philos Trans A Math Phys Eng Sci* **368**, 4695-4711, doi:10.1098/rsta.2010.0121 (2010).

181 Gao, N. & Yan, Y. Characterisation of surface wettability based on nanoparticles. *Nanoscale* **4**, 222-2218, doi:10.1039/c2nr11736c (2012).
182 Abid, N. *et al.* Synthesis of nanomaterials using various top-down and bottom-up approaches, influencing factors, advantages, and disadvantages: A review. *Adv Colloid Interface Sci* **300**, 102597-102597, doi:10.1016/j.cis.2021.102597 (2022).
183 Wu, K.-J., Tse, E. C. M., Shang, C. & Guo, Z. Nucleation and growth in solution synthesis of nanostructures – From fundamentals to advanced applications. *Progress in materials science* **123**, 100821, doi:10.1016/j.pmatsci.2021.100821 (2022).
184 Thanh, N. T. K., Maclean, N. & Mahiddine, S. Mechanisms of Nucleation and Growth of Nanoparticles in Solution. *Chem. Rev* **114**, 7610-7630, doi:10.1021/cr400544s (2014).
185 Whitehead, C. B., Özkar, S. & Finke, R. G. LaMer's 1950 model of particle formation: a review and critical analysis of its classical nucleation and fluctuation theory basis, of competing models and mechanisms for phase-changes and particle formation, and then of its application to silver halide, semiconductor, metal, and metal-oxide nanoparticles. *Materials advances* **2**, 186-235, doi:10.1039/d0ma00439a (2021).
186 LaMer, V. K. & Dinegar, R. H. Theory, Production and Mechanism of Formation of Monodispersed Hydrosols. *J. Am. Chem. Soc* **72**, 4847-4854, doi:10.1021/ja01167a001 (1950).
187 Reiss, H. The growth of uniform colloidal dispersions. *The Journal of chemical physics* **19**, 482-487, doi:10.1063/1.1748251 (1951).
188 Yao, Y. *et al.* Microconfinement from Dendronized Chitosan Oligosaccharides for Mild Synthesis of Silver Nanoparticles. *ACS Appl. Nano Mater* **5**, 4350-4359, doi:10.1021/acsanm.2c00119 (2022).
189 Yong, J. M. *et al.* ROS-Mediated Anti-Angiogenic Activity of Cerium Oxide Nanoparticles in Melanoma Cells. *ACS Biomater. Sci. Eng* **8**, 512-525, doi:10.1021/acsbiomaterials.1c01268 (2022).
190 Arshadi, S., Moghaddam, J. & Eskandarian, M. LaMer diagram approach to study the nucleation and growth of Cu2O nanoparticles using supersaturation theory. *The Korean journal of chemical engineering* **31**, 2020-2026, doi:10.1007/s11814-014-0130-3 (2014).
191 Vreeland, E. C. *et al.* Enhanced Nanoparticle Size Control by Extending LaMer's Mechanism. *Chem. Mater* **27**, 6059-6066, doi:10.1021/acs.chemmater.5b02510 (2015).
192 Anton, N., Benoit, J.-P. & Saulnier, P. Design and production of nanoparticles formulated from nano-emulsion templates—A review. *J Control Release* **128**, 185-199, doi:10.1016/j.jconrel.2008.02.007 (2008).
193 Jenjob, R., Phakkeeree, T., Seidi, F., Theerasilp, M. & Crespy, D. Emulsion Techniques for the Production of Pharmacological Nanoparticles. *Macromol Biosci* **19**, e1900063-n/a, doi:10.1002/mabi.201900063 (2019).
194 Hassam, C. *High-concentration nanofluids prepared from functionalised silica nanoparticles: synthesis optimisation and investigation of rheological properties* Nanotechnology thesis, (2019).
195 Mangos, D. N., Nakanishi, T. & Lewis, D. A. A simple method for the quantification of molecular decorations on silica particles. *Science and Technology of Advanced Materials* **15**, doi:10.1088/1468-6996/15/1/015002 (2014).
196 McDonough, R. *Silica Nanoparticles as a Platform for Intelligent Cofactor Immobilisation for Biosynthetic Applications* Nanotechnology thesis, Flinders University, (2020).
197 Stacey, K. *The Role of Scale in the Production of Biomimetic Coatings* Nanotechnology thesis, Flinders University, (2017).
198 Nakamura, M. & Ishimura, K. One-pot synthesis and characterization of three kinds of thiol-organosilica nanoparticles. *Langmuir* **24**, 5099-5108, doi:10.1021/la703395w (2008).
199 Jenjob, R., Seidi, F. & Crespy, D. Recent advances in polymerizations in dispersed media. *Adv Colloid Interface Sci* **260**, 24-31, doi:10.1016/j.cis.2018.08.002 (2018).

200 Qi, D.-m., Bao, Y.-z., Weng, Z.-x. & Huang, Z.-m. Preparation of acrylate polymer/silica nanocomposite particles with high silica encapsulation efficiency via miniemulsion polymerization. *Polymer (Guilford)* **47**, 4622-4629, doi:10.1016/j.polymer.2006.04.024 (2006).
201 Chern, C.-S. *Principles and applications of emulsion polymerization*. 1st edn, (Hoboken: Wiley, 2008).
202 American Chemical Society. Meeting Chicago, I. *Polymerization and polycondensation processes: a collection of papers based on the Symposium on Polymerization and Polycondensation Processes*. Vol. 34 (Washington, DC: American Chemical Society, 1962).
203 Grant, R. L., Yao, C., Gabaldon, D. & Acosta, D. EVALUATION OF SURFACTANT CYTOTOXICITY POTENTIAL BY PRIMARY CULTURES OF OCULAR-TISSUES .1. CHARACTERIZATION OF RABBIT CORNEAL EPITHELIAL-CELLS AND INITIAL INJURY AND DELAYED TOXICITY STUDIES. *Toxicology (Amsterdam)* **76**, 153-176, doi:10.1016/0300-483X(92)90162-8 (1992).
204 Inácio, Â. S. *et al.* In vitro surfactant structure-toxicity relationships: Implications for surfactant use in sexually transmitted infection prophylaxis and contraception. *PLoS One* **6**, e19850, doi:10.1371/journal.pone.0019850 (2011).
205 Nagarajan, R. & Ruckenstein, E. Molecular Theory of Microemulsions. *Langmuir* **16**, 6400-6415, doi:10.1021/la991578t (2000).
206 Amato, D. V., Amato, D. N., Flynt, A. S. & Patton, D. L. Functional, sub-100 nm polymer nanoparticles via thiol-ene miniemulsion photopolymerization. *Polymer chemistry* **6**, 5625-5632, doi:10.1039/c4py01449a (2015).
207 Behzadi, S. *et al.* A triblock terpolymer: Vs. blends of diblock copolymers for nanocapsules addressed by three independent stimuli. *Polymer chemistry* **7**, 3434-3443, doi:10.1039/c6py00344c (2016).
208 Crespy, D. & Landfester, K. Miniemulsion polymerization as a versatile tool for the synthesis of functionalized polymers. *Beilstein J Org Chem* **6**, 1132-1148, doi:10.3762/bjoc.6.130 (2010).
209 Crespy, D. & Landfester, K. Making dry fertile: a practical tour of non-aqueous emulsions and miniemulsions, their preparation and some applications. *Soft matter* **7**, 1154-1164, doi:10.1039/c1sm06156a (2011).
210 Schaeffel, D. *et al.* Fluorescence Correlation Spectroscopy Directly Monitors Coalescence During Nanoparticle Preparation. *Nano Lett* **12**, 6012-6017, doi:10.1021/nl303581q (2012).
211 Bohlender, C., Landfester, K., Crespy, D. & Schiller, A. Unconventional Non-Aqueous Emulsions for the Encapsulation of a Phototriggerable NO-Donor Complex in Polymer Nanoparticles. *Particle Particle Systems Characterization* **30**, 138-142, doi:10.1002/ppsc.201200067 (2013).
212 Desgouilles, S. *et al.* The Design of Nanoparticles Obtained by Solvent Evaporation: A Comprehensive Study. *Langmuir* **19**, 9504-9510, doi:10.1021/la034999q (2003).
213 Staff, R. H., Landfester, K. & Crespy, D. Hierarchical Macromolecular Structures: 60 Years after the Staudinger Nobel Prize II. *Hierarchical Macromolecular Structures: 60 Years after the Staudinger Nobel Prize II* (2013).
214 Chaudhary, S., Rohilla, D. & Mehta, S. K. Surfactant adsorption and aggregate structure of silica nanoparticles: a versatile stratagem for the regulation of particle size and surface modification. *Materials Research Express* **1**, 1-17, doi:10.1088/2053-1591/1/1/015011 (2014).
215 Gholami, T., Salavati-Niasari, M., Bazarganipour, M. & Noori, E. Synthesis and characterization of spherical silica nanoparticles by modified Stöber process assisted by organic ligand. *Superlattices and microstructures* **61**, 33-41, doi:10.1016/j.spmi.2013.06.004 (2013).

216 Rahman, I. A. & Padavettan, V. Synthesis of Silica nanoparticles by Sol-Gel: Size- dependent properties, surface modification, and applications in silica- polymer nanocompositesa review. *Journal of Nanomaterials* **2012**, doi:10.1155/2012/132424 (2012).
217 Stöber, W., Fink, A. & Bohn, E. Controlled growth of monodisperse silica spheres in the micron size range. *J Colloid Interface Sci* **26**, 62-69, doi:https://doi.org/10.1016/0021-9797(68)90272-5 (1968).
218 Doura, T., Tamanoi, F. & Nakamura, M. Miniaturization of thiol-organosilica nanoparticles induced by an anionic surfactant. *J Colloid Interface Sci* **526**, 51-62, doi:10.1016/j.jcis.2018.04.090 (2018).
219 Wang, W., Gu, B. & Liang, L. Effect of Surfactants on the Formation, Morphology, and Surface Property of Synthesized SiO 2 Nanoparticles. *Journal of Dispersion Science and Technology* **25**, 593-601, doi:10.1081/DIS-200027309 (2005).
220 Fernandes, R. S., Raimundo, I. M. & Pimentel, M. F. Revising the synthesis of Stöber silica nanoparticles: A multivariate assessment study on the effects of reaction parameters on the particle size. *Colloids and surfaces. A, Physicochemical and engineering aspects* **577**, 1-7, doi:10.1016/j.colsurfa.2019.05.053 (2019).
221 Greasley, S. L. *et al.* Controlling particle size in the Stöber process and incorporation of calcium. *J Colloid Interface Sci* **469**, 213-223, doi:10.1016/j.jcis.2016.01.065 (2016).
222 Sun, X. L. *et al.* Superhydrophobicity of silica nanoparticles modified with polystyrene. *Applied Surface Science* **257**, 2308-2312, doi:10.1016/j.apsusc.2010.09.094 (2011).
223 Zhao, Z. B., Zhang, D. M., Meng, Y. F., Tai, L. & Jiang, Y. One-pot fabrication of fluoride-silica@silica raspberry-like nanoparticles for superhydrophobic coating. *Ceramics International* **42**, 14601-14608, doi:10.1016/j.ceramint.2016.06.076 (2016).
224 Schubert, U. *Synthesis of inorganic materials*. 2nd, rev. and updated ed. edn, (Weinheim ; Great Britain : Wiley-VCH, 2005).
225 Chen, S. L., Dong, P., Yang, G. H. & Yang, J. J. Kinetics of formation of monodisperse colloidal silica particles through the hydrolysis and condensation of tetraethyorthosilicate. *Industrial and Engineering Chemistry Research* **35**, 4487-4493, doi:10.1021/ie9602217 (1996).
226 Han, Y. *et al.* Unraveling the Growth Mechanism of Silica Particles in the Stöber Method: In Situ Seeded Growth Model. *Langmuir* **33**, 5879-5890, doi:10.1021/acs.langmuir.7b01140 (2017).
227 Ibrahim, I. A. M., Zikry, A. A. F. & Sharaf, M. A. Preparation of spherical silica nanoparticles: Stober silica. *Journal of American Science* **6**, 985-989, doi:10.7537/marsjas061110.133 (2010).
228 Razink, J. J. & Schlotter, N. E. Correction to "Preparation of monodisperse silica particles: Control of size and mass fraction" by G.H. Bogush, M.A. Tracy and C.F. Zukoski IV, Journal of Non-Crystalline Solids 104 (1988) 95–106. *Journal of Non-Crystalline Solids* **353**, 2932-2933, doi:10.1016/j.jnoncrysol.2007.06.067 (2007).
229 Nedeljko, P., Turel, M., Košak, A. & Lobnik, A. Synthesis of hybrid thiol-functionalized SiO 2 particles used for agmatine determination. *Journal of Sol-Gel Science and Technology* **79**, 487-496, doi:10.1007/s10971-016-4030-3 (2016).
230 Yuan, J., Zhou, S., Gu, G. & Wu, L. Effect of the particle size of nanosilica on the performance of epoxy/silica composite coatings. *Journal of Materials Science* **40**, 3927-3932, doi:10.1007/s10853-005-0714-8 (2005).
231 Liang, R. & Zou, H. Removal of aqueous Hg(ii) by thiol-functionalized nonporous silica microspheres prepared by one-step sol–gel method. *RSC Advances* **10**, 18534-18542, doi:10.1039/D0RA02759F (2020).
232 Arkhireeva, A. & Hay, J. N. Synthesis of sub-200 nm silsesquioxane particles using a modified Stöber sol-gel route. *Journal of Materials Chemistry* **13**, 3122-3127, doi:10.1039/b306994j (2003).

233 Nagappan, S. *et al.* Synthesis of size-controlled and highly monodispersed silica nanoparticles using a short alkyl-chain fluorinated surfactant. *RSC Adv* **11**, 2194-2221, doi:10.1039/d0ra08114k (2021).
234 Singh, L. P., Bhattacharyya, S. K., Mishra, G. & Ahalawat, S. Functional role of cationic surfactant to control the nano size of silica powder. *Applied nanoscience* **1**, 117-122, doi:10.1007/s13204-011-0016-1 (2011).
235 Alex, S. & Tiwari, A. Functionalized Gold Nanoparticles: Synthesis, Properties and Applications--A Review. *J Nanosci Nanotechnol* **15**, 1869-1894, doi:10.1166/jnn.2015.9718 (2015).
236 Turkevich, J., Stevenson, P. C. & Hillier, J. A study of the nucleation and growth processes in the synthesis of colloidal gold. *Discussions of the Faraday Society* **11**, 55-75, doi:10.1039/DF9511100055 (1951).
237 Chumanov, G., Sokolov, K., Gregory, B. W. & Cotton, T. M. Colloidal metal films as a substrate for surface-enhanced spectroscopy. *J. Phys. Chem* **99**, 9466-9471, doi:10.1021/j100023a025 (1995).
238 Connolly, D., Twamley, B. & Paull, B. High-capacity gold nanoparticle functionalised polymer monoliths. *Chem Commun (Camb)* **46**, 2109-2111, doi:10.1039/b924152c (2010).
239 Grabar, K. C. *et al.* Two-Dimensional Arrays of Colloidal Gold Particles: A Flexible Approach to Macroscopic Metal Surfaces. *Langmuir* **12**, 2353-2361, doi:10.1021/la950561h (1996).
240 Grabar, K. C., Freeman, R. G., Hommer, M. B. & Natan, M. J. Preparation and Characterization of Au Colloid Monolayers. *Anal. Chem* **67**, 735-743, doi:10.1021/ac00100a008 (1995).
241 Grabar, K. C. *et al.* Kinetic Control of Interparticle Spacing in Au Colloid-Based Surfaces: Rational Nanometer-Scale Architecture. *J. Am. Chem. Soc* **118**, 1148-1153, doi:10.1021/ja952233+ (1996).
242 Sato, T., Ahmed, H., Brown, D. & Johnson, B. F. G. Single electron transistor using a molecularly linked gold colloidal particle chain. *Journal of applied physics* **82**, 696-701, doi:10.1063/1.365600 (1997).
243 Sato, T., Brown, D. & Johnson, B. F. G. Nucleation and growth of nano-gold colloidal lattices. *Chemical communications (Cambridge, England)*, 1007-1008, doi:10.1039/a701627a (1997).
244 Westcott, S. L., Oldenburg, S. J., Lee, T. R. & Halas, N. J. Construction of simple gold nanoparticle aggregates with controlled plasmon–plasmon interactions. *Chemical physics letters* **300**, 651-655, doi:10.1016/S0009-2614(98)01410-9 (1999).
245 Frens, G. Controlled Nucleation for the Regulation of the Particle Size in Monodisperse Gold Suspensions. *Nature Physical Science* **241**, 20-22, doi:10.1038/physci241020a0 (1973).
246 Daniel, M.-C. & Astruc, D. Gold Nanoparticles: Assembly, Supramolecular Chemistry, Quantum-Size-Related Properties, and Applications toward Biology, Catalysis, and Nanotechnology. *Chemical Reviews* **104**, 293-346, doi:10.1021/cr030698+ (2004).
247 Deraedt, C. *et al.* Sodium borohydride stabilizes very active gold nanoparticle catalysts. *Chemical Communications* **50**, 14194-14196, doi:10.1039/C4CC05946H (2014).
248 Mehravani, B., Ribeiro, A. I. & Zille, A. Gold Nanoparticles Synthesis and Antimicrobial Effect on Fibrous Materials. *Nanomaterials* **11**, 1067 (2021).
249 Park, S.-E., Park, M.-Y., Han, P.-K. & Lee, S.-W. The Effect of pH-adjusted Gold Colloids on the Formation of Gold Clusters over APTMS-coated Silica Cores. *Bulletin of the Korean Chemical Society* **27**, 1341-1345, doi:10.5012/bkcs.2006.27.9.1341 (2006).
250 Ramesh, S., Kim, H. S., Lee, Y.-J., Hong, G.-W. & Kim, J.-H. Nanostructured Silica/Gold-Cellulose-Bonded Amino-POSS Hybrid Composite via Sol-Gel Process and Its Properties. *Nanoscale Res Lett* **12**, 381-381, doi:10.1186/s11671-017-2122-9 (2017).
251 Westcott, S. L., Oldenburg, S. J., Lee, T. R. & Halas, N. J. Formation and Adsorption of Clusters of Gold Nanoparticles onto Functionalized Silica Nanoparticle Surfaces. *Langmuir* **14**, 5396-5401, doi:10.1021/la980380q (1998).

252 Duff, D. G., Baiker, A. & Edwards, P. P. A new hydrosol of gold clusters. 1. Formation and particle size variation. *Langmuir* **9**, 2301-2309, doi:10.1021/la00033a010 (1993).
253 Song, Y., Huang, T. & Murray, R. W. Heterophase Ligand Exchange and Metal Transfer between Monolayer Protected Clusters. *J. Am. Chem. Soc* **125**, 11694-11701, doi:10.1021/ja0355731 (2003).
254 Templeton, A. C., Wuelfing, W. P. & Murray, R. W. Monolayer-Protected Cluster Molecules. *Acc. Chem. Res* **33**, 27-36, doi:10.1021/ar9602664 (2000).
255 De, S. & Khan, A. Efficient synthesis of multifunctional polymers via thiol-epoxy "click" chemistry. *Chemical communications (Cambridge, England)* **48**, 3130-3132, doi:10.1039/c2cc30434a (2012).
256 Hoyle, C. E., Lowe, A. B. & Bowman, C. N. Thiol- click chemistry: a multifaceted toolbox for small molecule and polymer synthesis. *Chemical Society Reviews* **39**, 1355-1387, doi:10.1039/b901979k (2010).
257 Nair, D. P. *et al.* The Thiol-Michael Addition Click Reaction: A Powerful and Widely Used Tool in Materials Chemistry. *Chemistry of Materials* **26**, 724-744, doi:10.1021/cm402180t (2014).
258 Li, J. *et al.* Preparation and Properties of SBS-g-GOs-Modified Asphalt Based on a Thiol-ene Click Reaction in a Bituminous Environment. *Polymers* **10**, doi:10.3390/polym10111264 (2018).
259 Ou, B. *et al.* Preparation of doubly responsive polymer functionalized silica hybrid nanoparticles via a one-pot thiol-isocyanate click reaction at room temperature. *Polymer composites* **38**, 1454-1461, doi:10.1002/pc.23713 (2017).
260 Cengiz, N., Rao, J., Sanyal, A. & Khan, A. Designing functionalizable hydrogels through thiolepoxy coupling chemistry. *Chem. Commun.* **49**, 11191-11193, doi:10.1039/c3cc45859h (2013).
261 Lin, H. *et al.* Thiol-epoxy click polymerization for preparation of polymeric monoliths with well-defined 3D framework for capillary liquid chromatography. *Analytical chemistry* **87**, 3476-3483, doi:10.1021/acs.analchem.5b00006 (2015).
262 Tucker-Schwartz, A. K., Farrell, R. A. & Garrell, R. L. Thiol-ene click reaction as a general route to functional trialkoxysilanes for surface coating applications. *Journal of the American Chemical Society* **133**, 11026-11029, doi:10.1021/ja202292q (2011).
263 Jin, K., Heath, W. H. & Torkelson, J. M. Kinetics of multifunctional thiol-epoxy click reactions studied by differential scanning calorimetry: Effects of catalysis and functionality. *Polymer* **81**, 70-78, doi:10.1016/j.polymer.2015.10.068 (2015).
264 Konuray, A. O., Fernández-Francos, X. & Ramis, X. Analysis of the reaction mechanism of the thiol-epoxy addition initiated by nucleophilic tertiary amines. *Polymer chemistry* **8**, 5934-5947, doi:10.1039/c7py01263b (2017).
265 Loureiro, R. M., Amarelo, T. C., Abuin, S. P., Soulé, E. R. & Williams, R. J. J. Kinetics of the epoxy–thiol click reaction initiated by a tertiary amine: Calorimetric study using monofunctional components. *Thermochimica Acta* **616**, 79-86, doi:10.1016/j.tca.2015.08.012 (2015).
266 Vernon-Parry, K. D. Scanning electron microscopy: an introduction. *III-Vs review* **13**, 40-44, doi:10.1016/S0961-1290(00)80006-X (2000).
267 Australia, M. *Scanning Electron Microscopy SEM Basics*, <https://myscope.training/#/SEMlevel_3_1> (
268 Malvern. Dynamic Light Scattering: An Introduction in 30 Minutes. *Technical Note*. <https://warwick.ac.uk/fac/cross_fac/sciencecity/programmes/internal/themes/am2/booking/particlesize/intro_to_dls.pdf>.
269 Parupudi, A., Mulagapati, S. H. R. & Subramony, J. A. 3-46 (Elsevier Inc, 2022).
270 Stetefeld, J., McKenna, S. A. & Patel, T. R. Dynamic light scattering: a practical guide and applications in biomedical sciences. *Biophys Rev* **8**, 409-427, doi:10.1007/s12551-016-0218-6 (2016).

271 Lim, J., Yeap, S. P., Che, H. X. & Low, S. C. Characterization of magnetic nanoparticle by dynamic light scattering. *Nanoscale Research Letters* **8**, 381, doi:10.1186/1556-276X-8-381 (2013).
272 Malvern. Zeta Potential - An introduction in 30 minutes. *Technical Note* (2015). <https://www.research.colostate.edu/wp-content/uploads/2018/11/ZetaPotential-Introduction-in-30min-Malvern.pdf>.
273 Tadros, T. *Encyclopedia of Colloid and Interface Science*. 1st 2013. edn, (Berlin, Heidelberg : Springer Berlin Heidelberg : Imprint: Springer, 2013).
274 Grover, R. B. G. *Ellman's assay for in-solution quantification of sulfhydryl groups*, <https://www.bmglabtech.com/ellmans-assay-for-in-solution-quantification-of-sulfhydryl-groups/> (2022).
275 LLC, E. N. *Ellman's Assay for Quantification of Free Sulfhydryls in Antibodies*, <https://encapsula.com/ellmans-assay-protocol-2/> (2019).
276 Aitken A, L. M. in *The Protein Protocols Handbook* (ed Walker J.M) (Humana Press, 2009).
277 Raja, P. M. V. & Barron, A. R. *4.4: UV-Visible Spectroscopy*, <https://chem.libretexts.org/Bookshelves/Analytical_Chemistry/Physical_Methods_in_Chemistry_and_Nano_Science_(Barron)/04%3A_Chemical_Speciation/4.04%3A_UV-Visible_Spectroscopy> (2021).
278 Elmer, P. FT-IR Spectroscopy: Attenuated Total Reflectance (ATR). *Technical Note* (2005). <https://cmdis.rpi.edu/sites/default/files/ATR_FTIR.pdf>.
279 Dietzek, B., Cialla, D., Schmitt, M. & Popp, J. in *Confocal Raman Microscopy* (eds Jan Toporski, Thomas Dieing, & Olaf Hollricher) 47-68 (Springer International Publishing, 2018).
280 Hollricher, O. in *Confocal Raman Microscopy* (eds Jan Toporski, Thomas Dieing, & Olaf Hollricher) 69-87 (Springer International Publishing, 2018).
281 Kakihana, M. & Osada, M. in *Carbon Alloys* (eds Ei-ichi Yasuda *et al.*) 285-298 (Elsevier Science, 2003).
282 Lee, K. S. *et al.* Raman microspectroscopy for microbiology. *Nature Reviews Methods Primers* **1**, 80, doi:10.1038/s43586-021-00075-6 (2021).
283 Toporski, J., Dieing, T. & Hollricher, O. *Confocal Raman Microscopy*. 2nd 2018. edn, (Cham : Springer International Publishing : Imprint: Springer, 2018).
284 Mthembu, S. N., Sharma, A., Albericio, F. & Torre, B. G. Breaking a Couple: Disulfide Reducing Agents. *Chembiochem.* **21**, 1947-1954, doi:10.1002/cbic.202000092

info:doi/10.1002/cbic.202000092 (2020).
285 Humphrey, R. E. & Potter, J. L. Reduction of Disulfides with Tributylphosphine. *Analytical chemistry.* **37**, 164-165, doi:10.1021/ac60220a049 (1965).
286 Mekaru, H., Yoshigoe, A., Nakamura, M., Doura, T. & Tamanoi, F. Biodegradability of Disulfide-Organosilica Nanoparticles Evaluated by Soft X-ray Photoelectron Spectroscopy: Cancer Therapy Implications. *ACS Appl. Nano Mater* **2**, 479-488, doi:10.1021/acsanm.8b02023 (2019).
287 Ladhe, A. R., Frailie, P., Hua, D., Darsillo, M. & Bhattacharyya, D. Thiol-functionalized silica–mixed matrix membranes for silver capture from aqueous solutions: Experimental results and modeling. *J Memb Sci* **326**, 460-471, doi:10.1016/j.memsci.2008.10.025 (2009).
288 Stolyarchuk, N. V. *et al.* Synthesis and sorption properties of bridged polysilsesquioxane microparticles containing 3-mercaptopropyl groups in the surface layer. *Colloids and surfaces. A, Physicochemical and engineering aspects* **538**, 694-702, doi:10.1016/j.colsurfa.2017.11.049 (2018).
289 Yu, Y., Addai-Mensah, J. & Losic, D. Functionalized diatom silica microparticles for removal of mercury ions. *Sci Technol Adv Mater* **13**, 015008-015008, doi:10.1088/1468-6996/13/1/015008 (2012).

290 Méndez, J., Monteagudo, A. & Griebenow, K. Stimulus-Responsive Controlled Release System by Covalent Immobilization of an Enzyme into Mesoporous Silica Nanoparticles. *Bioconjugate Chem* **23**, 698-704, doi:10.1021/bc200301a (2012).
291 Alswieleh, A. M. Modification of Mesoporous Silica Surface by Immobilization of Functional Groups for Controlled Drug Release. *Journal of chemistry* **2020**, 1-9, doi:10.1155/2020/9176257 (2020).
292 Ambrožić, G. *et al.* Building organosilica hybrid nanohemispheres via thiol-ene click reaction on alumina thin films deposited by atomic layer deposition (ALD). *J Colloid Interface Sci* **560**, 303-311, doi:10.1016/j.jcis.2019.10.074 (2020).
293 Nedeljko, P., Turel, M., Košak, A. & Lobnik, A. Synthesis of hybrid thiol-functionalized SiO2 particles used for agmatine determination. *Journal of sol-gel science and technology* **79**, 487-496, doi:10.1007/s10971-016-4030-3 (2016).
294 Nakamura, T., Yamada, Y. & Yano, K. Direct synthesis of monodispersed thiol-functionalized nanoporous silica spheres and their application to a colloidal crystal embedded with gold nanoparticles. *Journal of materials chemistry* **17**, 3726-3732, doi:10.1039/b705209j (2007).
295 Gaslain, F. O. M., Delacôte, C., Walcarius, A. & Lebeau, B. One-step preparation of thiol-modified mesoporous silica spheres with various functionalization levels and different pore structures. *Journal of sol-gel science and technology* **49**, 112-124, doi:10.1007/s10971-008-1845-6 (2009).
296 Hayashi, K., Maruhashi, T., Sakamoto, W. & Yogo, T. Organic–Inorganic Hybrid Hollow Nanoparticles Suppress Oxidative Stress and Repair Damaged Tissues for Treatment of Hepatic Fibrosis. *Advanced functional materials* **28**, 1706332-n/a, doi:10.1002/adfm.201706332 (2018).
297 Johari, K., Saman, N. & Mat, H. Synthesis and Characterization of Novel Sulfur-Functionalized Silica Gels as Mercury Adsorbents. *Journal of materials engineering and performance* **23**, 809-818, doi:10.1007/s11665-013-0813-7 (2014).
298 Melnyk, I. V. *et al.* Protection of thiol groups on the surface of magnetic adsorbents and their application for wastewater treatment. *Sci Rep* **8**, 8592-8513, doi:10.1038/s41598-018-26767-w (2018).
299 Al Mahrooqi, J. H., Mun, E. A., Williams, A. C. & Khutoryanskiy, V. V. Controlling the Size of Thiolated Organosilica Nanoparticles. *Langmuir* **34**, 8347-8354, doi:10.1021/acs.langmuir.8b01556 (2018).
300 Beaupre, D. M. & Weiss, R. G. Thiol-and disulfide-based stimulus-responsive soft materials and self-assembling systems. *Molecules (Basel, Switzerland)* **26**, 3332, doi:10.3390/molecules26113332 (2021).
301 Irmukhametova, G. S., Mun, G. A. & Khutoryanskiy, V. V. Thiolated Mucoadhesive and PEGylated Nonmucoadhesive Organosilica Nanoparticles from 3-Mercaptopropyltrimethoxysilane. *Langmuir* **27**, 9551-9556, doi:10.1021/la201385h (2011).
302 Lin-Vien, D., Colthup, N. B., Fateley, W. G. & Grasselli, J. G. in *The Handbook of Infrared and Raman Characteristic Frequencies of Organic Molecules* (eds Daimay Lin-Vien, Norman B. Colthup, William G. Fateley, & Jeanette G. Grasselli) 225-250 (Academic Press, 1991).
303 Lin-Vien, D., Colthup, N. B., Fateley, W. G. & Grasselli, J. G. in *The Handbook of Infrared and Raman Characteristic Frequencies of Organic Molecules* (eds Daimay Lin-Vien, Norman B. Colthup, William G. Fateley, & Jeanette G. Grasselli) 251-261 (Academic Press, 1991).
304 Bastian, E. J. & Martin, R. B. Disulfide vibrational spectra in the sulfur-sulfur and carbon-sulfur stretching region. *The Journal of Physical Chemistry* **77**, 1129-1133, doi:10.1021/j100628a010 (1973).
305 Reid, E. E. *Organic Chemistry of Bivalent Sulfur*. (Chemical Publishing Co Inc, 1958).
306 Wallace, T. J. & Schriesheim, A. Solvent Effects in the Base-Catalyzed Oxidation of Mercaptans with Molecular Oxygen1. *The Journal of Organic Chemistry* **27**, 1514-1516, doi:10.1021/jo01052a005 (1962).

307 Shchukarev, S. A. & Tolmacheva, T. A. Solubility of oxygen in ethanol - Water mixtures. *Journal of structural chemistry* **9**, 16-21, doi:10.1007/BF00744018 (1968).
308 Lan, Y., Liu, J., Eiser, E. & Scherman, O. A. Polymeric raspberry-like particles via template-assisted polymerisation. *Polymer chemistry* **10**, 3772-3777, doi:10.1039/C9PY00484J (2019).
309 Stauch, C. *et al.* Colloidal Core–Satellite Supraparticles via Preprogramed Burst of Nanostructured Micro-Raspberry Particles. *Particle & particle systems characterization* **35**, 1800096-n/a, doi:10.1002/ppsc.201800096 (2018).
310 Yeh, K. Y. *et al.* Observation of the rose petal effect over single- and dual-scale roughness surfaces. *Nanotechnology* **25**, 345303, doi:10.1088/0957-4484/25/34/345303 (2014).
311 Zou, H. & Zhai, S. Synthetic strategies for raspberry-like polymer composite particles. *Polymer chemistry* **11**, 337-3392, doi:10.1039/d0py00394h (2020).
312 Tang, X. *et al.* Simple, robust and large-scale fabrication of superhydrophobic surfaces based on silica/polymer composites. *RSC Advances* **3**, doi:10.1039/c3ra44502j (2013).
313 Koval, I. V. The chemistry of disulfides. *Russian chemical reviews* **63**, 735-750, doi:10.1070/RC1994v063n09ABEH000115 (1994).
314 Tonkin, S. J. *et al.* Chemically induced repair, adhesion, and recycling of polymers made by inverse vulcanization. *Chem Sci* **11**, 5537-5546, doi:10.1039/d0sc00855a (2020).
315 Freeman, R. G. *et al.* Self-Assembled Metal Colloid Monolayers: An Approach to SERS Substrates. *Science* **267**, 1629-1632, doi:10.1126/science.267.5204.1629 (1995).
316 Kalies, S. *et al.* Surface modification of silica particles with gold nanoparticles as an augmentation of gold nanoparticle mediated laser perforation. *Biomed Opt Express* **5**, 2686-2696, doi:10.1364/BOE.5.002686 (2014).
317 Félix, L. L., Porcel, J. M., Aragón, F. F. H., Pacheco-Salazar, D. G. & Sousa, M. H. Simple synthesis of gold-decorated silica nanoparticles by in situ precipitation method with new plasmonic properties. *SN Applied Sciences* **3**, 443, doi:10.1007/s42452-021-04456-0 (2021).
318 Otoufi, M. K., Shahtahmasebebi, N., Kompany, A. & Goharshadi, E. A systematic growth of Gold nanoseeds on Silica for Silica@Gold core-shell nanoparticles and investigation of optical properties. *International Journal of Nano Dimension* **5**, 525-531, doi:10.7508/ijnd.2014.06.003 (2014).
319 Park, J.-W. & Shumaker-Parry, J. S. Structural Study of Citrate Layers on Gold Nanoparticles: Role of Intermolecular Interactions in Stabilizing Nanoparticles. *Journal of the American Chemical Society* **136**, 1907-1921, doi:10.1021/ja4097384 (2014).
320 Vakarelski, I. U., McNamee, C. E. & Higashitani, K. Deposition of silica nanoparticles on a gold surface via a self-assembled monolayer of (3-mercaptopropyl)trimethoxysilane. *Colloids and surfaces. A, Physicochemical and engineering aspects* **295**, 16-20, doi:10.1016/j.colsurfa.2006.08.021 (2007).
321 Loos, M. in *Carbon Nanotube Reinforced Composites* (ed Marcio Loos) 1-36 (William Andrew Publishing, 2015).
322 Noginov, M. A., Zhu, G. & Gavrilenko, V. I. Sensitized nonlinear emission of gold nanoparticles. *Opt Express* **15**, 15648-15655, doi:10.1364/OE.15.015648 (2007).